MULTIMODAL IMAGING OF TUMOR MICROENVIRONMENT IN MURINE WINDOW CHAMBER MODELS USING OPTICAL, MAGNETIC RESONANCE, AND NUCLEAR IMAGING TECHNIQUES

by

Hui Min Leung

A Dissertation Submitted to the Faculty of the

COLLEGE OF OPTICAL SCIENCES

In Partial Fulfillment of the Requirements
For the Degree of

DOCTOR OF PHILOSOPHY

In the Graduate College

THE UNIVERSITY OF ARIZONA

2015

THE UNIVERSITY OF ARIZONA
GRADUATE COLLEGE

As members of the Dissertation Committee, we certify that we have read the dissertation prepared by Hui Min Leung entitled *Multimodal Imaging of Tumor Microenvironment in Murine Window Chamber Models Using Optical, Magnetic Resonance, and Nuclear Imaging Techniques* and recommend that it be accepted as fulfilling the dissertation requirement for the Degree of Doctor of Philosophy.

_____ Date: 25 November 2015
Arthur F. Gmitro

_____ Date: 25 November 2015
Hong Hua

_____ Date: 25 November 2015
Jean-Philippe Galons

Final approval and acceptance of this dissertation is contingent upon the candidate's submission of the final copies of the dissertation to the Graduate College.

I hereby certify that I have read this dissertation prepared under my direction and recommend that it be accepted as fulfilling the dissertation requirement.

_____ Date: 25 November 2015
Dissertation Director: Arthur F. Gmitro

STATEMENT BY AUTHOR

This dissertation has been submitted in partial fulfillment of requirements for an advanced degree at the University of Arizona and is deposited in the University Library to be made available to borrowers under rules of the Library.

Brief quotations from this dissertation are allowable without special permission, provided that accurate acknowledgment of source is made. Requests for permission for extended quotation from or reproduction of this manuscript in whole or in part may be granted by the head of the major department or the Dean of the Graduate College when in his or her judgment the proposed use of the material is in the interests of scholarship. In all other instances, however, permission must be obtained from the author.

SIGNED: Hui Min Leung

ACKNOWLEDGEMENTS

This dissertation could not have been accomplished without many people and I would like to convey my most sincere gratitude to them here.

To my parents and family: Thanks for giving me your blessings to pursue my dreams away from home, even though that means having to constantly worry for me, much more than usual.

To my advisor Dr. Arthur Gmitro: Thanks for your immense patience, tolerance and kindness throughout all these years. You have built a wonderful working environment where I enjoy learning and making strides towards my goals. It has been a great honor to learn from you, from imaging techniques to water skiing skills, from writing grant proposals to your inimitable interpersonal skills. Your respectibility, trustability and openess have a great influence on me and I'm fortunate to have benefited from that kind of working relationship.

To Dr. Andy Rouse: Thank you for being there for me and everyone in the laboratory with an assuring smile everyday. Thanks for teaching me useful techniques about optics and computers and for answering my questions whenever I walked into your office flustered. And thanks for inviting me to lake trips on your boat that were so much fun.

To my committee members: Thanks Dr J. P. Galons and Dr. Hong Hua for taking time to be on my committee. Dr Galons, there is never a moment when I don't enjoy learning the tricks of the trade of MRI from you and thanks for your words of encouragement. Dr Hua, thanks for the invaluable advice that you have given me to improve the optical system that I was trying to develop.

To Dr Furenlid: Thanks for allowing me to use the ModPET system in your laboratory and spending time to teach me how to process the data. I am also especially grateful for the words of wisdom you have kindly offered me, from coursework to career paths. I thoroughly enjoyed your classes and inspire to be as effective and articulate as you in presentations.

To my labmates: Thanks Xiaoyu for being such a dear friend who kept me going whenever I ran out of strength. Thanks Rachel for developing the MWC model. I reminisce the days when we soldier on together as curveballs just kept coming our way.

I would like to express my heartfelt appreciation for all the help and expertise provided by Center for Gamma-Ray Imaging's 3D printing team.

I would also like to thank Chisty Barber, Christy Howison, Gillian Paine, and Bethany Skovan for their expertise in animal care and surgery.

Lastly, thanks to Ting for putting up with all my nonsense and being with me on good days and bad days.

DEDICATION

To my family and advisor

TABLE OF CONTENTS

TABLE OF CONTENTS – *Continued*

TABLE OF CONTENTS – *Continued*

LIST OF FIGURES

LIST OF FIGURES – *Continued*

LIST OF FIGURES – *Continued*

LIST OF FIGURES – *Continued*

LIST OF FIGURES – *Continued*

LIST OF FIGURES – *Continued*

LIST OF TABLES

ABSTRACT

Pre-clinical study of cancer often involves imaging different aspects of a tumor, ranging from visualizing sub-cellular detail to imaging of the tumor anatomy. Multimodal imaging seeks to combine imaging techniques with complementary strengths and use them to provide a more complete picture of the disease. In this dissertation work, the development of various optical, nuclear and magnetic resonance imaging (MRI) techniques applicable to the study of cancer xenografts in murine window chamber models was carried out. Two types of window chamber models were used in this work: the dorsal skinfold WC (DSFWC) model and the mammary WC (MWC) model. The MWC was specifically used to study breast cancer xenografts.

In this work, optical pH imaging with a pH-sensitive fluorescent agent was used to evaluate methods to achieve tumor-specific pH modulation. Temporary tumor acidification was performed by administration of an agent that consists of glucose and meta-iodobenzylguanidine. On the other hand, re-normalization of pH_e in acidic tumor tissue was achieved by administration of buffer solutions, such as sodium bicarbonate.

A broadband reflectance spectral imaging system was developed to perform *in vivo* imaging of oxygen saturation in the MWC murine model. The imaging system was used to study tissue oxygenation changes in animals that receive chemotherapy. Preliminary results were obtained to evaluate the utility of the MWC murine model in imaging the spatiotemporal changes in oxygen saturation (SaO_2) as an early biomarker of response to neo-adjuvant chemotherapy.

To study metabolic activity, nuclear imaging of radiolabeled fluorodeoxyglucose (18F-FDG) was carried out using a β-imager, as well as a pre-clinical PET system. The 2D nuclear imaging capability of the β-imager was cross-validated with the 3D PET imaging system.

Anatomical and functional MRI was performed on the MWC murine model. Anatomical MRI was used to study tumor growth rates, which aid in the identification of animals that responded to chemotherapy. In addition, diffusion-weighted (DW) MRI, dynamic-contrast-enhancement (DCE) MRI, and perfusion MRI were performed to study various functional aspects of the tumor xenografts.

Lastly, work was done to incorporate patient derived xenograft (PDX) tumors into the MWC murine model. As opposed to xenografts grown from cultured cancer cells, PDX tumors better recapitulate characteristics of human tumors. This new cancer model is aimed at improving the translational power of pre-clinical studies employing window chamber models.

CHAPTER 1

Introduction

1.1 Cancer imaging

Cancer is a heterogeneous condition that dynamically evolves and is remarkably adaptive [1]. A tumor's phenotype is a term that describes its physical and functional traits. The phenotype of a tumor is a consequence of its genetic expression, which in turn, is intricately linked to factors such as tumor microenvironment, stressors, and treatment. Cancer researchers have found that heterogeneity in phenotype exists even within the same tumor and selective pressure brought on by the aforementioned factors can have profound effects on altering the tumor phenotype and, ultimately, affect cancer progression [2, 3].

Cancer research entails work in three phases, namely *in vitro* studies, preclinical research typically in animal models, and clinical testing. Table 1.1 summarizes the key utility of each phase of the research. Although research in each phase has its own limitations and advantages, the ultimate goal has always been to gain knowledge that is useful in the clinic. While *in vitro* cell studies are well controlled and can be carried out with minimal regulatory restrictions, they do not represent clinical disease well. This is because experiments on isolated cells are carried out in artificial settings, which are void of interactions with a natural biological system. Pre-clinical animal studies serve to bridge the gap between *in vitro* cell studies and clinical trials on humans. Nevertheless, with less than half of the preclinical results being replicated in humans [4], there is a need to improve translational power.

Preclinical study of cancer often involves the imaging of many different aspects of a tumor. It can range from visualizing sub-cellular detail to the imaging of the whole animal. It is a tall order to find a single imaging modality that can satisfy all the desired imaging requirements. Multimodal imaging seeks to combine imaging

Table 1.1: Phases of cancer research

Phase	Imaged object	Imaging purposes
In vitro studies	Cultured cells	Cell characterization
Preclinical	Small animals	Study cancer biology, drug efficacies, developing treatment strategies
Clinical	Human patients	Lesion detection, diagnosis, staging, monitoring of disease

techniques with complementary strengths and use them to provide a more complete picture of the disease. Another critical step in improving translational power is finding a more representative animal cancer model. These are the main themes that motivated the research in this dissertation.
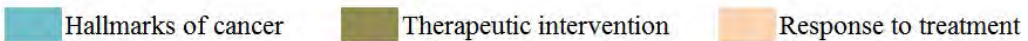
In this work, a number of imaging techniques were developed and used to non-invasively study tumor xenografts in murine window chamber (WC) models. A WC is a stable structure that can be surgically implanted onto a living animal to facilitate repeated imaging of the underlying tissue of interest. Table 1.2 gives an overview of the imaging techniques that were used. The techniques fall under three main imaging categories, namely optical, nuclear, and magnetic resonance imaging (MRI). Specific imaging modalities can be used in combination to facilitate the study of certain aspects of cancer biology. The imaging of the hallmarks of malignant tumors, investigation of pH modulation as a therapeutic intervention, and the imaging of biomarkers associated with response to treatment were main studies used to demonstrate the versatility of the WC model.

1.2 Structure of dissertation

The following sections of Chapter 1 provide a broad overview of window chamber models, the imaging modalities employed, and how these varying techniques can be applied to studying different characteristics of cancer xenografts in window chamber models. The subsequent chapters are dedicated to describing each imaging modality in detail and the experiments performed with that modality. Finally, the latest multimodal imaging work that was done on a newly developed patient derived

Table 1.2: Multimodal imaging of cancer in WC models

Studies	Metrics	Imaging modality	Optical	MRI	Nuclear
	Tumor growth rates	T2-weighted MRI		x	
		Confocal microscopy	x		
	Metabolic activity	Small animal PET			x
		Beta-imaging	x		x
	Perfusion	Arterial spin labelling		x	
	Oxygenation / hypoxia	Spectral imaging	x		
	Angiogenesis / vascularity	Confocal microscopy	x		
	pH	Confocal microscopy	x		
	Receptor expression	Confocal microscopy	x		
	Diffusion	Diffusion-weighted MRI		x	

Hallmarks of cancer   Therapeutic intervention   Response to treatment

xenograft (PDX) model will be described. Readers may find the list of abbreviations in Appendix A a useful reference.

1.3 Brief introduction to multimodal imaging in murine WC models

Anatomical and functional imaging are two complementary classes of methods used in studying cancer biology. Anatomical imaging is used for investigating tumor growth rates, visualizing necrosis, and invasion into surrounding tissue. However, these morphological changes are often preceded by changes in the tumor microenvironment such as dysregulation of expression of cell receptors, abnormal metabolic pathways, angiogenesis, pH levels, vascular permeability, and tissue oxygenation. Imaging of these functional changes are, therefore, referred to as functional imaging. Both functional and anatomical imaging are heavily utilized in many studies, such as the investigation of carcinogenesis, response to treatment, and drug efficacy.

This section provides a brief overview of the imaging methodologies that are utilized in this dissertation work to extract information about the tumor.

1.3.1 Optical imaging

With a transparent coverslip that provides direct visual access to the tumor tissue, WC models are well suited for *in vivo* optical imaging. At superficial tissue layers where scattering effects are not significant, optical imaging has the advantage of providing information at high resolution. For instance, high resolution molecular imaging can be achieved by attaching fluorophores onto an agent that can target specific molecular biomarkers in the tissue. In addition to optical imaging with exogeneous agents, the optical properties of endogeneous tissue components can be utilized to extract useful information about the status of the tissue. The optical imaging techniques utilized in this work involve the use of optical properties of both exogeneous agents and endogeneous components in tissues.

1.3.2 Nuclear imaging

Nuclear imaging is a form of functional imaging that utilizes trace amounts of radiolabeled pharmaceuticals to provide 3D images of the distribution of the tracer. Examples of nuclear imaging include positron emission tomograph (PET) and single-photon emission computed tomography (SPECT). Although the injected radionuclides emit ionizing radiation, there is a negligible health risk associated with the use of nuclear imaging. Nuclear imaging is a common clinical diagnostic tool and PET imaging is often used to detect tumors in human patients. In this work, pre-clinical PET imaging was used to study the metabolic activity of tumors in mice.

1.3.3 Magnetic resonance imaging

For whole body imaging, magnetic resonance imaging (MRI) is a better option than optical imaging. Unlike nuclear imaging, MRI does not utilize ionizing forms of radiation. Instead, magnetic fields and radiofrequency pluses are applied to obtain images. MRI is probably most commonly used to studying anatomy. Nevertheless, its capabilities extend beyond that. There are many MRI techniques that can be used to image physiological parameters such as pH, water diffusion in tissue, blood perfusion, and metabolic activity. Despite the need for sophisticated hardware and reconstruction of raw data, MRI is a commonly available imaging tool in most hospitals and research institutes. MRI was used for both anatomical and functional imaging in this work.

CHAPTER 2

Murine Window Chamber Models

2.1   Introduction to window chambers

Traditionally, tissue has to be excised, fixed, stained with appropriate dyes, and mounted on a glass slide before being imaged with a microscope. In addition to the lengthy time between tissue extraction and imaging, this is an invasive method which only allows limited information of the tissue at one timepoint to be captured. To address these disadvantages, intravital microscopy was developed. As the name suggests, intravital microscopy aims to enable repeated *in vivo* imaging of tissue at high resolution. With the capability to repeatedly observe living tissue with its supporting biological system intact, there is an opportunity to study dynamic phenomena in a more realistic setting than can be accomplished with *in vitro* cell studies.

There are two main methods of performing intravital microscopy. One method requires repeated surgical opening an animal to expose the tissue of interest before each imaging session [5, 6]. The procedure risks infection and inflammation, and is labor-intensive and disruptive to homeostasis. One alternative is to implant a window chamber (WC). Note that a WC is sometimes referred to as a intravital window, imaging window, or simply a chamber in the literature. Once the WC is implanted, imaging can take place at any time with minimal prior preparation.

A WC is a stable structure that can be surgically implanted onto a living animal to facilitate repeated imaging of the underlying tissue of interest. The key component of a WC is a transparent glass coverslip that allows direct optical interrogation of the tissue while serving as a protective barrier between the tissue and the external environment. Because the tissue of interest often lies beneath layers of skin, subcutaneous fat or, in the case of a cranial WC, the skull, these intervening tissues

have to be surgically removed before implantation of the WC. For more detailed information about surgical preparation and procedures involved, the reader is referred to a review article by Makale [7].

One of the earliest implementations of a window chamber appeared in a 1924 article [8] in which vascularization in a rabbit ear was studied. Since then, the technique has been refined and applied to various areas of biomedical research, such as the study of angiogenesis [9], interaction between cancer cells and host cells [10], circulating tumor cells [11], islet cells [12], tissue oxygenation [13], wound healing [14], mestatasis [15], drug delivery [16], brain signals [17], and spinal cord pathalogy [18]. The wide range of studies that involve many different animal models is a testament to the versatility of the WC technique. Figures 2.1(a)-(e) show images of a cranial WC used to study the brain [19], a mammary window chamber (MWC) used to study breast cancer, a dorsal skinfold window chamber (DSFWC) used to study various aspects of tumor biology [19], and a spinal WC that is used to study spinal cord pathalogy [18].

(a) Cranial WC.　　(b) MWC.

(c) DSFWC.　　(d) Spinal cord WC.　　(e) Body WC.
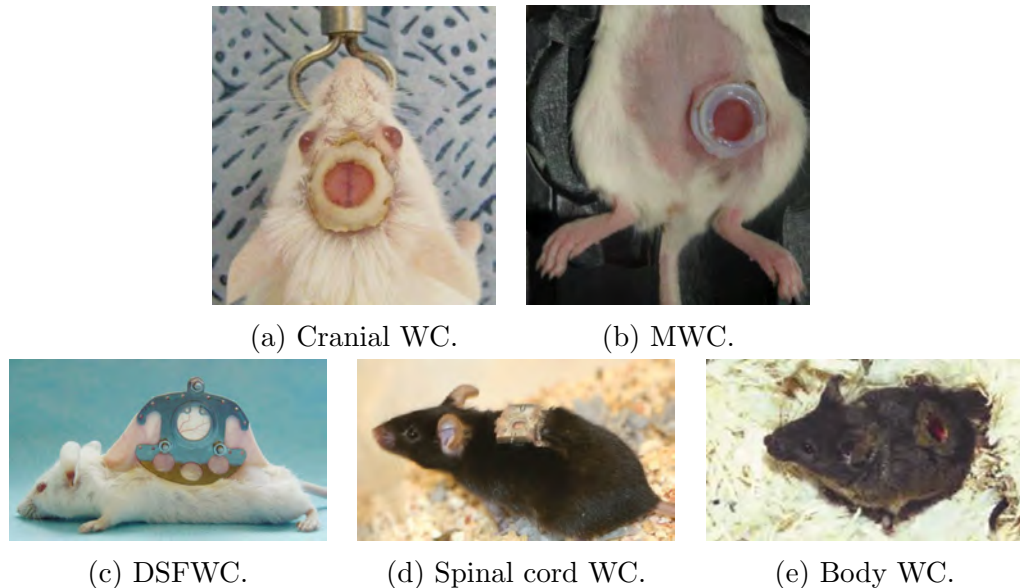
Figure 2.1: Different forms of WC.

In the context of cancer research, there are numerous considerations when trying to implement a murine WC model. They are: 1) the mechanical design of the

WC structure, 2) the location of the implantation of tumor cells and WC, 3) type of tumor cells used, and 4) the genetic strain of the mouse. Judicous selection of these aspects is essential in ensuring that the animal model recapitulates important features of the clinical disease in human patients. Furthermore, the animal model and experiments have to be compliant with the regulations stipulated by the University of Arizona's Office for the Responsible Conduct of Research (ORCR), and the Insitutional Animal Care and Use Committee (IACUC).

The mechanical design of the WC determines the longetivity of the structure and the length of time over which imaging can take place within the animal. The material of the WC has to be bio-compatible as it has to stay in contact with exposed tissue for long periods of time. In addition, the material needs to be lightweight such that the WC will not encumber the animal.

In certain cancer models, malignant tumors occur spontaneously through genetic engineering of the animals. For instance, genes responsible for promoting tumor growth can be overexpressed in genetically engineered mice [20, 21]. To the best of the author's knowledge, research with this spontaneous cancer model has not been integrated with the WC technique. Instead, the use of human tumor xenografts is more common in WC studies. In this cancer model, either cultured cells from established human cancer cell lines or pieces of resected tumors from human patients are transplanted into mice with a suppressed immune system (immunodeficient mice). Depending if the transplatation is done at a dissimilar or similar site from the origin of the tumor cells, one has either an ectopic or orthotopic cancer model, respectively. Immunodeficient mice are used for such studies because these animals have limited ability to trigger an immune response to foreign tissue, which increases the chance of successful engraftment [22]. Commonly encountered immunodeficient mice for cancer studies include severe combined immunodeficient (SCID) mice, nonobese diabetic (NOD) SCID mice, NOD SCID gamma (NSG) mice, and nude mice. Because immune response plays a key role in tumorigenesis, there have been concerns about the use of immunodeficient mice in cancer studies [23]. However, immunodeficient mice models currently remain the best available option.

2.1.1 Ectopic DSFWC murine model

The DSFWC is a versatile ectopic murine model that is most suitable for studying tumor types such as melanoma, and carconoma of the colon, lung, breast, pancreas, and prostate [24]. The design of the DSFWC that is used in this work is shown in Figure 2.2. The DSFWC consists of a pair of titanium (Ti) plates that are used to clamp a thin piece of skin flap that is pulled away from the back of a mouse. To avoid excessive clamping of the tissue, which could lead to obstruction of blood flow, an approximate 1.5mm gap is maintained between the pair of Ti plates by placing spacers at each of the screws positions that hold the two plates together. Ti is chosen as the WC material because it is lightweight and biocompatible. These Ti plates are screwed firmly together and sutured onto the skin flap. A section of the skin is removed and a round glass coverslip is placed over the exposed tissue. The coverslip is held in place with a retaining ring. When fully ensembled, the DSFWC has a 9.5mm diameter clear aperture. Chaffing bewteen the structure and the skin of the animal is minimized by using rounded flanges that spread out at an angle to accomodate the torso of the animal.
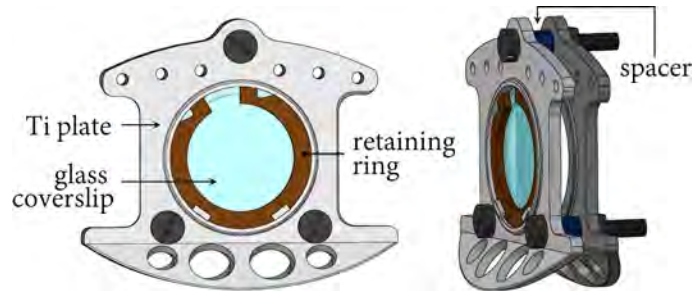
Figure 2.2: Design of the DSFWC. The DSFWC is made up of a pair of Ti plates screwed together. To avoid excessive clamping of the skin fold, they are separated by spacers. At the center of one of the Ti plates, a snap ring holds a glass coverslip in place. The aperture of the other Ti plate is left open.

A set of commercial Ti DSFWC costs about \$400 but it can be reused many times with proper cleaning and maintanence. A photopolymeric version of this DSFWC was 3D printed and used when MRI of the tumor is required. Although they cost much less to fabricate, the photopolymeric versions are comparatively more prone

to damage by animals than the Ti ones. Therefore, they are not re-usable.

The DSFWC model was used to study the effects of tumor acidosis on prostate tumor xenografts (details in Chapter 4). The xenograft was prepared by subcutaneously injecting green fluorescent protein (GFP) transduced tumor cells from a prostatic carcinoma cell line, PC-3, into the tissue under the coverslip. Injection of cells usually took place two days after implantation of the DSFWC. Imaging commenced when the cells began to form a solid tumor, which typically occurred within 3-5 days after cell innoculation.

The Ti DSFWCs are structurely sturdy. Being implanted on animals' backs, they are inaccessible by the animal. As a result, they can stay viable for more than 3 weeks on the animals without any visible damage. Nevertheless, occassional problems such as skin injury due to prolonged stretching or poor hydration of the tumor site due to compromized sealing of the chamber, and retraction of the skin from insufficient clamp force of the WC can lead to premature failure of the WC. Another problem that can be encountered is unsuccessful engraftment of the tumor cells. In such instances, the GFP signals of the tumor cells weakened or disappeared altogether over a period of a few days.

Another advantage of the DSFWC is it can be easily fixed in position on a customized mouse holder to restrict motion artifacts during imaging. The mouse holder depicted in Figure 2.3 was initially designed by Mir Farrokh Shayegan Salek [25] and later refined by various students in Dr. Gmitro's group. It has screw holes that can hold the protruding ends of the screws of the DSFWC and keep the animal stable. The through hole on the holder allows trans-illumination of the tissue in the DSFWC.
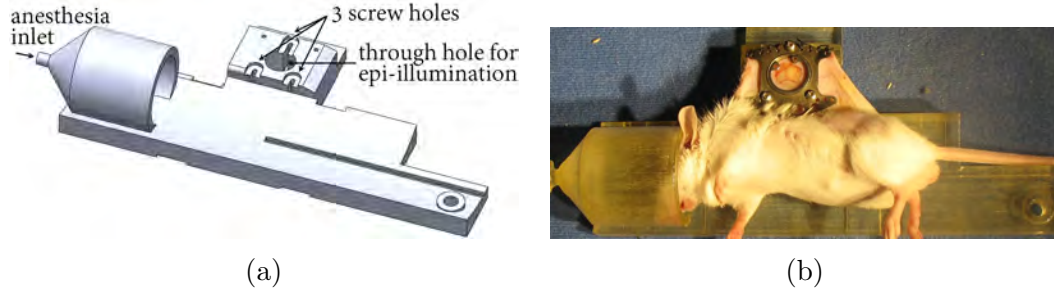
Figure 2.3: Schematic of the DSFWC setup. (a) A DSFWC holder. (b) An anesthetized mouse with a DSFWC sutured to its back.

2.1.2   Orthotopic MWC murine model

The orthotopic MWC that was used in this dissertation work was developed by Rachel Schafer [26] who was a graduate student working with Prof. Gmitro. In contrast to the DSFWC, which is typically an ectopic model, the MWC is an orthotopic murine model specifically developed to study various aspects of breast cancer biology. The orthotopic model has been shown to possess higher predictive power in pre-clinical studies than ectopic tumor models [27]. This is possibly because the tumor cells are transplanted into a similar location where the tumor would arise in human patients and, thus, better mimics the microenvironment in clinical tumors.

Two methods of preparation of breast cancer xenografts have been used in the murine MWC model. The first method utilizes GFP-transduced breast cancer cell lines from American Type Culture Collection (ATCC). The two types of cell lines used in this dissertation work were MDA-MB-231/GFP and MCF-7/GFP breast cancer cells. Approximately 5×10^6 cancer cells were injected into the left 4th mammary fat pad of a female post-breeder SCID mouse, and the MWC was implanted a week later when the tumor reached a size of approximately 100mm^3. In the second method, breast cancer tumor tissue samples obtained from patient biopsies were used instead. Through a collaboration with Dr Ghassan Mouneimne and his collaborators at the University of Utah, a frozen tissue sample of breast tumor tissue, HCI-011 (refer to Table 1 in [28]), was obtained. An initial volume of 8mm^3 of tissue was engrafted orthotopically in the mammary fat pad of an NSG mouse. Tumor vol-

umes were regularly monitored via palpitation. The MWC was surgically implanted soon after the tumor started a rapid exponential growth phase, which typically occurred 4-6 weeks after engraftment. A xenograft prepared by this method is referred to as a PDX tumor.

Figure 2.4 shows a schematic of the MWC design. It is an asymmetrical 13mm diameter rigid structure with a 7.25mm diameter clear aperture after assembly. The asymmetrical design and size are optimized to minimize skin abrasion, maintain animal mobility, and ensure animal tolerance to these implanted structures while providing a reasonable field of view for optical imaging. The main chamber and the retaining rings are 3D printed with a photopolymer (Stratasys, MN, VeroGray RGD850) while the round glass coverslip is an off-the-shelf product (Warner Instruments, Hamden, CT, Model CS-8R).
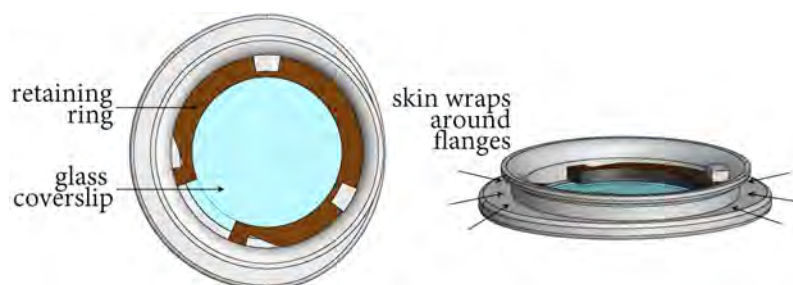
Figure 2.4: Design of the MWC. The MWC is implanted after a circular incision is made on the skin. Due to the elasticity of the skin, it wraps around the bottom flange of the MWC. Surgical glue is then used to hold it in place without the need for sutures. A glass coverslip then covers the wound and is held in place by a retaining ring.

During surgical implantation, a round incision smaller than the size of the MWC is made above the left 4th mammary fat pad of the mouse. The lower flange of the MWC is then fitted under the incision, which allows the skin to wrap around the structure due to the skin's natural elasticity. Next, surgical glue is applied to fix the MWC in place. Finally, the coverslip and retaining ring are used to cover the wound. Because no suturing is required, the surgical procedure can be completed in approximately 15 minutes.

Unlike the DSFWC, the MWC is easily accessible to the animal. Incessant chew-

ing by the animal results in deterioriation of the MWC and ultimately detachment. To maximize the amount of time imaging can be done with the MWC, the chamber was implanted after the injected tumor cells had developed into a solid tumor. This typically took a week to occur. After MWC implantation, bitterants (Yuk-2e gel) were regularly applied around the MWC to discourage chewing. A MWC typically maintains structural integrity for approximately one to two weeks, which sets the limit for the period of time imaging can be carried out.

During imaging experiments, animals were anesthetized with 1.5% isofluorane and a 1 L/min medical-grade oxygen flow rate. It was sometimes necessary to slightly adjust the isoflurane concentration while keeping the oxygen flow rate constant to maintain a stable respiration rate throughout experiments. Mice were placed in a supine position in a custom-made holder and a stabilizing bar was fitted snugly over the MWC to reduce motion artifacts due to respiration (Fig. 2.5(a)). The round opening on the stabilizing bar fits around the MWC and restricts respiratory motion of the tissue under the MWC. Care was taken to prevent excessive pressure on the animal, which could result in difficulty breathing. A photograph of an animal with an implanted MWC is shown in Figure 2.5(b).

(a)   (b)
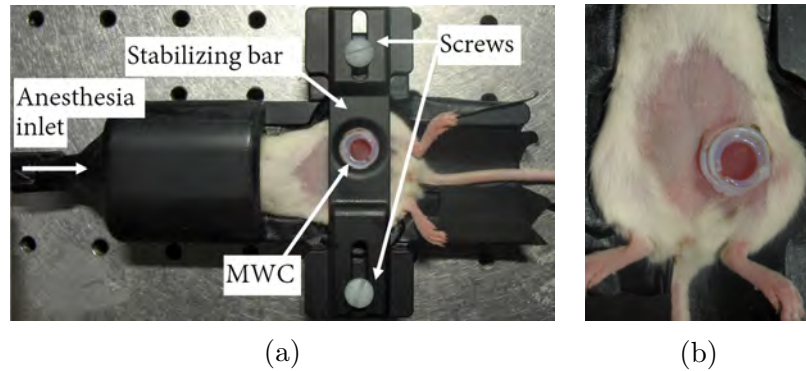
Figure 2.5: Schematic of the MWC setup. (a) An anesthetized mouse secured in a customized holder with a stabilizing bar used to minimize respiratory motion artifacts.(b) An mouse with an implanted MWC.

CHAPTER 3

Optical Setup and Calibration for pH Imaging

3.1   Abnormal metabolism of cancer cells

There are two main pathways by which glucose is metabolized in the body. In the first pathway, which is known as glycolysis, glucose is metabolized into pyruvate and subsequently reduced to lactate. In the second pathway, glucose undergoes the same initial metabolic process in which it is broken down into pyruvate. The pyruvate then enters the tricarboxylic acid cycle (also commonly referred to as Krebs cycle or citric acid cycle) before finally undergoing oxidative phosphorylation. Like the name suggests, oxidative phosphorylation requires the consumption of oxygen.

In both metabolic pathways, adenosine triphosphate (ATP) is produced. Because ATP is a necessary component used for energy transport in living tissues, the number of ATP molecules produced per glucose molecule is a measure of the energy efficiency of each metabolic pathway. Glycolysis of a glucose molecule to lactate yields an estimated 2-8 ATP molecules while complete metabolism of each glucose molecule through the oxidative phosphorylation process yields 29-38 ATP molecules [29–32]. Clearly, oxidative metabolism is much more efficient than glycolytic metabolism of glucose.

Normal cells at rest state preferentially undergo oxidative phosphorylation, which is estimated to account for 90% of the ATP production [33]. When there is inadequate supply of oxygen to support oxidative phosphorylation, cells are able to re-direct pyruvate away from that oxidative process and reduce it to lactate instead. Glycolysis under the condition of insufficient oxygen is referred to as anaerobic glycolysis.

When tumorigenesis, or the transformation of normal cells to cancer, takes place, it often involves metabolic reprogramming. Compared to healthy cells, cancer cells

exhibit a much higher perference (approximately 10 times as much) for glycolytic metabolism, even in the presence of sufficient oxygen supply [33]. This seemingly paradoxical phenomenon is known as aerobic glycolysis, or the "Warburg effect". It is named after Otto Warburg who first reported abnormal cells' preference for the less energy efficient metabolic pathway in the 1920s [34][†]. Various groups have hypothesized that glycolysis reflects a tumor's greater reliance on anabolism for more rapid proliferation and that various forms of catabolism could serve as alternative sources of energy [35, 36].

This dissertation involves work that studies two closely related downstream effects of this reprogramming of metabolic pathways. They are namely, the dysregulation of pH levels, and the occurrence of hypoxia in tumors. Dysregulation of pH levels, which leads to tumor acidosis is discussed in this chapter. Hypoxia and changes in tissue oxygenation are later described in Chapter 7.

3.2   Altered metabolism and tumor acidosis

Malignant tumors are highly proliferative and, thus, metabolically active. Due to metabolic reprogramming, which makes them preferrentially undergo glycolytic metabolism, large amounts of lactate are produced during the glycolytic process. When the amount of lactate produced exceeds the threshold buffering capacity of HCO_3^-, extracellular pH (pH_e) decreases, leading to tumor acidosis. In healthy mammalian cells, intracellular pH (pH_i) and pH_e are approximately 7.2 and 7.4, respectively. Under normal conditions, pH_i and pH_e are highly regulated. However, when tumor acidosis sets in, there is a reversed pH gradient, whereby pH_i and pH_e are $\geqslant 7.4$ and $\leqslant 7.1$, respectively [37–40].

There are several adverse effects associated with dysregulation of pH levels. For instance, it has been linked to increased protection against apoptosis, thereby leading to unchecked proliferation [41, 42]. It has also been demonstrated to mediate degradation of the extracellular matrix, increase the production of fibroblasts, which

---

[†]Many of Warburg's publications are in German language or translated into English by others.

then enhance cell motility, and ultimately, enhance metastatic potential [43, 44]. These are viewed as adaptive mechanisms that many types of cancer cells are observed to acquire [45].

In light of the evidence for acid-mediated tumor invasion, re-normalizing tissue pH or driving tumor acidosis past tolerable thresholds are being explored as possible therapeutic interventions [40, 46–48]. The former type of therapy is termed buffer therapy and it serves to re-normalize pH_e of tissue that has compromised mechanisms for maintaining homeastasis but does not alter the pH of blood. No acute side effects are anticipated and this buffering therapy approach is considered safe. Although laboratory experiments have shown mixed therapeutic results [49, 50], there has been a push toward translating this method into clincal application. Researchers at Moffitt Cancer Center, for instance, have been carrying out clinical trials of buffer therapy on pancreatic cancer patients by having patients chronically consume 300-900 mg of dissolved sodium bicarbonate per day per kg of patient's body weight [51]. This work motivated the pH modulation experiements carried out in this work. The following sections of this chapter describe the optical pH measurement methodology and the optical pH calibration procedures. The use of *in vivo* optical pH imaging methods to explore and evaluate various pH_e modulating methods are discussed in the following chapter.

3.3   Optical measurement of pH_e *in vivo*

The use of micro-electrodes inserted into tissue through the lumen of hypodermic needles is a common method of measuring pH in live animals. Typically sold in 25 gauge needles that have an outer diameter of about 0.5mm, repeated insertion of these electrodes often result in tissue injury. This limits the number of readings that can be done on an animal at any one time, and can lead to sampling error.

Various non-invasive pH measurement methods have been developed by different research groups to overcome this issue. MRI with acidoCEST [52] or magnetic resonance spectroscopy (MRS) after the injection of hyperpolarized 13C-labelled

bicarbonate [39] are two prominent MR techniques capable of measuring pH_e. Although MR methods have the advantage of being easily translatable to the clinic, many challenges remain. AcidoCEST is sensitive to non-uniformities in magnetic field in the machine and might not have sufficient sensitivity to be applicable in small animal models. MRS requires specialized equipment to produce nuclear spin polarization and has a very short time window over which the polarization can be maintained at ambient or body temperature.

Alternatively, optical methods can be used to measure pH. Such methods typically make use of fluorescent agents that have pH-dependent emission spectra such as BCECF [53], dyes in the mFruit series [54], and benzoxanthenes dyes [55]. 5-(and-6)-carboxy-SNARF-1 (hereinafter referred to as SNARF-1) is an isomer in the family of benzoxanthene dyes. As illustrated in Figure 3.1, the equilibrium between anionic (protonated) and neutral (deprotonated) forms shifts in response to the concentration of H^+ ions, thereby giving SNARF-1 its pH-dependent fluorescent emission properties. Its pH-dependent absorbance and fluorescent emission spectra are shown in Figure 3.2. With a 488nm excitation (Figure 3.2(a)), the SNARF-1 fluorescent emission peak shifts from about 580nm to 640nm as pH increases from 6 to 9 with an isosbestic point at approximately 620nm. Figure 3.2(b) shows that a similar spectral behavior can be observed with the use of a different excitation wavelength. Depending on the excitation wavelength of choice, the ratio of the emission signals from two different sides of the isosbestic point yields a metric that is monotonic with pH change and can be calibrated to quantify pH. This ratiometic measurement technique has the advantge of being insensitive to absolute concentration of the dye in the sample. SNARF-1 has an acid dissociation constant, $pK_a = 7.5$ at ambient temperature [55], making it appropriate for measuring pH_e in tumors [40, 49].
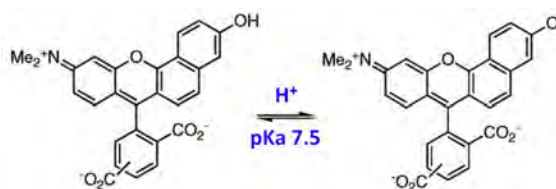
Figure 3.1: Protonated (left) and deprotonated forms of C-SNARF-1.
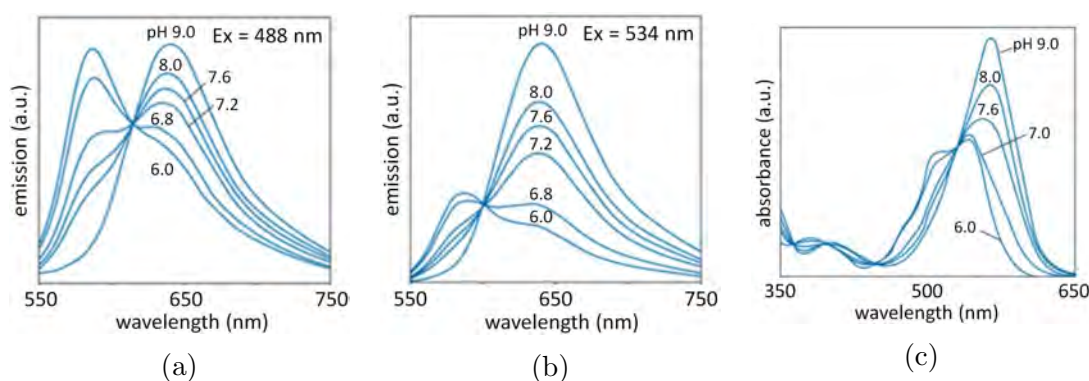
Figure 3.2: Emission spectra of SNARF-1 with (a) 488nm and (b) 534nm excitation. (c) Absorbance spectrum of SNARF-1. Images adapted from [56]

.

3.4 pH measurement and calibration

As mentioned previously, the ratio of the emission signals from two different sides of the isosbestic point of SNARF can be calibrated to quantify pH. The fundamentals of the ratiometric pH imaging methodology and various error sources associated with it can be found in the dissertation work of Yuxiang Lin [57, 58], who was a former graduate student working with Prof. Gmitro. My dissertation work expands upon Lin's work. Improvements to the pH calibration and image processing methods were made, and temperature-dependent effects were taken into account during image processing. This section outlines the experimental work taken to perform pH calibration. The optical setup, which was used for pH calibration and measurements, is also described in this section. In addition, the use of the ratiometric pH imaging approach was applied to study various methods to achieve pH modulation in animals. They will be discussed in Chapter 4

3.4.1 Phantom preparation for pH calibration

SNARF-1 (#C-1270, Life Technologies) was used as a cell impermeable fluorescent pH_e sensor for all WC experiments done in this dissertation work. Delivered in powder form, a SNARF solution was prepared by dissolving the powder in sterile biotechnology grade phosphate buffered saline (PBS). By adding small amounts of either HCl or NaOH, the pH of the SNARF solution was adjusted to make phantoms of different acidity.

In order to make measurements with a pH electrode (InLab Science Pro electrode, Mettler Toledo, OH, USA), its voltage readings had to be calibrated with buffer solutions of known pH values = 4.00, 7.01, and 10.01 (Orion pH Buffer Bottles, Thermo Scientific, USA). Next, a small amount of the SNARF-1 solution that was prepared earlier was added to a beaker of 20% intralipid solution. Intralipid is a fat emulsion that is often used to mimic scatter effects in tissue [59]. The pH of the resulting solution was then measured by the calibrated pH electrode. Either diluted NaOH or HCl was incrementally added to the SNARF-intralipid solution to produce SNARF solutions with pH values ranging from approximately 6.4-7.4. At each desired pH, a small amount of SNARF solution was transferred into a borosilicate micro glass cell (BMC-080-14-50,Friedrich & Dimmock Inc., USA) and sealed at both ends. The material and wall thickness of the glass cell are similar to those of the glass coverslips used in the WC. Because the response of the pH electrode and the dissociation reaction of SNARF are temperature dependent, all measured solutions were warmed to approximately 37 ^oC to ensure accuracy of the calibration procedure.

3.4.2 Optical setup

After preparing SNARF phantoms over a range of pH values, optical measurements were done on a Nikon Eclipse E600 microscope with a C1 confocal module. Images were acquired with EZ-C1 v3.90 software. The temperature of the phantoms was maintained at 37^oC during optical measurements by regulating hot air into a

ventilated chamber via a feedback sensor (Figure 3.3). Phantoms were allowed to equilibrate to the chamber's temperature before measurements were taken.
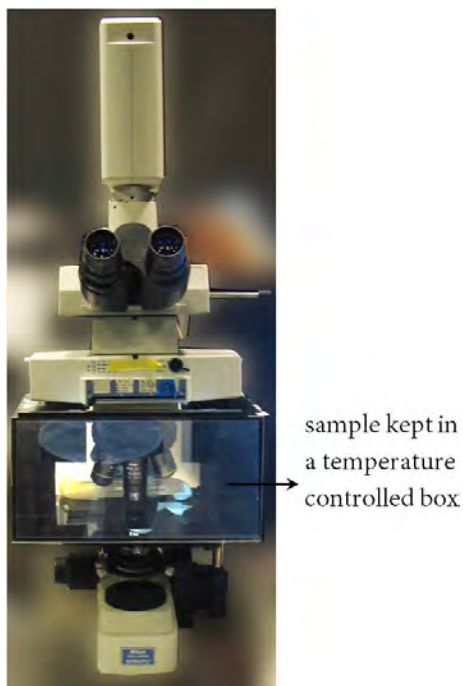
Figure 3.3: A photograph of the temperature controlled box mounted on a confocal microscope to stabilize temperature during pH measurements.

A labelled photograph of the confocal microscope system with a diagram of the attached spectral detection system is shown in Figure 3.4. A 543nm laser source was used to excite SNARF through the laser point-scanning confocal microscope. The resulting fluorescent emission was collected in two spectral channels with PMT detectors. The two emission channels (channels 2 and 3 on microscope) were filtered by a 595/50nm bandpass (BP) filter and 640nm longpass (LP) filter, respectively. PMT gain settings on channels 2 and 3 were set at a constant value (110, 90). Typically, image acquisition was averaged over five times to improve the SNR of the measurement. The ratio of the signals in channels 2 and 3 varies monotonically with the pH of SNARF. Details regarding the ratiometric calibration of the PMT signals to enable quantification of pH are given in Section 3.4.3.

pH calibration on phantoms was performed with 1X and 2X objectives. Most

animal experiments used a 2X objective but a 1X objective was occasionally used. The pinhole of the confocal microscope was fully opened to 150 μm to minimize the effect of chromatic aberration on pH measurements [60]. Opening the pinhole results in reduced optical sectioning and thus, integrated signals from a thicker section of the sample were detected by the microscope. However, this is not a cause for concern in this application because the phantoms were uniform solutions. In the case for animal experiments, the xenografts are typically less than 100mm^3 and depth-resolved information is not required.
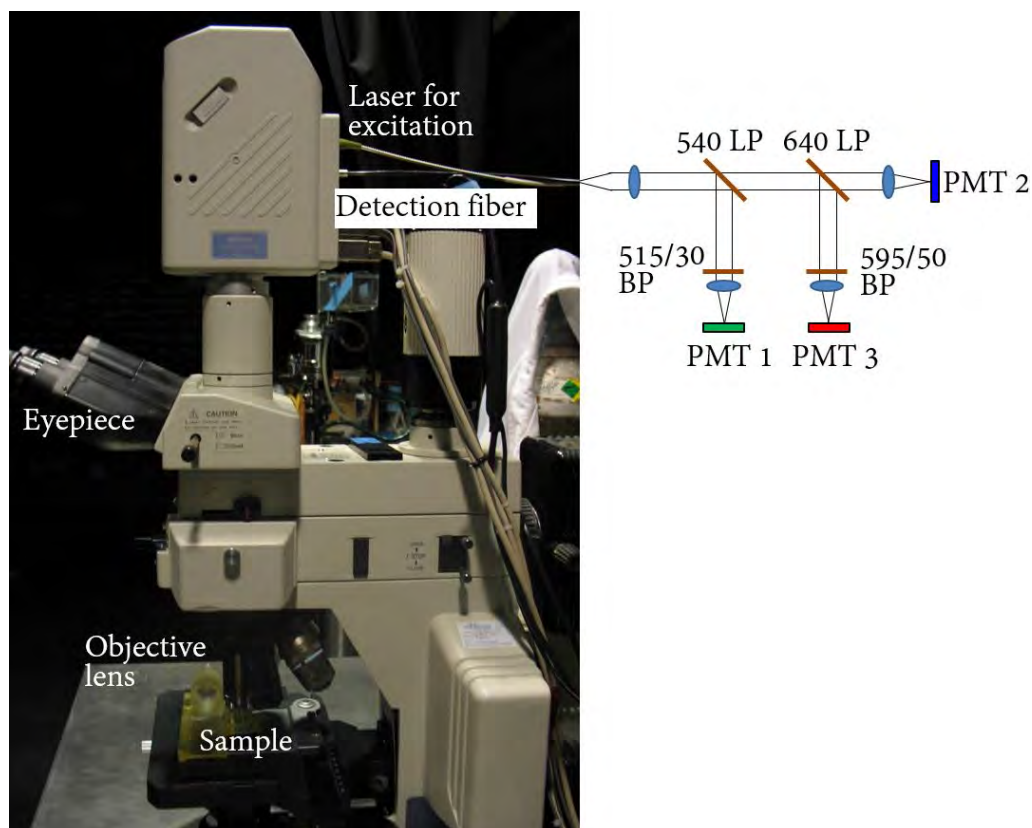
Figure 3.4: A diagram showing the microscope and optical layout used during optical pH imaging.

Table 3.1: Imaging parameters on the microscope

	Magnification	1X
CFI Plan UW 1X	Numerical aperture (NA)	0.04
	Field of view (FOV)	12.5x12.5mm
	Magnification	2X
CFI Plan UW 2X	NA	0.06
	FOV	6.4x6.4mm
	Confocal pinhole size	150μm
Acquisition settings	Dwell time	Variable.
	Gain settings (channel 2, channel 3)	(110,90)
	Excitation	543nm
Fluorescence	Emission detection at channel 2	595/50nm BP filtered
	Emission detection at channel 3	640nm HP filtered

3.4.3 pH calibration procedures and results

The SNARF-intralipid phantoms were imaged in the temperature-controlled chamber using the microscope settings summarized in Table 3.1. Depending on the amount of SNARF present and the pH value of the phantom, the laser scan speed had to be adjusted to ensure both spectral channels had sufficient signal levels and were not saturated. Scan speed was adjusted by changing the dwell time of the scan. It should be noted that the microscope was focused on the object plane that gives the maximum signal strength, which is slightly below the liquid-glass interface of the phantom. Focusing right at the liquid-glass interface should be avoided as explained by Lin et. al. [60].

The fluorescent images contain background signal that needs to be subtracted. The DC signal that constitutes backgound in the two channels are quantified by measuring the emission spectra of a phantom that contains no SNARF. The linear relationship between background signal level and dwell time is shown in Figure 3.5. Because there was no significant difference between measurements made with the 1X objective and 2X objective, the fitting of data was done using the 2X measurements.
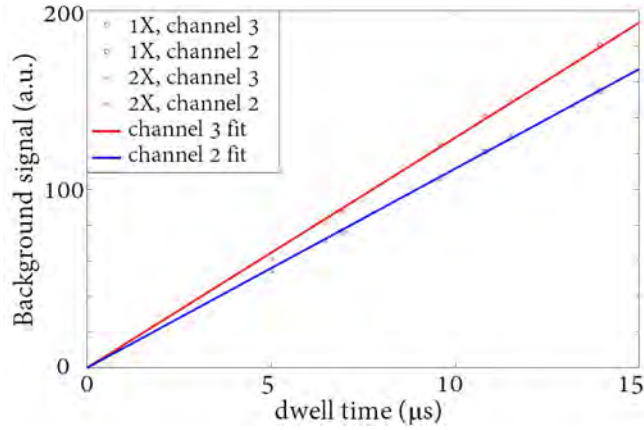
Figure 3.5: Graph of background signal against dwell time measured using 1X and 2X objectives.

The background signals in channel 2 and 3 scale with imaging dwell times and are expressed as Equations 3.1 and 3.2:

$$I_{bg2} = C_{ch2} \ t, \tag{3.1}$$

$$I_{bg3} = C_{ch3} \ t, \tag{3.2}$$

where I_{bg2} and I_{bg3} represents the background signal levels in spectral channels 2 and 3, respectively, and t represents the dwell time used in the measurements. C_{ch2} and C_{ch3} are proportionality constants, determined to be 11.14 and 12.87, respectively for the intralipid phantoms. Equations 3.1 and 3.2 are used to calculate the background signals that need to be subtracted from the fluorescent images of SNARF phantoms, depending on the dwell time that was used to acquire them.

The ratio, R, is defined as:

$$R = \frac{I_2 - I_{bg2}}{I_3 - I_{bg3}}, \tag{3.3}$$

where I_2 and I_3 are the signal levels of the SNARF phantom in spectral channels 2 and 3, respectively. The images from spectral channels 2 and 3 were processed on a pixel-by-pixel basis to derive the value R at each spatial location. The value R

41

represents the ratio of background-subtracted intensity values in the two spectral channels, which varies monotonically with pH.

Five SNARF phantoms with pH ranging from 6.4-7.4 were imaged on the microscope. The images were processed to obtain the R values associated with the pH value. Figure 3.6(a) shows an example of a map of R values across a single phantom that had a known pH value of 7.17. A histogram showing the distribution of R values for that phantom is shown in Figure 3.6(b). The measured standard deviations, σ, of the R values of the phantoms were calculated and the resulting experimental results of R vs. pH is shown in 3.6(c).

(a)   (b)   (c)
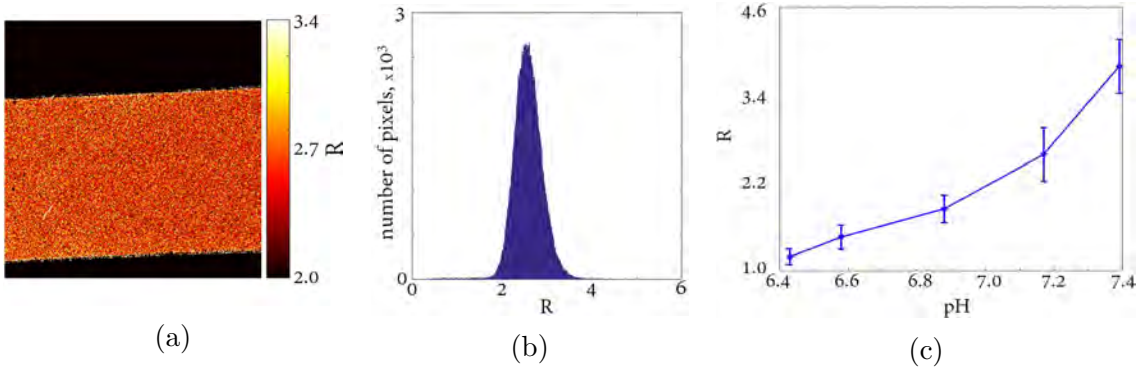
Figure 3.6: Results of pH calibration with SNARF-intralipid phantoms. (a) An example of an image of R values of a phantom with pH=7.17. (b) A histogram of R values in the phantom. (c) A graph of measured R values against known pH values of five different phantoms. Error bars have lengths of 2σ.

The pH and mean R values were used to derive a pH calibration curve given by Equation 3.4. The values were fitted to a model that assumes that SNARF-1 exists only in either protonated or deprotonated forms. The equation of the model is given by:

$$\text{pH} = C_a + log_{10}\left(\frac{R - C_b}{C_c - R}\right) + C_T(T), \tag{3.4}$$

where C_a, C_b, and C_c are constants obtained from curve fitting. T represents temperature and the term C_T is a temperature-dependent offset constant given by:

$$C_T(T) = 1.98 \times 10^{-2}(37 - \text{T}). \tag{3.5}$$

The derivation of Equation 3.4 follows closely to that for a fluorescent Ca^{2+} indicator [61] but was modified to be applicable to SNARF-1 [62]. Although it is possible that photobleaching and photoconversion of SNARF-1 to other fluorescent products could have taken place [63], Equation 3.4 is valid when precautions are taken to prevent excessive exposure of the dye to light. C_a is a function of the pK_a of SNARF-1 while constants C_b and C_c represent extreme R values achievable when SNARF-1 is in a very low and very high pH, respectively. The term C_T is a function of temperature as shown in Equation 3.5, and is used to account for temperature-dependent effects on the calibration curve. It was found that measurement at higher temperatures resulted in overestimation of pH of PBS-buffered SNARF-1 phantoms [58]. The result is reproduced here as Figure 3.7. The temperature dependence was estimated from the data in Figure 3.7 and is given in Equation 3.5. Since the temperature of the chamber was well maintained at 37 ^{o}C during phantom imaging, $C_T = 0$. However, it is difficult to maintain the body temperature of animals during *in vivo* imaging to within $\pm 0.5^o$C . In those instances, $C_T \neq 0$ and corrections are applied based on the actual body temperature of the animal measured with a rectal probe.
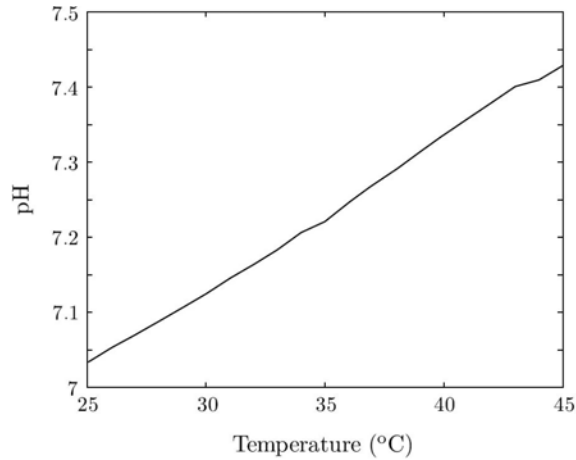
Figure 3.7: Temperature effects of measured pH of a PBS-buffered phantom. Figure reproduced from [58].

Non-linear curve fitting of the data to Equation 3.4 was done using Matlab's trust region minimization algorithmn with robust bisquare weighting. The resulting pH calibration curve for the 2X objective is given by Equation 3.6 and plotted in Figure 3.8(a). A similar procedure was done with the 1X objective and the calibration curve is given by Equation 3.7 and plotted in Figure 3.8(b).

$$\text{pH} = 7.912 + log_{10}\left(\frac{R - 0.8266}{12.60 - R}\right) + C_T(T) \tag{3.6}$$

$$\text{pH} = 7.494 + log_{10}\left(\frac{R - 0.8769}{8.017 - R}\right) + C_T(T) \tag{3.7}$$
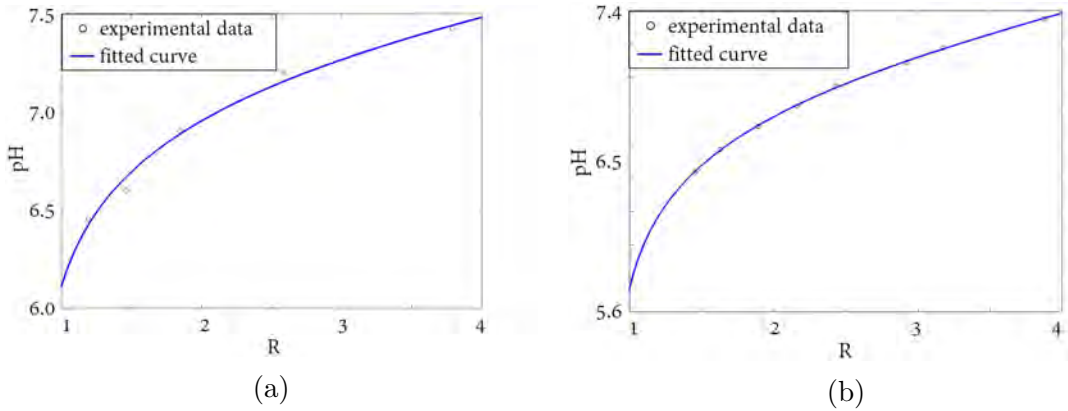
Figure 3.8: pH calibration curves at T = 37 ^oC for the (a) 2X and (b) 1X objective.

CHAPTER 4

Experiments with *In Vivo* pH Imaging in the WC

4.1 Tumor acidification with MIBG and glucose

The chronic lower pH_e of tumor tissue as compared to normal tissue is a direct conse-
quence of the metabolic reprogramming of the tumor cells from oxidative mitochon-
drial respiration to heavy reliance on glycolysis. Despite the many adverse effects
of long term acidification of tumors as outlined in Chapter 3, there are instances
when short term amplification of the Warburg effect facilitates the delivery of certain
types of drugs into cancer cells. One of the ways of achieving that is through the
administration of glucose either with or without meta-iodobenzylguanidine (MIBG).
There are studies that report a positive correlation between the availability of en-
ergy sources and tumor metabolism [47]. Therefore, the induction of hyperglycemia
likely stimulates the rate of glycolysis and, hence, lactate production. The addition
of MIBG further impairs oxidative respiration and forces cells to increase reliance
on glycolysis and reduce oxygen consumption. Because cancer cells tend to have a
predisposition for glycolysis, the pH_e in tumors is more susceptible to acidification
through the administration of glucose and MIBG, then is normal tissue. pH_i, on
the other hand, is more tightly regulated. This results in an increased acid-outside
pH gradient across cell membranes and facilitates the transportation of weak-acid
drugs into tumor cells to achieve enhanced therapeutic effect [64].

4.1.1 Experiment with a higher dose of MIBG and glucose

Experiments with tumor acidification were carried out in the MWC murine model
and with MDA-MB-231 breast cancer xenografts. First, an animal was given an
intravenous (IV) injection of 200μl of 2mM SNARF-1 and imaged for 15-20 minutes
under the microscope using the settings given in Table 3.1. Subsequently, it was

given an intraperitoneal (IP) injection of $200\mu l$ MIBG+glucose and pH imaging was done every 5 minutes for the next 90 minutes. The MIBG+glucose agent was composed of 13.6mM MIBG (#I9890, Sigma Aldrich, USA) and 1.10M 2-Deoxy-D-glucose (#25972, EMD Millipore, USA) (Table 4.1).

Table 4.1: Composition of MIBG+glucose injection

Chemical name	Chemical formula	Molar mass	Concentra-tion	Mass Injected
MIBG hemisulfate salt	$C_8H_{10}IN_3 \cdot 1/2H_2SO_4$	324.13	13.6 mM	0.88 mg
2-Deoxy-D-glucose	$C_6H_{12}O_5$	164.2	1.10 M	36 mg

Figure 4.1(a) shows a GFP image of a heterogeneous tumor, which consists of a core with strong GFP signals and neighbouring regions with significantly weaker GFP signals. The pH map obtained shortly before MIBG+glucose injection (Figure 4.1(b)) shows that most of the pH values of the MWC fall within a range of 6.9-7.3. The pH map obtained approximately 92 minutes after injection is shown in Figure 4.1(c). It is evident that, generally, both the tumor and surrounding tissue became more acidic. However, the effect was much more pronounced in the tumor, resulting in a higher pH_e gradient between tumor cells and surrounding extracellular space. Figure 4.1(d) shows a histogram of the pH_e values in the MWC at these two time points. At 92 minutes after MIBG+glucose injection, the pH_e values were lower and more distributed as compared to the initial time point. This is because the effect of the agent differs in different regions of the tissue.

Figure 4.2 shows the gradual change in pH_e over time, starting from prior to MIBG injection to approximately 92 minutes after injection. To illustrate the phenomena more clearly, the mean pH_e values at two 11x11 pixel ROIs within the MWC were plotted in Figure 4.3. As illustrated in the inset of that figure, ROI 1 is in the normal tissue region where there was no GFP signal while ROI 2 is within the tumor where there was a strong GFP signal. Before the injection of MIBG, the normal tissue ROI had an initial pH_e of approximately 7.2 while the tumor ROI had a lower pH_e of approximately 7.1. After the MIBG injection, the pH_e across the

MWC decreased steadily but the rate of acidification was higher in the tumor ROI. By assuming a linear relationship, the rate of pH drop was 5.2×10^{-3} and 10.3×10^{-3} pH units per minute for ROI 1 and 2, respectively. As a result, 92 minutes after MIBG injection, the difference in mean pH_e between the normal and tumor tissue ROI increased from 0.14 to 0.69. A map of the rate of change of pH_e is shown in Figure 4.4, where the outline of the tumor, shown as a red dotted line, is superimposed on the map. It can be seen that the tumor region had a relatively higher pH_e rate of decrease as compared to the rest of the MWC. This implies that MIBG+glucose affects the pH_e of tumor more than that of the surrounding tissue.
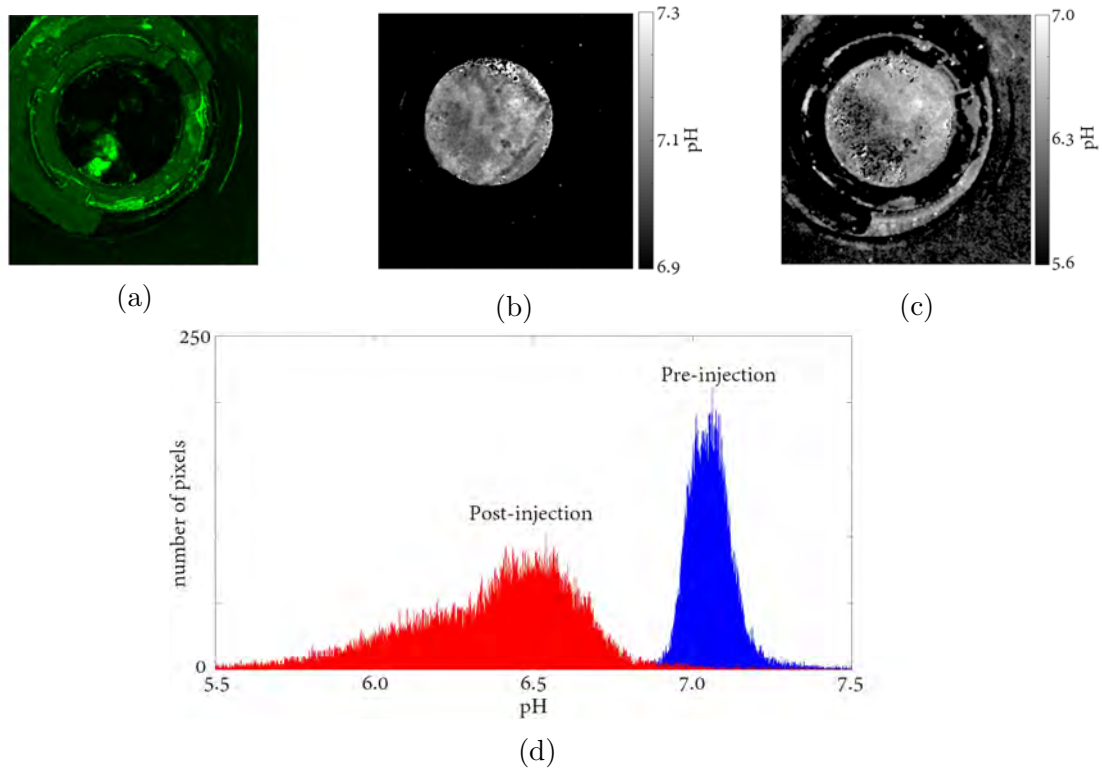
Figure 4.1: pH_e modulation with MIBG and glucose. (a) GFP image of tumor. (b) pH map just before MIBG injection. (c) pH map 92 minutes after MIBG+glucose injection. (d) Histogram of MWC pH values before and 92 minutes after MIBG+glucose injection.
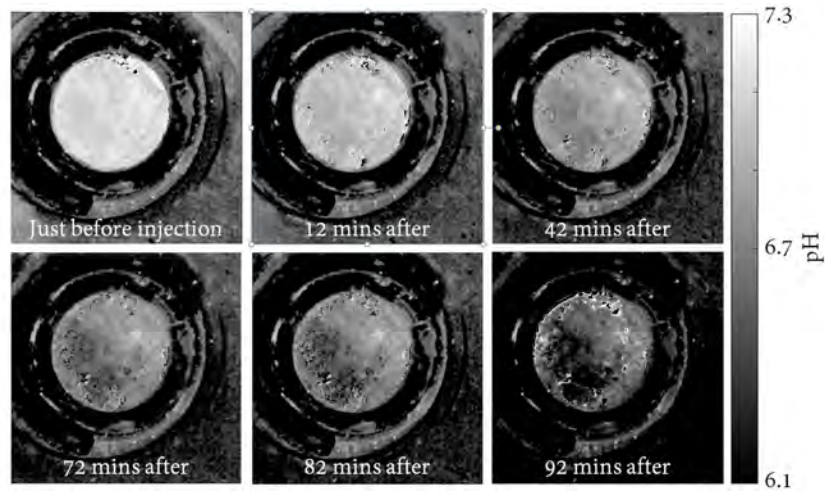
Figure 4.2: pH_e maps obtained at different time points before and after MIBG+glucose injection.
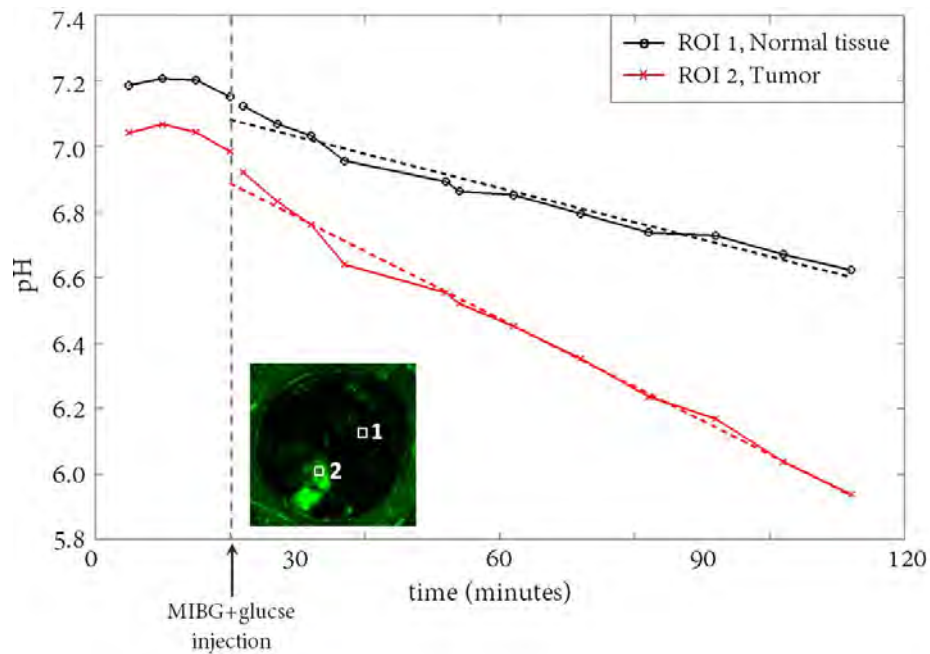
Figure 4.3: pH_e of two ROIs at various time points before and after MIBG+glucose injection. The rate of pH_e drop in ROI 1 was smaller than that in ROI 2. By the end of the experiment, the difference in pH_e between the two ROIs was approximately 0.69. This was much higher than the pH_e difference of 0.14 before the injection of MIBG+glucose.
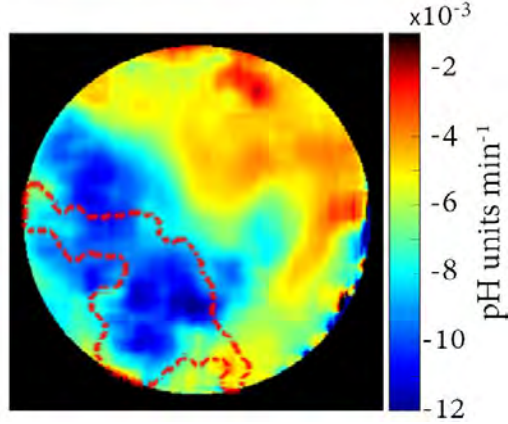
Figure 4.4: A map of rate of decrease of pH_e after MIBG+glucose injection. Dotted line represents the boundary of GFP signals in the MWC. The region with the highest rate of decrease in pH_e corresponds to the tumor region.

4.1.2 Experiment with a lower dose of MIBG and glucose

In an attempt to reduce the acidification of surround tissue, the dose of MIBG+glucose was reduced to what is stated in Table 4.2. The experiment was carried out using the same breast cancer cell line and MWC model. The animal was first given an IV injection of 200ul of 2mM SNARF-1 and imaged for 15 minutes on the microscope. The animal was then given an IP injection of $200\mu l$ of a low dose MIBG+glucose solution and imaged for the next hour at 5-minute intervals.

Table 4.2: Composition of MIBG+glucose injection

Chemical name	Concentration	Mass Injected
MIBG hemisulfate salt	11.1 mM	0.79 mg
2-Deoxy-D-glucose	0.794 M	28.7 mg

A GFP image of the tumor in the MWC is shown in Figure 4.5(a). The pH_e map of the MWC just before and 55 minutes after MIBG+glucose injection are shown in Figures 4.5(b) and (c), respectively. The mean pH_e in a tumor and normal surrounding tissue ROIs were calculated at different time points after injection and the results are shown in Figure 4.6. Inset shows where ROI 1 and 2 are located in the MWC. By assuming a linear relationship, the rates of pH drop were approximately 7.2×10^{-3} and 10.7×10^{-3} pH units per minute for ROI 1 and 2, respectively.

Comparing these results with those in Section 4.1.1, the rate of pH change was similar in the tumor ROI. However, in the normal tissue ROI, a faster pH change was observed. This was unexpected since lower amounts of MIBG and glucose were used.

A map of the rate of acidification with the outline of the tumor superimposed on it is shown in Figure 4.7. Although the region where the fastest rate of acificiation (11-12$\times 10^{-3}$ pH units per minutes) occured is in the tumor, there was moderate acidification (8-10$\times 10^{-3}$ pH units per minute) of the tissue immediately surrounding the tumor. It is possible that the surrounding tissue in the immediate vincinity of the tumor has undergone altered metabolism and, therefore, was being impacted by the MIBG+glucose injection more than normal tissue would be. The tissue regions further away from the tumor had a lower acidification rate of approximately 6-7$\times 10^{-3}$ pH units per minute.

(a) (b) (c)
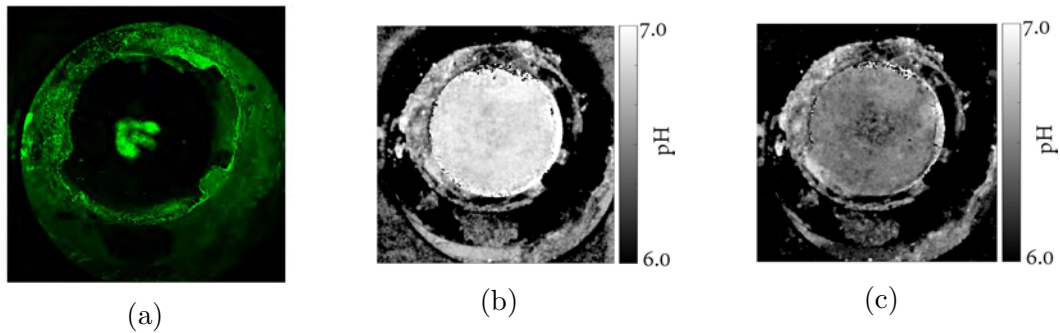
Figure 4.5: pH_e modulation with low dose MIBG and glucose. (a) GFP image of tumor. (b) pH map just before MIBG injection. (c) pH map 55 minutes after MIBG injection.
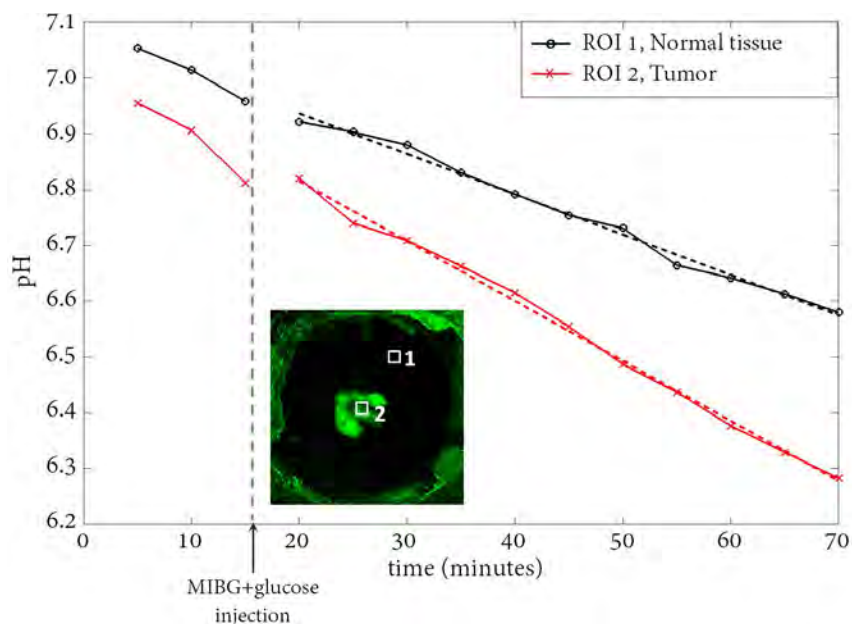
Figure 4.6: pH$_e$ at two ROIs in the MWC before and after MIBG injection. The magnitude and rate of pH drop in normal surrounding tissue, ROI 1, is smaller than that in the tumor.
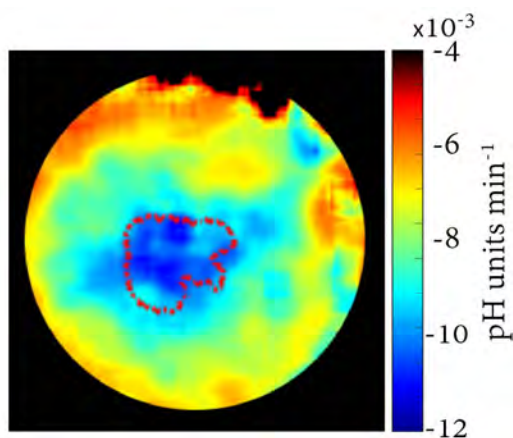
Figure 4.7: A map of rate of decrease of pH$_e$ after MIBG+glucose injection. Dotted line represents the boundary of GFP signals in the MWC. The region with the highest rate of decrease in pH$_e$ corresponds to the tumor tissue.

This experiment showed that the modified lower dose of MIBG+glucose did not change the rate of decrease of pH$_e$ in the tumor. This implies that the given dose of MIBG+glucose was in excess of the maximum rate of glycolytic metabolism that can

be stimulated. Therefore, the rate of lactate production and, hence, acidification of the tumor was at the limit.

On the other hand, the rate of pH_e drop in the normal surrounding tissue was higher when a lower dose agent was used. This observation was unexpected. However, the ratio of the concentrations of MIBG to glucose was slightly different between the two experiments. It was 1:81 in the higher dose agent and 1:72 in the lower dose agent. MIBG is a mitochondrial inhibitor and would presummably affect all tissue indiscriminately. On the other hand, glucose would preferrentially stimulate metabolic activity in a tumor where metabolic reprogramming to a high glycolytic metabolism occured. It is unclear if the difference in the MIBG to glucose ratio affected the rate of pH_e drop in the surrounding tissue. Future work to adjust and test different doses of MIBG+glucose is necessary to optimize results in order to achieve tumor-specific acidification.

4.2   pH modulation with different doses of sodium bicarbonate

In Chapter 3, the adverse effects of chronic tumor acidosis and interest in the use of buffer therapy to re-normalize tumor pH_e were discussed. Previous experiments by our collaborators, Dr. Natarajan Raghunand and Dr. Ian Robey, attempted to reverse tumor acidosis by adding buffer solutions into drinking water of animals with implanted tumors. Although ingestion of buffer solution remains the most viable way of implementing this promising therapeutic regimen in the clinic, it has been difficult to quantify in animal models the amount of buffer solution consumed over time and the pH change associated with it. To address this, experimental work was done to try to quantify the extent of the pH change after bolus administration of known amounts of buffer solutions into animals. This section presents the experimental results of using sodium bicarbonate ($NaHCO_3$) as a pH re-normalizing buffer solution.

4.2.1 Experimental protocols

In this pilot study, experiments were done to test the magnitude of pH modulation that resulted from $200\mu l$ oral administration of 0.5M (low dose) or 1M (high dose) of sodium bicarbonate solution, as compared to saline vehicle controls. Tumor xenografts grown from GFP-transduced human prostate cancer cells, PC-3/GFP, were used with the DSFWC murine model. The DSFWC model was used due to the ease of stabilizing the WC during long periods of imaging.

The experimental protocol used in these experiments is illustrated in Figure 4.8. Before SNARF-1 was injected, the animal was imaged with the microscope using the settings shown in Table 3.1. Background signals were measured at various dwell times and the coefficients C_{ch2} and C_{ch3} of Equations 3.1 and 3.2 for the DSFWC were determined. Those equations were then used to determine the average background signal that was present across the WC before SNARF-1 was injected. Under ideal circumstances, if there was perfect registration of images throughout the experiment, background subtraction through image subtraction provides the most accuracy for measurement of fluorescent signals. However, pixel-to-pixel background subtraction was difficult to implement when non-affine position changes in the tissue occurred in the DSFWC between measurements of background and post-treatment signal. Therefore, subtracting the average background signal was used to produce more consistent results.
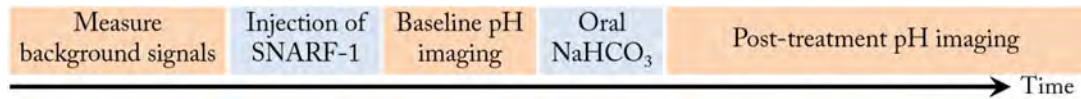
Figure 4.8: Experimental sequence of pH modulation studies.

To measure pH, $200\mu l$ of 2mM SNARF-1 was intravenously injected through a tail vein catheter. The catheter was used to ensure minimal animal motion so that background images and signal measurement images were as closely co-registered as possible. pH imaging was carried out every 5 minutes for 15 minutes after injection to allow time for the injected SNARF to equilibrate in the body. The pH_e map

measured 15 minutes after injection provides the pre-treatment baseline pH_e values of tissue in the WC.

Subsequently, the animal was recovered from anesthesia and given $200\mu l$ of either a saline control vehicle, or a low dose, or a high dose of sodium bicarbonate through a feeding tube. This procedure delivered the buffer solution directly into the gastric system of the animal. The animal was then anesthetized again and the WC was re-positioned on the microscope to achieve a similar FOV as when the baseline pH_e measurements were taken. Imaging continued at 5 minutes intervals for the subsequent hour to allow the dynamical change of pH_e following treatment to be captured.

4.2.2   Experimental results and analysis

As an example to illustrate the pH_e changes that took place after oral administration of buffer solution, the imaging results for an animal that received a low dose of sodium bicarbonate are shown in Figure 4.9. The lack of GFP signals in the middle of the GFP image suggests that there was a necrotic center in the tumor. The co-registered pre-treatment pH_e map showed that this presumably necrotic core had a low pH_e of less than 6.7. There was also differences in pH in various parts of the tumor, with parts of it more acidic than other parts. In general, the pH_e across the tissue increased after the animal received the buffer solution. However, the magnitude of pH_e modulation varied for different parts of the tissue.
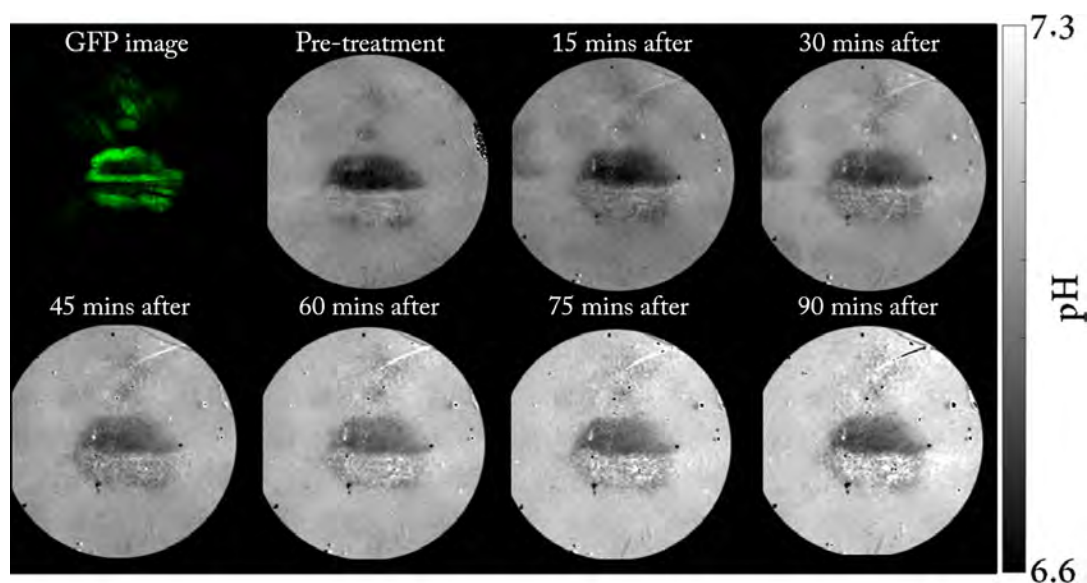
Figure 4.9: GFP image and pH_e maps of an animal that received a low dose of sodium bicarbonate. These images show that there was a gradual change in pH_e after the animal was given an oral dose of sodium bicarbonate.

Subsequent analysis was done to investigate if the magnitude of the pH_e modulation depended on the initial baseline pH_e and if the pH_e modulation showed a dose-dependent behavior. From the baseline pH_e maps, regions that had baseline pH_e lower than 6.7, between 6.7 and 7, and greater than 7 were analyzed as ROIs 1, 2, and 3, respectively.

By comparing the pH_e at each time point with respect to the baseline value, a map of the difference in pH_e was computed. The maximum increase in pH_e with respect to the baseline over the 90-minute monitoring time was recorded. The results of the maximum pH_e change reached in this animal are shown in Figure 4.10. The standard deviations of the maximum pH_e within each ROI are also given in the diagram.
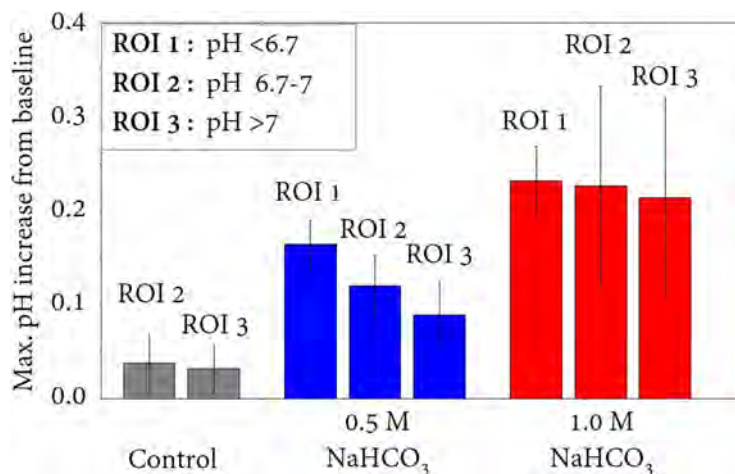
Figure 4.10: Bar diagram showing the averaged maximum increase in pH in different ROIs, in three separate experiments whereby either a saline solution, or a low or high dose of sodium bicarbonate was administered.

From the bar diagram in Figure 4.10, it can be seen that there is a dose-dependent effect on all three ROIs. The magnitude of the maximum increase in pH_e is greater when a higher dose of sodium bicarbonate was used. On the other hand, the saline solution produced very minimal change in pH_e . It is noted that in the case of the saline control, there was no region that had a pH_e lower than 6.7.

In addition, the results for the low dose showed that the magnitude of pH_e modulation depends on the baseline pH_e . The most acidic tissue region experienced the greatest amount of pH_e increase. In contrast, tissue with neutral or basic baseline condition experienced the lowest pH_e modulation. The modulation effect was less dependent on the baseline pH_e when a high dose of sodium biarbonate was used. Although there were differences in the standard deviations, the averaged maximum pH_e attained in the three ROIs were very similar.

This set of results implies that the low dose was able to reduce the pH_e difference between the acidic and less acidic region, and achieve a more uniform pH_e throughout. This may be desirable when considering the adverse effects of acid-mediated tumor invasion. However, neither the low nor the high dose of sodium bicarbonate was sufficient to re-normalize acidic tissue to neutral levels.

A similar set of experiments were done on another animal and the results are

shown in Figure 4.11. This animal did not have a very acidic tumor and, therefore, a pH of 7 was used as the threshold for ROI selection. ROI 1 and 2 represent areas with baseline pH below and above 7, respectively.
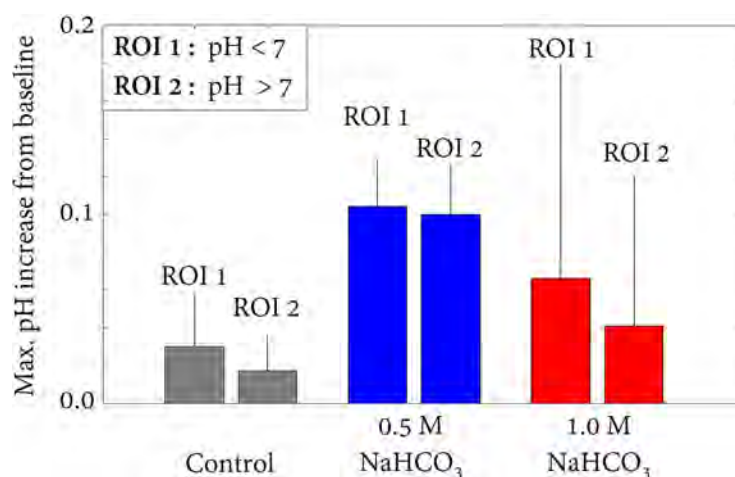
Figure 4.11: Bar diagram showing the averaged maximum increase in pH in different ROIs, in three separate experiments whereby either a saline solution, or a low or high dose of sodium bicarbonate was administered.

The saline solution produced the lowest magnitude of change in pH_e as was expected. However, for both ROIs, the magnitude of the averaged maximum increase in pH from baseline levels were larger when a lower dose of sodium bicarbonate was used. This was opposite from what was observed in the results shown in Figure 4.10. Nevertheless, the magnitude of the effect of the solutions on the tissue appears to depend on the baseline pH_e values, although the results are not significant. In other words, tissue regions with a more acidic baseline level tend to have a higher maximum increase in pH_e, regardless of dose. This is similar to what was observed in the other animal that was experimented on (Figure 4.10). Another similarity between the two animal experiments was larger standard deviations in the pH_e changes induced by the high dose of sodium bicarbonate. This may be because the higher dose of sodium bicarbonate resulted in greater perturbation of the tissue microenvironment and, thus, greater heterogeneity in the responses to the treatment.

4.2.3 Discussion of limitations of the study

There were various aspects of the experimental design that posed difficulties in the animal pH buffer studies. Firstly, the study was designed to determine the magnitude of pH_e modulation associated with ingestion of known amounts of buffer solution, because this is the desired mode of delivery of the buffer therapy if translated into the clinic. Therefore, the animal study required the buffer solution to be administered through a feeding tube while the animal was unanesthetized. With proper restraint on the animal, the gavage tube had to be inserted through the animal's oral cavity into the stomach. The process requires skills. Any motion from the animal during this process can cause the solution to enter the animal's lungs and lead to asphyxiation.

Secondly, from the results shown in Figures 4.10 and 4.11, it was observed that the amount of buffer solution given to the animal resulted in a maximum increase of approximately 0.3 pH units. Therefore, although the buffer solutions were able to result in an increase in pH_e, they were unable to renormalization the pH_e of highly acidic tissue to normal levels of approximately 7.4. Because of the difficulty of avoiding the sodium bicarbonate from precipitating in the solution when higher concentrations of the buffer solutions were prepared, several alternative buffer solutions with different pKa were explored. One of the buffer solutions explored was a solution of $Na_2CO_3 + NaHCO_3$ with either a 2:1 or 3:1 ratio. However, a large percentage of the tested animals did not tolerate the solution well.

Thirdly, because of the need to obtain baseline and post-treatment pH_e values, mis-registration of images occurs when the animal is removed from and then returned to the microscope. With simple image manipulation, lateral mis-registrations can be easily accounted for. However, image registration becomes more challenging when non-affine changes in the WC occur such as when the skin stretches. The effects on the analysis can be minimized by selecting a larger ROI and averaging over the selected area.

Another limitation of the experiment relates to the use of an injectable pH-

sensitive agent for optical measurement. The injection of SNARF itself could contribute to the fluctuations in pH_e levels observed at early imaging time points. Two examples of pH fluctuations are shown in Figures 4.12(a) and (b). The diagrams are plots of the temporal variation of the mean pH_e values within a 11x11 pixel ROI for two treated animals. Immediately after SNARF injection, a downward drift in measured pH_e was observed. The animal associated with Figure 4.12(b) experienced a more pronounced drift in the first 15 minutes after SNARF injection. These results show that the SNARF takes time to equilibriate in the animal and the amount of time it takes is variable. A possible improvement in future experiments would be to process the data to obtain pH_e maps live, rather than during post-processing, to ensure that the baseline pH_e has stabilized before a buffer solution is given to the animal.

The success of optical pH measurements depends on the delivery of the injected agent to the tissue. Figure 4.13(a) shows a GFP image of a tumor that has compromised tissue in the middle of the WC despite the presence of dense vasculature on the sides. Figure 4.13(b) shows an image from one of the PMT channels taken shortly after the injection of SNARF. Because of the lack of vasculature in the middle portion of the tumor where there was no GFP signal, there was very little SNARF fluorescence that was detected. The imaging dwell time could not be increased without saturating the signal in highly vascularized regions. As a result, the pH_e in the low fluorescence central part of the tumor could not be reliably measured in a single fluorescence measurement. The salt and pepper appearance of a region of the pH_e map, indicated with an arrow in 4.13(c), implies that the results for that region did not yield reliable pH_e readings that fall within the physical range of 6-8. In such cases, multiple images taken with different dwell times may be necessary to obtain reliable pH_e measurements for different parts of the tissue. However, multiple exposures of the fluorescent dye to excitation light leads to photobleaching effects. Repeated optical measurements of the fluorescent agent can give rise to photobleaching effects and introduce errors in the pH_e calculation. Aside from the need for multiple measurements in cases as discussed above, as the period of
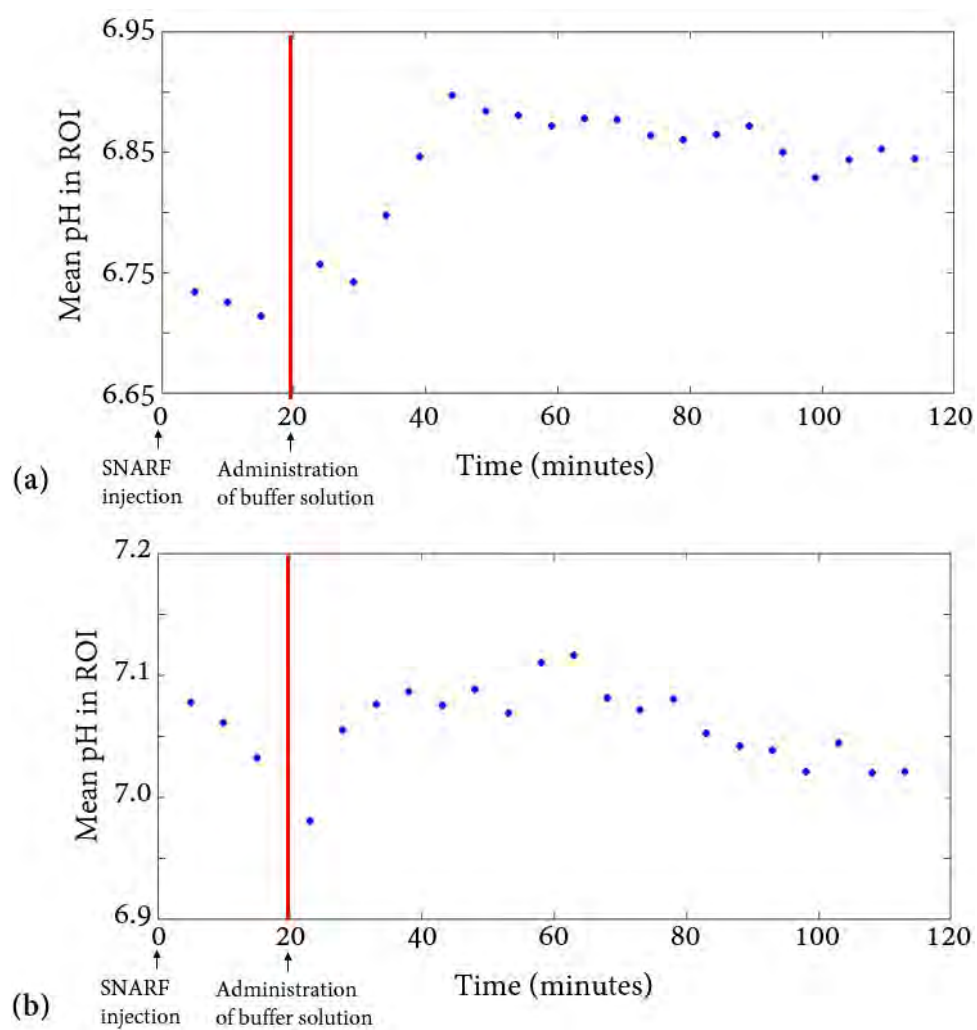
Figure 4.12: Examples of variation of mean pH_e values of a 11x11 pixel ROI of a treated animal immediately after SNARF injection. The drift in the first 15 minutes of measured pH as shown in (a) and (b) are approximately 0.3 and 0.6 pH units, respectively.

(a)   (b)   (c)
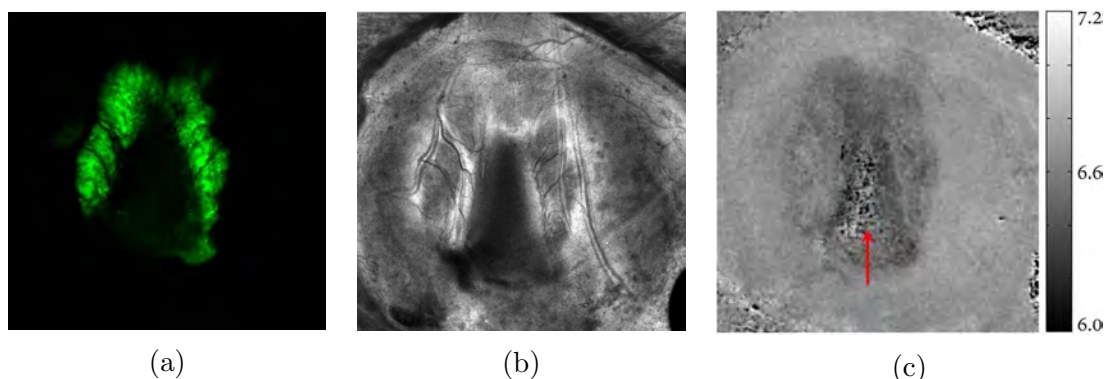
Figure 4.13: GFP image and pH imaging result. (a) GFP image of a tumor with a compromised section at the center. (b) An image from one of the PMT channels. Parts of the image suffered from low signals while other parts of it were close to saturation. The high dynamic range of the image was due to the variation of efficiency of the delivery of dye through the vascular system. (c) The resulting pH_e map yielded unreliable readings in a portion of the tissue, which has a salt and pepper appearance (indicated by an arrow). This is possibly due to poor delivery of the agent to the tissue region and, thus, low fluorescence signals.

the imaging experiments increased, the period of time over which the fluorescent agent was exposed to light increases. Moreover, SNARF is cleared slowly from the animal tissue over the imaging experiments. Therefore, longer imaging dwell times are required at later time points. Both effects may increase photobleaching of the SNARF. Reducing the frequency of imaging and keeping the number of averages small during each imaging time were steps that were taken to avoid photobleaching. To a certain extent, these sacrificed the temporal resolution for detecting dynamic pH_e changes and decreased signal-to-noise ratio.

CHAPTER 5

Fluorescence and Reflectance Hyperspectral Imaging System

5.1 Motivation

When healthy tissue turns pathological, it brings about a myriad of changes in tissue composition, cellular morphology, and expression levels of receptors. These changes alter the way tissue interacts with light and impart distinct wavelength dependent signatures in absorption, scatter, and autofluorescence properties. Thus, as compared to an anatomical image, the addition of tissue optical spectroscopy greatly enhances the information that can be obtained about the condition of the tissue.

In addition to the study of inherent spectral properties of tissue, fluorescence imaging also has wide usage in cancer research. Generally, introduction of fluorescence signals for *in vivo* imaging can either be done by means of genetic modification of cells or by injecting fluorescent agents. In the former method, specific cells are made to express fluorescent proteins via transduction and are capable of fluorescing as long as the cells are alive. The transplantation of color coded cells into a host enables delineation of those cells from surrounding tissue and facilitates the analysis of the interaction between the transplanted cells and the microenvironment [65–67]. Although it is most common to have cells transduced to fluorescence in a single color, color coding different parts of the cells (e.g. nucleus and cytoplasm) with different colors has also been reported [68]. Instead of having selective cells that express fluorescence, ubiquitous fluorescence of all cells in transgenic animals has also been reported in the literature [69].

In contrast to genetic modification, exogenous agents provide short term fluorescence. For instance, fluorescent dyes such as acridine orange can be applied topically on tissue to stain cell nuclei [70]. Dextrans conjugated to fluorophores

can be intravenously injected to visualize vascular networks and study angiogenesis [71]. Fluorecent agents such as 2-NDBG and SNARF have been used to study glycolytic metabolism [72, 73] and tissue pH [74] in animals. Furthermore, one of the most actively researched areas is to monitor the distribution and uptake of molecular probes designed to target specific biomarkers. A common stategy to visualize targeted agents is to conjugate them with fluorophores [75] or quantum dots [76, 77].

5.2   Background on tissue spectroscopy and spectral imaging systems

Spectral imaging refers to the measurement of spectral properties at every pixel on an imaging plane. When applied to a single imaging plane, spectral imaging yields $I(x,y,\lambda)$, which is often referred to as a 3D datacube, spectral cube, or image cube. A schematic of a 3D datacube is shown in Figure 5.1. Although depth-resolved spectral imaging, which measures $I(x,y,z,\lambda)$, has also been demonstrated [78, 79], the discussion here focuses on spectral imaging of a single image plane.
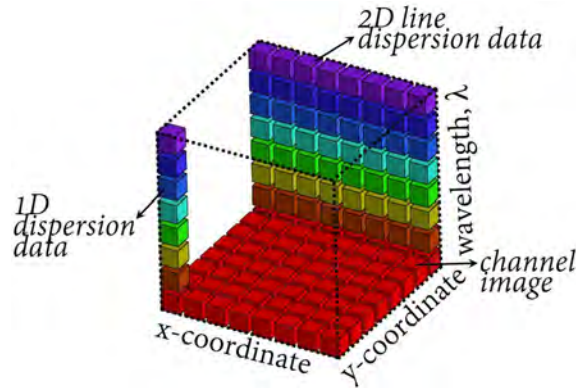
Figure 5.1: A 3D datacube showing two spatial dimensions and one spectral dimension.

The ultimate goal of any type of spectral imaging is to obtain sufficient information in the 3D datacube necessary to accomplish a given task. That can be accomplished by either employing scanning or non-scanning (snapshot) architectures. There are three main types of scanning methodologies. The first type is a point-scanning imaging system, otherwise known as a whiskbroom spectrometer.

Light from each object point is dispersed onto a 1D detector as the object is scanned in a 2D raster pattern. The second type of scan system, known as a pushbroom spectrometer, makes use of a line scanning method that requires scanning in only a single direction. At each line position, a 2D dispersed data set is recorded. Compared to a point-scanning system, the line-scanning system requires more complex calibration of a 2D detector. A channel image, which is an image that corresponds to a certain narrow band wavelength, is obtained by post hoc assembly of the dispersion data. In contrast to the aforementioned systems, the third type of scan system does not require a dispersive element. Instead, it serially captures spectral filtered images. The performance of the spectrometer varies, depending on whether the images are filtered using a filter wheel, Fabry-Perot etalon, liquid crystal filter, or acousto-optic filter. Generally, this architecture requires fewer alignment-sensitive optical elements but offers comparatively limited spectral information.

As with most scan systems, scanning spectral imagers are susceptible to motion artifacts and, depending on the method of data acquisition, may have a disadvantage of low light throughput. To address these potential problems, various snapshot spectral imagers have been developed [80]. They have the capability of acquiring a 3D datacube in a single exposure and do not require moving parts in the imaging system. However, it should be noted that the use of snapshot methods does not necessarily imply short imaging sessions. This is because of the reconstruction processes involved and the longer readout times associated with larger format detectors necessary with these systems. Recently, compressed sensing strategies have been investigated to reduce the acquired data size and allow for shorter acquisition times [80]. As a consequence of the limitation of the space-bandwidth product and the finite size of the detector, snapshot spectral imagers often have more sparse spectral information as compared to scanning spectral imaging systems.

Finally, there is another class of spectral imagers based on an interferometric Fourier-transform imaging instrument [79, 81, 82]. Both scanning and non-scanning varitations of these spectral imagers have been realized. Non-scanning Fourier-transform spectrometers tend to be much more compact than other scan-

ning spectrometers. Furthermore, common-path interferometric spectrometers have the advantge of being insensitive to environmental disturbances.

There has been inconsistent use of terminology in naming the various spectral imaging systems in the literature. In this dissertation, spectral imaging refers to any measurement of spatial and spectral information. Multispectral imaging refers to the use of spaced spectral bands during data acquisition, while hyperspectral imaging measures data across a certain spectrum in a more finely sampled manner.

5.3   Description of the imaging system and operation

The reflectance and fluorescence hyperspectral imaging system shown in Figure 5.2 was developed to study tumors growing under the MWC [83]. The system was modified from an optical setup that was originally built as the optical scan unit for a confocal microendoscope [84]. In the confocal microendoscope design, a 10X microscope objective was used to couple light into an imaging fiber bundle. Although that lens can be used to obtain high-resolution images of the MWC, the limited field of view of approximately 720μm is unsuitable for applications that require imaging of the entire MWC. To increase the full field of view (FOV) to approximately 7.4mm, a 200mm focal length UV-Vis achromatic object lens (Edmund Optics, #49-377) was used in place of the microscope objective.

The imaging system utilizes a laser for fluorescence imaging and a broadband source for reflectance imaging as shown in Figure 5.2(a) and (b), respectively. In the latter case, illumination is accomplished using a broadband halogen lamp with the light coupled into a 1.125 diameter fiber ring light-guide (Edmund Optics, #54-175). The annular output beam has an anglur spread of approximately 37°. At a distance of 30mm from the tissue, this arrangement produces a reasonably uniform illumination over the full field of the MWC with virtually no direct specular reflection of the illumination into the detection path. The backscattered light from the sample is imaged by a set of lenses and a scanning mirror onto a 25m wide slit aperture. The slit aperture is used to pass the backscattered light that originates from a 35.7μm

wide line on the object. The location of the line on the object is determined by the angle of the object scan mirror.

For spectral imaging, the light passing through the slit aperture is directed through a collimating lens, off a second scan mirror set at a fixed off-axis position, through a 45° BK7 glass prism, where it is dispersed and imaged by a camera lens to a 12-bit CCD camera (Photometrics, Quantix:57) as shown in Figure 5.2(c). The 512$\times$512 pixel CCD camera employed has 13x13μm pixels and a readout rate of 10 fps. For a given position of the object scan mirror, the 2D image data on the CCD corresponds to a spectral-spatial image with spatial information along the vertical line of the slit and spectrally dispersed information perpendicular to the slit (horizontal direction). By reading out multiple frames of image data as the object scan mirror scans the line of light collection across the sample, a data set with the two spatial dimensions of the MWC and a reflectance spectrum at each spatial pixel location is obtained in less than 1 minute (512 frames of data at 10 fps = 51.2s). The FOV in the direction along the slit is determined by the CCD. The FOV in the perpendicular direction is determined by the rate at which the object mirror scans, and the scan speed is set such that the FOV in both directions are matched.

Fluorescence spectral imaging is accomplished with a laser instead of using the broadband source. In this case, a fiber-coupled 488nm laser and an achromatic lens were used to create a collimated laser beam that passes through a cylindrical lens to produce a line illumination at the sample. This illumination line is conjugate to the slit aperture. The fluorescence emission goes through the same imaging path as described for reflected light imaging.

In addition to spectral imaging, live real-time white-light reflectance or fluorescence imaging of the MWC can be obtained by using the appropriate light source and scanning both object and detection scan mirrors synchronously at 5Hz to match the camera's readout rate of 10 fps. As illustrated in Figure 5.2(d), the scan mirror close to the camera operates over an angular range such that the light reaching the camera is not dispersed by the prism. It should be noted that faster frame rates can be achieved with a camera that operates at a higher readout rate. The live

real-time mode of imaging is useful for quickly positioning and focusing the MWC in the field of view of the instrument or for visualizing the tumor location for correlation to reflectance mode spectral image data. The system is configured to operate in an off-axis configuration during spectral imaging (Figure 5.2(c)) and an on-axis configuration for live broadband fluorescence or white light reflectance imaging (Figure 5.2(d)), in order to facilitate rapid switching between different imaging modes without the need to move the alignment-sensitive dispersion prism. The 2D optical layout of the spectral imaging system is illustrated in Figure 5.3.
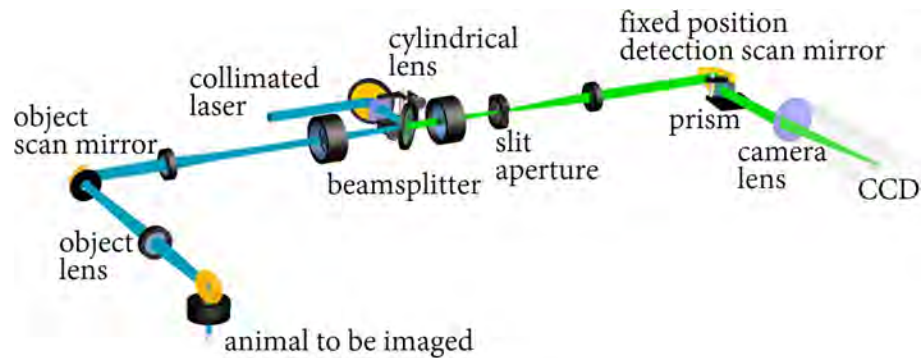
(a) Fluorescence spectral imaging with a collimated laser. Line illumination of the MWC is enabled by a cylindrical lens placed before the beamsplitter. Fluorescence emission is directed through the slit aperture and deflected by a scan mirror in a fixed off-axis position onto a prism where it is dispersed and imaged onto a CCD.
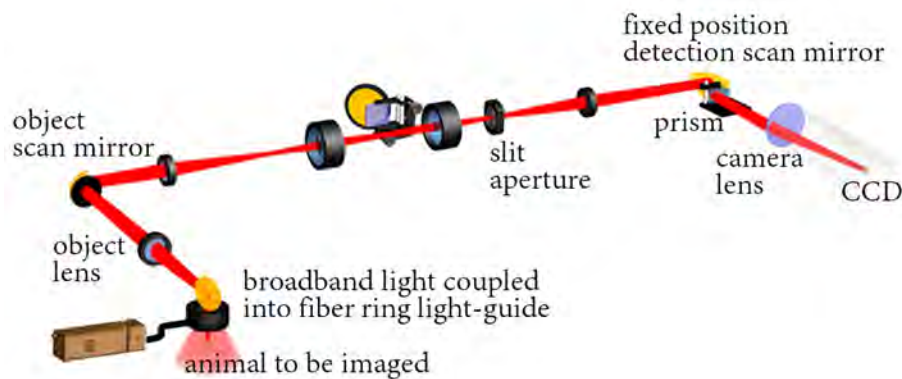
(b) Broadband reflectance spectral imaging with a broadband light source coupled into a fiber ring light guide. Backscattered light from the MWC is directed through the slit aperture and deflected by a scan mirror in a fixed off-axis position onto a prism where it is dispersed and imaged onto a CCD.
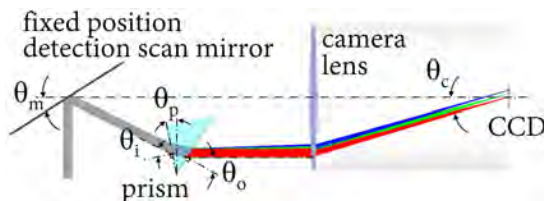
(c) A schematic showing the detection scan mirror in a fixed off-axis position. It deflects the beam of light onto a prism where it is dispersed and imaged onto the CCD.
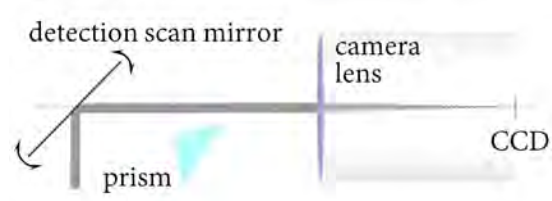
(d) Live imaging can be done by rotating the detection scan mirror to avoid the prism and scanning it synchronously with the object scan mirror.

Figure 5.2: Different configurations of the imaging system.
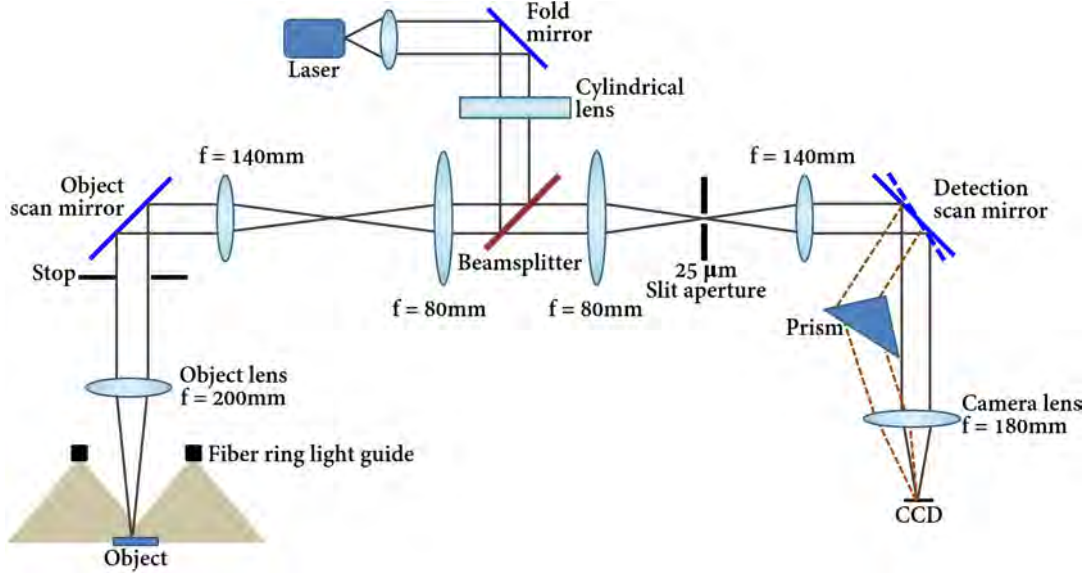
Figure 5.3: 2D optical layout of the spectral imaging system.

5.4 Spectral calibration of the system

Due to the nonlinear spectral to spatial mapping of the prism, calibration of the spectral measurements is required. With reference to Figure 5.2(c), the system operates at minimum deviation for $\lambda_{\text{ref}} = 632.8$nm. In addition, the exiting angle of the light with respect to the normal of the prism (θ_o) for λ_{ref} is such that the light propagates parallel to the optical axis of the camera lens. Satisfying these two conditions facilitates the optical alignment procedure. At λ_{ref}, the incident angle on the prism required for minimum deviation, θ_i is given by:

$$\theta_i = \sin^{-1}\left[n\left(\lambda_{ref}\right)\sin\left(\frac{A}{2}\right)\right], \tag{5.1}$$

where, in this case, the prism angle, $A = \frac{\pi}{4}$ and n is the wavelength-dependent refractive index of the prism. The angle of the detection scan mirror (θ_m) and tilt of the prism (θ_P) are aligned to achieve the incidence angle θ_i required for minimum deviation and make the exit angle parallel to the optical axis of the camera lens for λ_{ref}. In practice, this is equivalent to imaging the λ_{ref} light to the center of the CCD. The dispersion equation that governs θ_o for an arbitrary wavelength λ, is given by:

$$\theta_o(\lambda) = \sin^{-1}\left[\sin A\sqrt{n^2(\lambda) - \sin^2\theta_i} - \sin\theta_i\cos A\right]. \tag{5.2}$$

The angle of the incident light on the CCD with respect to the optical axis of the camera lens is given by:

$$\theta_c(\lambda) = \theta_o(\lambda) + \theta_p + A - \frac{\pi}{2}. \tag{5.3}$$

Using small angle approximations,

$$\theta_c(\lambda) \,.\, f = x(\lambda), \tag{5.4}$$

where f is the effective focal length of the camera lens and x is the horizontal position where the beam of light is focused on the CCD. By considering the centers of two adjacent pixels, which are separated by a distance equivalent to 1 pixel size (p), the difference in angles is given by

$$\theta_c(\lambda_2) - \theta_c(\lambda_1) = \frac{p}{f}. \tag{5.5}$$

Ideally, an on-axis point source emitting at λ_{ref} would be imaged onto the center pixel of the CCD. The pixel-to-wavelength assignment along the horizontal direction of the CCD can be calculated based on Equations 5.2 - 5.5. Corrections to this initial spectral calibration are required due to the presence of chromatic aberration, breakdown of the small angle approximations, and aberrations that depend on where the beam hits the camera lens. In order to estimate these corrections, reflectance spectroscopy with a broadband light source was performed using a calibrated multi-component doped Spectralon wavelength standard (Labsphere, Inc) that has several distinct reflectance minima at specific wavelengths. The wavelength calibration adjustments required to match the measured spectra to the NIST-traceable calibration data supplied by Labsphere (see Figure 5.4(a)) were computed. A similar procedure was done separately with 488.0, 543.5 and 632.8nm lasers. The combined calibration result is fitted to a 3rd order polynomial and the result is shown in Figure 5.4(b).

In the absence of aberrations, an extended source with light at λ_{ref} would be imaged onto a vertical straight line with the same x-coordinate on the CCD. Then,

every point of the slit image would share the same dispersion calibration. However, this was not the case in practice and the line image had a subtle curvature. Along the y-axis, the deviation of the x-coordinate from the middle position typically varies between 2 and 4 pixels. Due to the non-linearity of the dispersion, spectral error is more pronounced at longer wavelengths and a 4 pixels deviation translates to greater than 10nm spectral error at λ=800nm. Therefore, instead of a single calibration, a y-dependent spectral calibration curve was used to achieve better spectral accuracy across the entire 3D data set.

The spectral linewidth (spectral resolution) is determined by the convolution of the calibrated spectral to spatial mapping function with the FWHM of the slit aperture image on the detector. Figure 5.5(a) shows a line image of the slit obtained by illuminating a uniform reflectance Spectralon standard (Labsphere, Inc) with a 632.8nm laser coupled into the fiber ring light-guide. A plot of signal strength through the center of that image is shown in 5.5(b). From that plot, the FWHM of the slit image was determined to be 2.8 camera pixels, which corresponds to 36.4μm . The FWHM of the slit image does not change significantly with wavelengths 488.0, 543.5 and 632.8nm. The resulting spectral resolution of the system is shown in Figure 5.5(c). The spectral resolution of the system varies from about 2nm at 400nm wavelength to 11nm at 800nm wavelength, due to the non-linear dispersion of the prism. This results in roughly 100 independent spectral channels of measurement across the spectral band. Thus, the system performance is consistent with its definition as a hyperspectral imaging system.
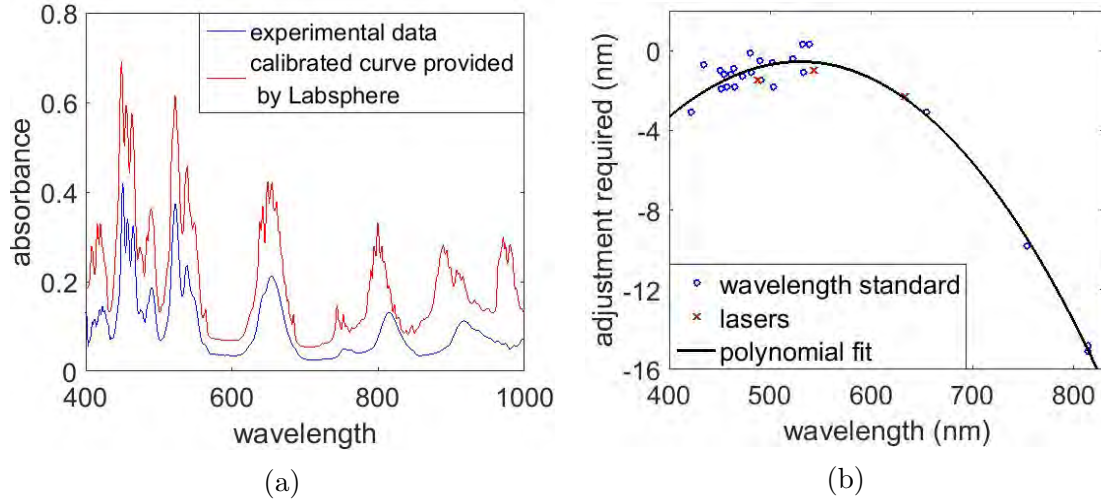
Figure 5.4: Refinement of spectral calibration. (a) Comparison of measured absorbance of multi-component Spectralon against the calibrated absorbance data supplied by Labsphere. (b) Adjustments required for spectral-spatial calibration mapping are computed from the data in (a) and with the use of 488nm, 543.5nm, and 632.8nm lasers.
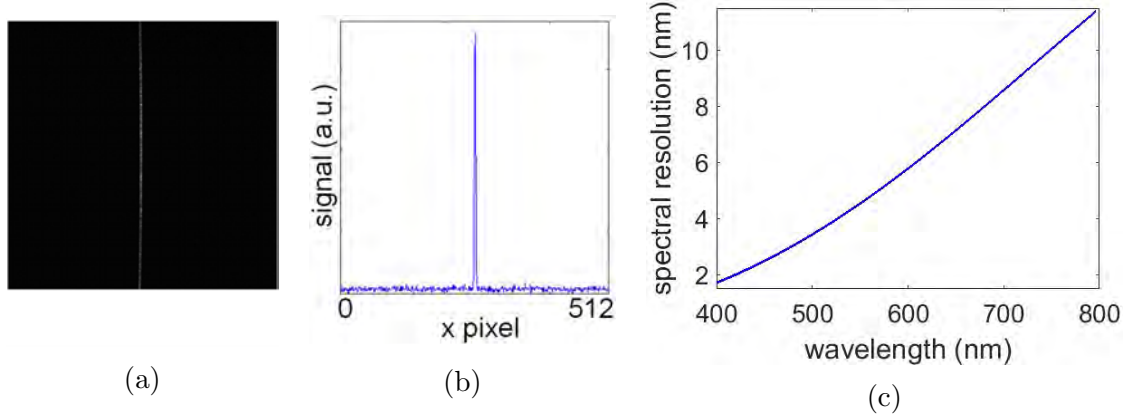
Figure 5.5: Spectral resolution of the system. (a) A line image of the slit aperture obtained by illuminating a R≈99% Spectralon standard with a 632.8nm laser through a fiber ring light guide. (b) Plot of signal strength through the center of the image (a). (c) The resulting wavelength dependent spectral resolution of system.

In addition, experiments imaging a point source was performed to evaluate the system's spatial resolution. Instead of imaging in reflectance mode with the fiber ring light guide, a laser was coupled into a single mode fiber. The slit aperture in the system was aligned to maximize the amount of light imaged onto the detector.

Figures 5.6(a) and (b) show images of the point spread function (PSF) of a 543nm laser point source without and with the slit aperture in the system, respectively. The FWHM of the PSF (in the direction perpendicular to the slit) that was taken with the slit in the system is slightly narrower than the PSF obtained with the slit removed. In the direction along the slit, the FWHM of the image with the slit is the same as the FWHM of the image without the slit. This is shown in Figure 5.5. This implies that the spectral resolution of the system is slightly improved with the use of the slit. However, the light efficiency decreased as the total detected signal of the point source with the slit in place was 85% of what was detected when the slit was removed. The result in Figures 5.6(a) and (b) also gives the spatial resolution of the system. It is approximately 39μm in the direction along the slit and 36.4μm in the dispersion (or spatial scan) direction.

(a)   (b)
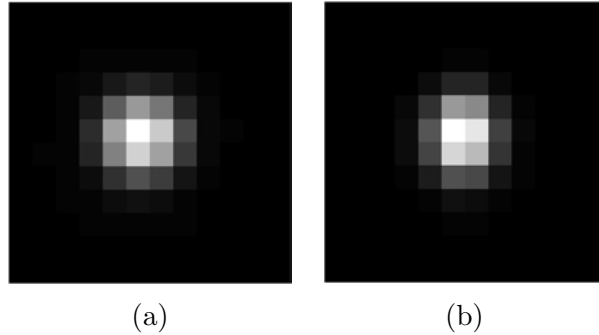
Figure 5.6: Images of PSF (a) without and (b) with the slit aperture (oriented vertically) in the system.

The key parameters of the spectral imaging system are summarized in Table 5.1.

Table 5.1: Key specifications of spectral imaging system

Stop diameter (mm)	11
Object space NA	0.027
Image space NA	0.031
Magnification	0.9
Full FOV (mm)	7.4
Slit width (μm)	25
Slit width of conjugate in object space (μm)	35.7
FWHM of slit image on CCD (μm)	36.4
Camera frame rate (fps)	10

5.5 Stray light control in the system

Stray light in the imaging system has the potential to reach the detector and introduce inaccuracies in the spectral measurements. To understand how the major sources of stray light in the system affect the measurement and how the effect can be minimized, the optical system was modelled in stray light analysis software (FRED, Photon Engineering). With the exception of the Nikon camera lens, all other lenses were modelled with the optical prescriptions and surface coating provided by the manufacturer. The camera lens was modelled as a perfect lens with a 180mm focal length. In the initial step, all mirrors were considered 100% reflective and all mounting structures and baffles were considered 100% absorptive. In the actual system, the mounts were made of black anodized aluminum and baffles were either lined with matte black anodized aluminum or black flocked material. Other than at large incidence angles, these materials typically have very low reflectance in the visible and NIR wavelength range. The prism is made from uncoated N-BK7 and it's optical properties were calculated based on the incidence angle and wavelength dependent Fresnel coefficients. Figure 5.7 depicts the optical system that was modelled in software.
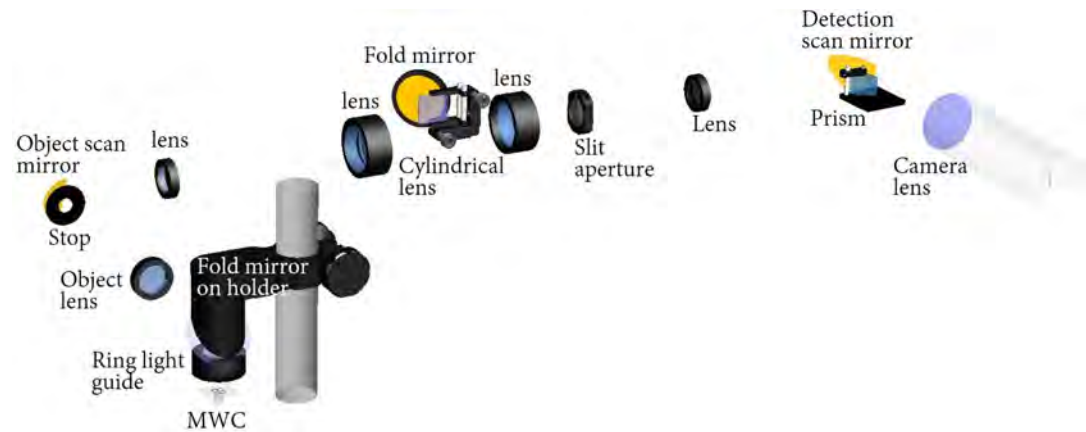
Figure 5.7: Diagram of the optical system without any baffles to manage stray light.

There are two major sources of stray light in the system. Firstly, the fiber ring light guide that was used to illuminate the MWC has an output beam with an angular spread of 37°. Figure 5.8 shows that, in addition to the MWC, its surroundings are also illuminated by this light source. Because of this, scattered light from the region outside the MWC is a potential source of stray light in the imaging system. The second major source of stray light comes from the fresnel reflection on the uncoated surfaces of the prism.
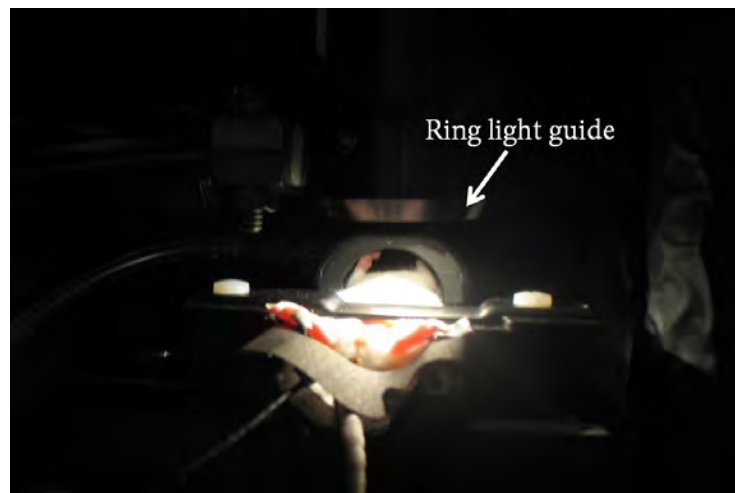
Figure 5.8: A photograph of the animal being illuminated by the ring light guide. The output beam reaches the MWC as well as surrounding areas, resulting in potentially dentrimental stray light.

To address the first issue, it is important to find out where the light rays that ultimately reach the CCD originate from. Incident rays on the CCD that do not originate from the MWC are considered as stray light. The approach to this problem is to recognize that all light is going to be filtered by the slit aperture. Therefore, it is equivalent to find out where all the rays that can be transmitted by the slit aperture originate from. This was investigated by creating random light sources on the slit aperture that emit into random directions into an angular range and tracing the rays backwards. The angular range used in the simulation was set by the clear aperture of the lens right next to the slit aperture. A diagram of the raytrace result is shown in Figure 5.9(a). The raytrace path report shown in Figure 5.9(b) shows that all the light from the slit either ended on absorbing surfaces or on a line at the object plane. This gives assurance that only information that originated from the object plane will be transmitted through the slit aperture and reach the CCD. Figure 5.9(c) shows a directional spot diagram of the rays that reach the object plane. It indicates that the incidence angles on the object plane are within $\pm\ 2^o$. This implies that, on the object plane, only reflected light within this angular range will be imaged onto the CCD.

	Total Power	Ray Count	Last Entity	Previous Entity
0	0.6415	6719	buildsystem_old.edmund 49389_N-SF10.Surface 8	buildsystem_old.edmund 49389_N-SF10.Surface 9
5	0.0923	945	buildsystem_old.50mm lens mount 3.Front Face	buildsystem_old.edmund 49389_N-BAF10 1.Surface 11
2	0.0683	716	buildsystem_old.30mm lens mount 2.Front Face	buildsystem_old.edmund 49389_N-SF10.Surface 8
3	0.0564	628	buildsystem_old.STOP.stop	buildsystem_old.scan mirror 1.Reflecting Surface
1	0.0394	397	buildsystem_old.edmund 49389_N-SF10 1.Edge	buildsystem_old.edmund 49389_N-SF10 1.Surface 13
4	0.0202	230	buildsystem_old.dummy at obj.Surface	buildsystem_old.45deg fold mirror.reflecting surface
7	0.0179	183	buildsystem_old.edmund 49389_N-BAF10 1.Edge	buildsystem_old.edmund 49389_N-SF10 1.Surface 12
10	0.0044	47	buildsystem_old.30mm lens mount 2.Inner Wall	buildsystem_old.edmund 49389_N-SF10.Surface 8
8	0.0032	33	buildsystem_old.50mm lens mount 3.Inner Wall	buildsystem_old.edmund 49389_N-BAF10 1.Surface 11
9	0.0032	33	buildsystem_old.50mm lens mount 4.Inner Wall	buildsystem_old.edmund 49389_N-BAF10 1.Surface 11
12	0.0024	24	buildsystem_old.50mm lens mount 4.Inner Wall	Optical Sources rays on slit
6	0.0014	16	buildsystem_old.LAO140 melles griot N-BK7.Surface 5	buildsystem_old.LAO140 melles griot N-BK7.Surface 6
11	0.0014	16	buildsystem_old.LAO140 melles griot N-BK7.Edge	buildsystem_old.LAO140 melles griot N-BK7.Surface 6
13	0.0008	9	buildsystem_old.LAO 140 melles griot N-SF5.Edge	buildsystem_old.LAO 140 melles griot N-SF5.Surface 7
14	0.0003	3	buildsystem_old.50mm lens mount 4.Front Face	Optical Sources rays on slit
15	0.0002	3	buildsystem_old.LAO 140 melles griot N-SF5.Edge	buildsystem_old.LAO140 melles griot N-BK7.Surface 6

Figure 5.9: Raytrace results with a line source on the slit aperture. (a) Diagram of the raytrace results. (b) Raytrace report of the raypaths. (d) Directional spot diagram of the rays that reach the object plane.

Stray light due to the fresnel reflections off the uncoated surfaces of the prism was also investigated. A 400-900nm broadband line source on the center of the object plane was used. Based on the results shown in Figure 5.9(c), although the rays that are backscattered and/or reflected from the object plane have a much larger angular spread, only the rays that are within $\pm 2^o$ are imaged onto the CCD. Thus, a line source with a $\pm 2^o$ angular spread was used. The raytrace results are shown in Figures 5.10(a)-(c).

The fresnel reflections from the surfaces of the prism create several beams of stray light (rays in blue) that go in different directions. Two beams, including one of the fresnel reflection beams that hit the edge of the scan mirror, were directed towards the object. One of the beams reached the metalic post that supported the 45° fold mirror and was scattered outwards in a range of angles. Although none of the scattered light managed to re-enter the imaging system and reach the detector, there is a risk of unintended consequences if the stray light is reflected off the user operating the system or other items on the optical table. Therefore, a lightbox made

with black hardboard was built around the system. The hardboard was lined with black anodized aluminum foil to further minimize its reflection. In addition, a piece of hardboard was placed around the objective lens close to the ring light guide to block unwanted light that is reflected from the animal.

By assuming that the lightbox is 100% absoprtive, the result of the raytrace of the system is shown in Figure 5.10(b). In this case, the lightbox absorbs the stray light and prevents it from travelling to critical parts of the system. An additional raytrace was done by setting the reflectivity of the lightbox to 20% and that result is shown in Figure 5.10(c). The darker blue rays represent the fact that the beams of stray light lose energy as the number of reflections increases. From that result, it is clear that the lightbox is effective in absorbing the bulk of the unwanted fresnel reflections off the prism. Light that is reflected off the surfaces of the lightbox are of very low energy and no significant amount of stray light reached the CCD. More importantly, stray light is contained and will not reach places that are close to the object.

(a)

(b)

(c)
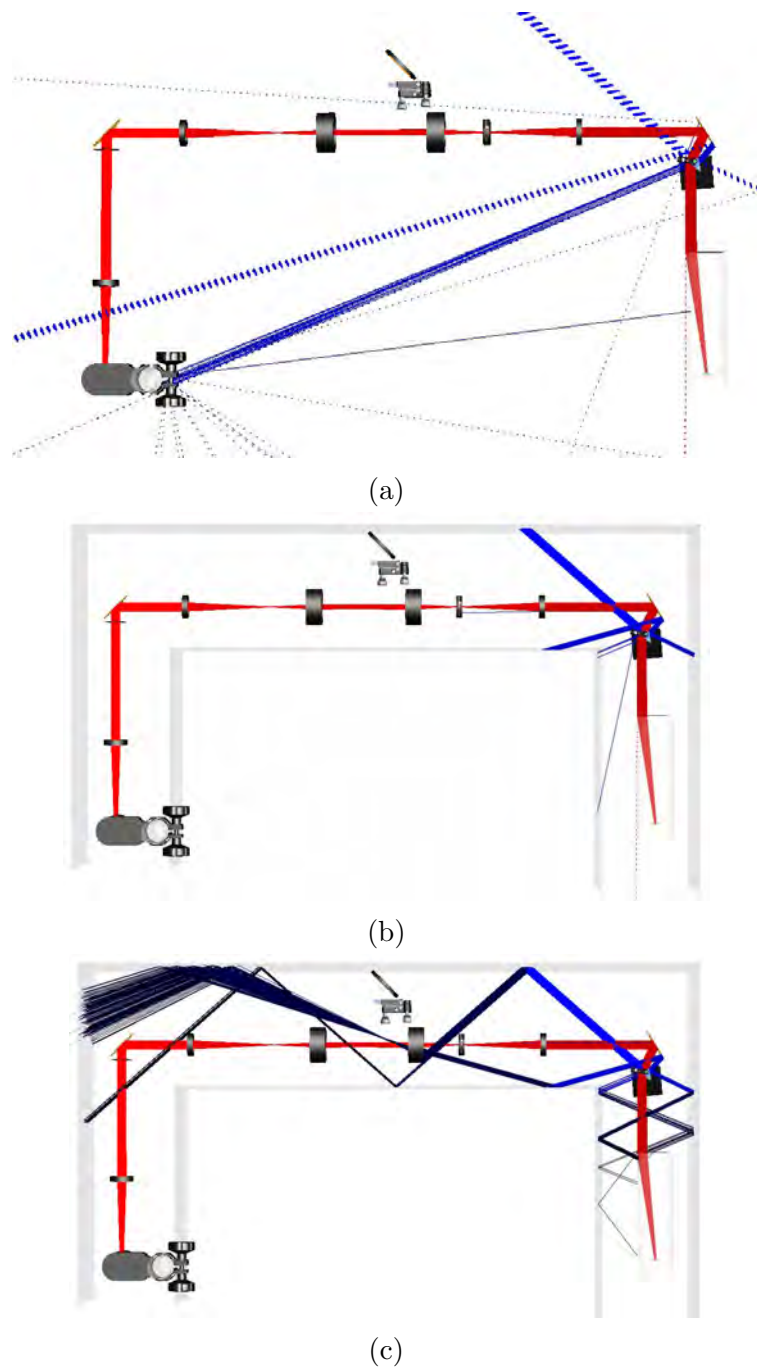
Figure 5.10: Stray light analysis of the spectral imaging system with and without having a light box. A line source on the object plane that was conjugate to the slit aperture was used. Diagram of the raytrace results (a) without a light box, (b) with a perfectly absorbing light box, and (c) with a light box with a 20% reflectance surface.

CHAPTER 6

Experimental Results with *In Vivo* Fluorescence and Spectral Imaging of the MWC

6.1 Hyperspectral fluorescence imaging

To demonstrate the hyperspectral fluorescence imaging capability of the system, an experiment was performed in which spectral fluorescence data were collected before and after injection of 100μl of 30mM fluorescein via a tail vein catheter into a MWC mouse with an MDA-MB-231-GFP breast cancer tumor. A 488nm laser efficiently excites the fluorescence of both GFP and fluorescein.

Figure 6.1(a) shows a spectral projection image of the GFP signal from the tumor obtained before fluorescein injection. A spectral projection image is an image obtained by summing all spectral channel images in the datacube (Figure 5.1). Despite a visible vascular network around the tumor, there is a necrotic core in the center. Figure 6.1(b) shows an example of a single dispersion image that corresponds to a line at the center of the MWC. After fluorescein injection, the agent was rapidly transported to the tissue within seconds and the resultant spectral projection image is shown in Figure 6.1(c). There is little fluorescein in the necrotic core due to the lack of vasculature in that region. Figure 6.1(d)is a plot of normalized emission spectral of GFP ($S_{GFP}(\lambda)$) and fluorescein ($S_{fl}(\lambda)$). The former was obtained by measuring the signal from the tumor before injection of fluorescein while the latter was obtained by measuring the post-injection fluorescence signal in regions where there was originally no GFP signal but significant signal after injection.

The spectral emission profiles of GFP and fluorescein are very similar and separation of the two signals requires techniques such as spectral unmixing [85]. In a simple first order approximation, a linear unmixing model expressed as

$$S_{\mathrm{refl}}(\lambda) = C_{\mathrm{GFP}}S_{\mathrm{GFP}}(\lambda) + C_{\mathrm{fl}}S_{\mathrm{fl}}(\lambda) + C, \qquad (6.1)$$

was used to determine the amount of GFP and fluorescein signal at each pixel location. $S_{\mathrm{refl}}(\lambda)$ denotes the mean detected reflected signal within a 11x11 pixel region around a point. Taking a mean of a small region helps smooth out noise and improve performance of the spectral unmixing procedure. C_{GFP} and C_{fl} are proportionality coefficients representing the relative signal strengths of the two fluorophores. Lastly, C is a constant. Figure 6.1(e) and (f) show the resulting maps of C_{GFP} and C_{fl}, respectively. The R^2 value gives an indication of goodness of fit and is defined by

$$R^2 = 1 - \frac{SS_E}{SS_T}, \qquad (6.2)$$

where SS_E is the sum of squared errors and SS_T is the total sum of squares, defined by

$$SS_E = \sum (y_i - \hat{y}_i)^2, \qquad (6.3)$$

$$SS_T = \sum (y_i - \bar{y}_i)^2. \qquad (6.4)$$

Here y_i is the experimental data, $\hat{y}_i$ is the data fitted to the mathematical model, and $\bar{y}_i$ is the mean of the experimental data within the fitting range. The R^2 value was computed for every fitted data point, 92% of which had $R^2 \geq 0.99$. The experimental data and decomposed spectral components for three locations on the MWC, indicated by p_1-p_3 on Figures 6.1(e) and (f), are shown in Figures 6.1(g)-(i), respectively. The decomposed spectral curves for location p_1 show that there is fluorescence from GFP (green line) but not from fluorescein (blue line). The fitted curve in red is the sum of the fluorescence curves from GFP and fluorescein. The results show that there is a good fit (R^2=0.9939) to the measured fluorescence spectral curve. At location p_2, there is fluorescence from fluorescein but not from GFP.

Similarly, the spectral decomposition result shows good agreement with experimental results. Lastly, p_3 is at a location where there is fluorescence from GFP and fluorescein. The decomposed spectral curves shown in Figure 6.1(i) indicate that the fluorescence from fluorescein is higher than that from GFP in that location.

Despite the good fits and the high R^2 values, there are some discrepancies between the measured GFP map before fluorescein injection (Figure 6.1(a)) and that derived from post-injection data (Figure 6.1(e)). This is possibly because spectral variations arising from factors such as tissue pH and concentration of fluorophores have been neglected [86].
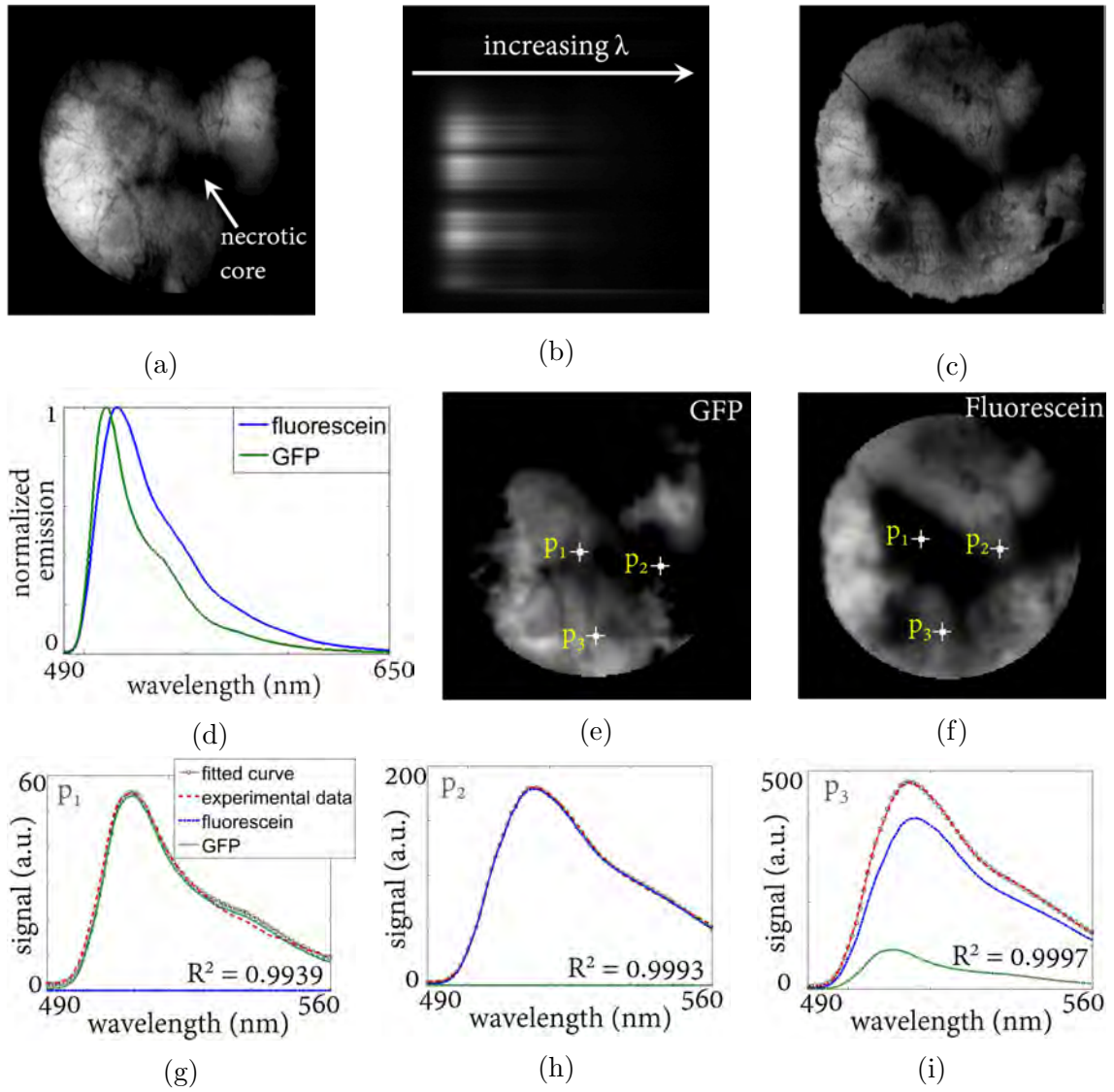
Figure 6.1: Hyperspectral fluorescence imaging results. (a) A fluorescence image of GFP. (b) A single dispersion image of a line through the center of MWC. (c) A fluorescence image after fluorescein injection. (d) Normalized emission spectra of fluorescein and GFP. (e)-(f) Maps of C_{GFP} and C_{fl} derived from spectral unmixing. (g)-(i) Plots show the measured data, fitted curves, and decomposed spectral components at three locations marked P_1-P_3 in (e) and (f).

6.2 Absorbance measurement and oxygen saturation estimation

6.2.1 Different forms of oxygen saturation

Another application of the optical imaging instrument is to obtain spectrally resolved absorbance measurements in order to map out the tissue oxygenation saturation levels in the tissue below the MWC.

There are four sites, known as heme groups, on each mammalian hemoglobin molecule that can carry oxygen. Oxygen saturation is a measure of the fractional oxygen loading on the total number of heme groups on all hemoglobin available in blood. Depending on where in the circulatory system the blood is being probed, there are four main types of oxygen saturation measurements. They are namely arterial (SaO_2), central venous ($ScvO_2$), mixed venous (SvO_2), and tissue (StO_2) oxygen saturation. SaO_2 measures the oxygen saturation of arterial blood before it is being delivered to different parts of the body. Therefore, SaO_2 values are typically greater than 85% in healthy subjects. A pulse oximeter is the most commonly used tool to measure SaO_2. In contrast, $ScvO_2$ and SvO_2 measure the oxygen saturation of deoxygenated blood that is in the return veneous system. $ScvO_2$ and SvO_2 are usually measured in the cava vein and pulmonary artery, respectively. Unlike the first three measurements, StO_2 measures oxygen saturation in the tissue microcirculation where oxygen is extracted from capillaries and diffusing towards tissue cells. Because oxygen is being extracted and used by tissue, StO_2 is usually lower than SaO_2.

The tissue under a MWC contains both arteries and microcirculation, and therefore the absorbance and oxygen saturation measurement of a MWC is a result of a mix of SaO_2 and StO_2. For simplicity, SaO_2 was used to label the results obtained in this work.

6.2.2 Mathematical modeling of absorbance

Because of the geometry of the MWC model, absorbance is described here in the context of epi-illumination and detection of the diffusely reflected broadband light.

Absorbance, as a function of wavelength, is defined as

$$A(\lambda) = -log\left[\frac{I(\lambda)}{I_o(\lambda)}\right],\qquad(6.5)$$

where I and I_o are the wavelength dependent intensities of light reflected off the object and the incident light, respectively. In order to calculate the absorbance of tissue under a MWC, two separate measurements were made. The first measurement (I_{sp}) was made with a Spectralon standard that has a uniform $R_{sp} \approx 99\%$ reflectance in the visible wavelength range. The second measurement (I_{MWC}) was made with the same illumination source but with the object (MWC) in place. Since the two objects are imaged under the exact same imaging conditions, system variations that arise from wavelength-dependent quantum efficiency of the CCD and optical properties of lenses are removed. With these two measurements, absorbance is calculated as follows:

$$A_{\text{meas}}(\lambda) = -log\left[\frac{R_{sp}(\lambda)\ I_{\text{MWC}}(\lambda)}{I_{\text{sp}}(\lambda)}\right].\qquad(6.6)$$

As a first order approximation, absorption was treated as a sum of terms associated with each chromophore in the tissue. In the visible wavelength range, the main chromophores of interest are fat, blood oxyhemoglobin (HbO2), and deoxyhemoglobin (Hb). The measured absorbance curve in the 480-620nm wavelength range was fitted to the following equation,

$$A_{\text{fit}}(\lambda) = k_1\left[SaO_2\ \epsilon_{\text{oxy}}(\lambda) + (1 - SaO_2)\ \epsilon_{\text{deoxy}}(\lambda)\right] + k_2\ \epsilon_{\text{fat}}(\lambda) + k_3,\qquad(6.7)$$

where ϵ_{oxy}, ϵ_{deoxy} and ϵ_{fat} are the molar extinction coefficients of HbO2, Hb, and fat, respectively, and k_1, k_2, and k_3 are constants. SaO_2 is the fractional oxygen saturation. It is expressed as

$$SaO_2 = \frac{[\text{HbO2}]}{[\text{Hbt}]} \approx \frac{[\text{HbO2}]}{[\text{HbO2}] + [\text{Hb}]},\qquad(6.8)$$

where square brackets denote concentration of the components in blood. [Hbt] is the total hemoglobin concentration in blood.

The wavelength dependent extinction coefficients of oxyhemoglobin and deoxy-hemoglobin of rat blood [87] were used as an approximation for mouse blood, and the wavelength dependent extinction coefficient of mammalian fat [88] was used for the fat component. The measurements and subsequent data fitting yield a 2D map of the local blood oxygenation in the tissue under the MWC. It should be noted here that breast cancer xenografts in the MWC mouse model are typically small (less than 300 mm^3) and grow close to the surface of the imaging windows. Because visible light penetrates only a few millimeters into mammary tissue [89], the SaO_2 maps reflect the average oxygenation status of a slab of tissue near the tissue/glass interface of the MWC.

6.3   Monitoring SaO_2 changes in the MWC over days

Hyperspectral reflectance measurements of a MWC animal were acquired and used to estimate the SaO_2 in the tissue below the glass coverslip. Tumor growth and oxygenation levels were monitored as the tumor developed over a period of several days. Figures 6.2(a)-(c) show GFP images from days 8, 11, and 13 after cell injection. SaO_2 maps from corresponding time points are shown in Figures 6.2(d)-(f). The k_2/k_1 parameter (see Equation 6.7) is a measure of fat content relative to blood. Normalized images of the ratio are given in Figures 6.2(g)-(i). Much of the fat is observed to exist in the tissue at the edge of the MWC and little fat content is present within the tumor, as expected.

In the GFP image of day 8 (Figures 6.2(a)), aberrant angiogenesis can be seen on the top left of the tumor indicated by the arrow marked "v". The co-registered SaO_2 map in Figures 6.2(d) shows that this part of the tumor is significantly more oxygenated than tissue in the surrounding region. In contrast, a vascular network was noticeably absent in the central part of the tumor. The measured SaO_2 indicates the occurrence of hypoxia in that region, which is common in aggressive tumors where the growth rate is faster than what the vascular network can support.

Three days later, Figure 6.2(b) shows that neovasculature had become more

prevalent at the periphery of the tumor. The disappearance of GFP signal in the middle indicates that tumor necrosis (marked "n") has occurred and GFP expressing tumor cells in this region have died even though the extent of low oxygen saturation has actually reduced in size. Figure 6.2(j) is a photograph of the MWC taken on that day and the necrotic region is visibly darker than surrounding tissue. On day 13, Figure 6.2(f) shows that the oxygen supply has redistributed with the region of lower oxygen saturation shifted to the right. Figures 6.2(k) and (l) show measured absorbance spectra and the spectral fits to the mathematical model in Equation 6.7 at two different locations in the MWC marked p_1 and p_2, respectively (Figure 6.2(e)).

At relatively high 0.55 SaO$_2$, the distinct double peaks of the absorbance curve associated with oxyhemoglobin can be seen in Figure 6.2(k). This is different from the absorbance curve in Figure 6.2(l) where absorbance is mainly due to deoxyhemoglobin. Good agreement between experimental data and fitted curves are observed over the spectral range despite the simplicity of the diffuse reflectance model. Generally, R^2 values of the fits are greater than 0.85 over the extent of the MWC.
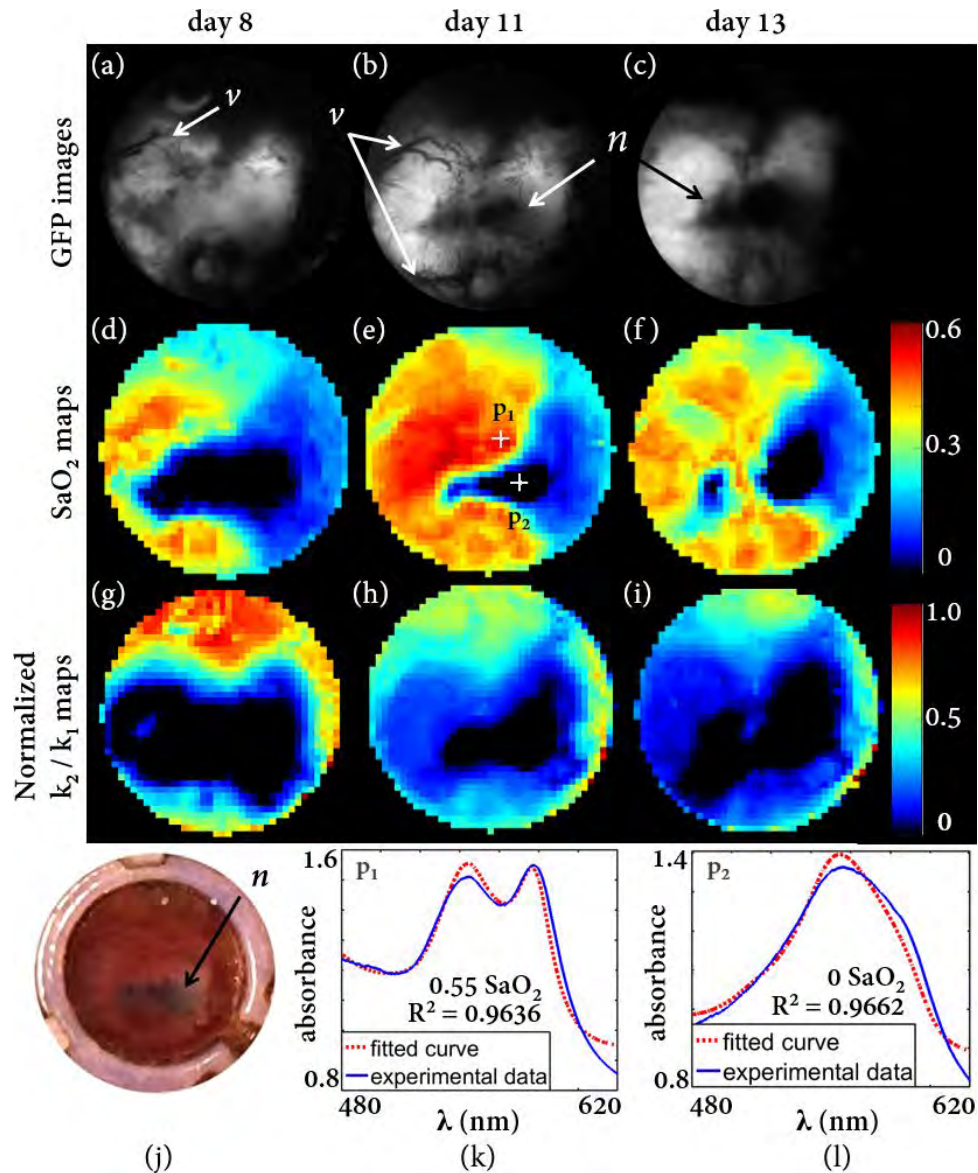
Figure 6.2: Hyperspectral reflectance imaging to measure SaO_2 in the MWC model. (a)-(c) are GFP images at days 8, 11, and 13 after cell inoculation. Aberrant vasculature and necrosis are marked as "v" and "n", respectively. (d)-(f) SaO_2 maps of the MWC at corresponding days. (g)-(i) Normalized maps of k_2/k_1 coefficient (see Equation 6.7), which are related to fat content. (j) A picture of the MWC taken at day 11 which shows the marked necrotic region being darker than surrounding tissue. (k) and (l) show plots of measured and fitted absorbance curves at two different locations marked p_1 and p_2, respectively.

6.4   Dynamic monitoring of SaO_2 during breathing gas modulation

The previous section illustrates the use of the spectral imaging system to monitor the change in tissue oxygenation as the vasculature around a tumor evolved over a two week time period. In this section, an experiment was performed to dynamically monitor the variation in tissue oxygenation that occurs within minutes.

The amount of dissolved oxygen in the bloodstream is directly correlated with the partial pressure of oxygen in the lungs. pO_2 is a parameter that quantifies the partial pressure excerted by free dissolved oxygen molecules in the blood plasma. Generally, the higher the pO_2, the easier it is to chemically bond with hemoglobin and, thus, the higher is the SaO_2 . Therefore, to produce a change in blood oxygen level in a mouse, the oxygen content of the gas provided to the mouse during the experiment was modulated between setting #1 and #2 as described in Table 6.1. The animal being imaged in this experiment was a female SCID mouse with a MCF-7/GFP breast cancer tumor at day 8 after cell innoculation.

Table 6.1: Settings used to modulate oxygen content in inspired gas

Setting	Inspired gas
#1	1 L/min pure O_2 and 1.5% isofluorane
#2	1 L/min air with 20% O_2 and 1.5% isofluorane

At the start of the experiment, gas settings #1 was used, in which pure oxygen flowing at 1L/min was given to the animal. This was similar to what would typically be used in an imaging experiment for MWC animals. Spectral imaging commenced after the animal's body temperature and respiration rate was stable. After acquiring three consecutive data sets at these settings, the gas was switched to setting #2, in which the oxygen content dropped from approximately 100% to 20%. Four consecutive imaging data sets were acquired at this setting. After completion, gas flow was returned to settings #1 and another four data sets were acquired. All imaging data were completed in under 25 minutes. Care was taken to maintain the body temperature and respiration rate at 34 ± 0.1^oC and approximately 65 breaths min^{-1}, respectively, as these two parameters could potentially influence the blood

oxygenation of the animal.

A GFP image of the tumor in the MWC is shown in Figure 6.3(a). It was a tumor that covered more than half of the area of the MWC. Non-uniform strength of the GFP signal was observed across the tumor. However, the GFP image indicated that the tumor was well vascularized in general. The SaO_2 maps for each imaging time point are shown in Figures 6.3(b)-(l).
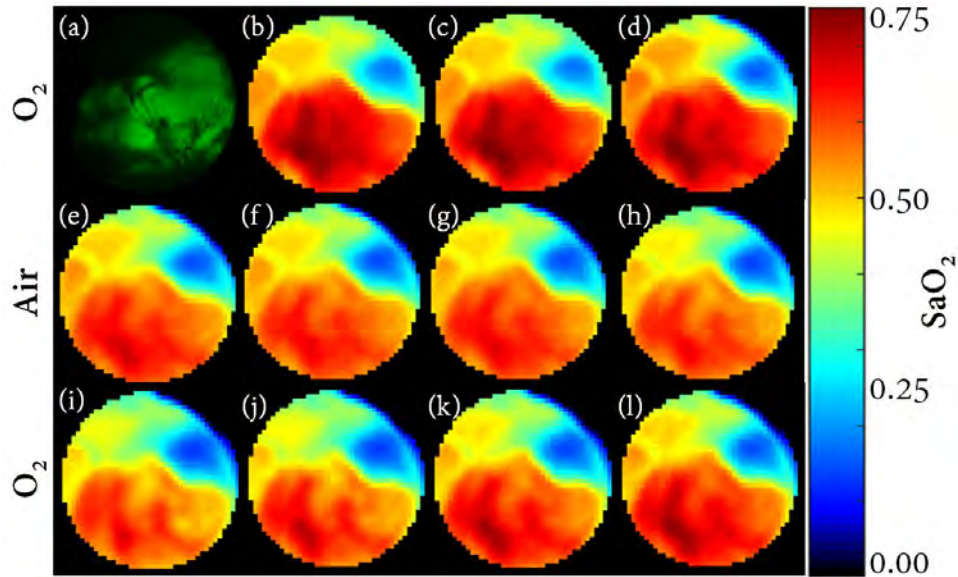
Figure 6.3: Modulation of tissue oxygenation by changing oxygen content in inspired gases. (a) GFP image of the MWC. (b)-(l) SaO_2 maps of MWC at different time points. SaO_2 maps in first and last rows were obtained when high oxygen gas setting #1 was used, while SaO_2 maps in the middle row were obtained when low oxygen gas setting #2 was used.

A map of baseline SaO_2 values, shown in Figure 6.4(a), was obtained by computing the average of the first three measurements taken when gas settings #1 was used. Representative plots of the variation of SaO_2 at two locations, marked p_1 and p_2 in Figure 6.4(a) are shown in Figures 6.4(b) and (c), respectively. p_1 is in a region where there was a relatively high baseline SaO_2, while p_2 is in the relatively hypoxic region in the upper right.
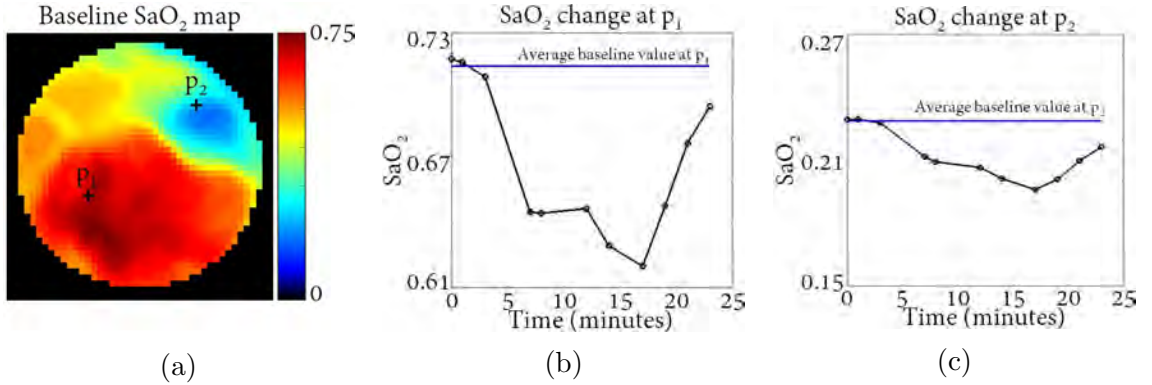
Figure 6.4: Change in SaO$_2$ in the MWC. (a) Map of baseline SaO$_2$ based on the average of the first three measurements taken during the use of gas setting #1. (b) and (c) show the temporal change in SaO$_2$ at locations p$_1$ and p$_2$ (as marked on SaO$_2$ map), respectively.

To further analyze the oxygen modulation effects, maps of the following parameters were computed and are shown in Figures 6.5(a)-(c).

$$\text{Max. decrease in SaO}_2 = Y_{min} - Y_b \tag{6.9}$$

$$\text{Max. percent change in SaO}_2 = \left(\frac{Y_{min} - Y_b}{Y_b} \right) \times 100\% \tag{6.10}$$

$$\text{Percent recovery in SaO}_2 = \left(\frac{Y_{final}}{Y_b} \right) \times 100\%, \tag{6.11}$$

where Y_b, Y_{min}, and Y_{final} are the baseline SaO$_2$, the minimum SaO$_2$ during the entire course of the experiment, and the SaO$_2$ value at the last imaging time point, repsectively.
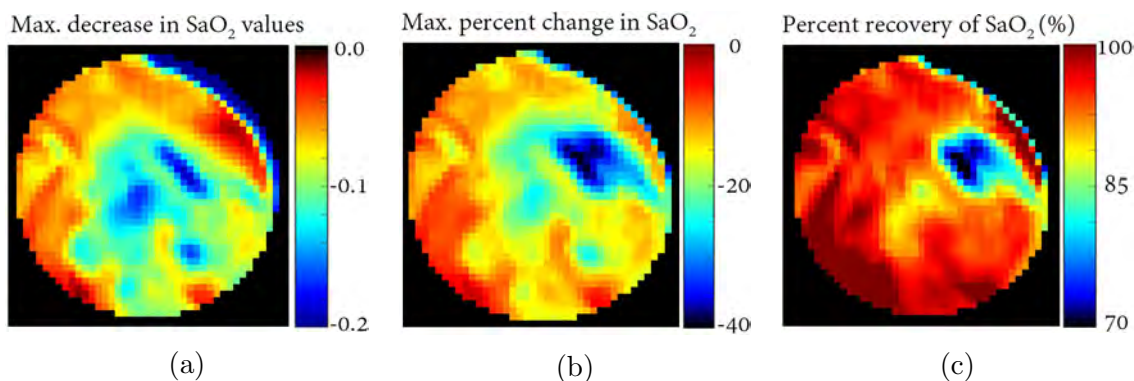
Figure 6.5: Monitoring effects of oxygen modulation on SaO_2 of MWC. Maps of (a) maximum decrease in SaO_2 values in MWC, (b) maximum percent change in SaO_2 with respect to baseline values and (c) percent recovery of SaO_2 values at the last imaging time point.

Comparing the images shown in Figures 6.5 with the baseline SaO_2 map shown in Figure 6.4(a), it is observed that the hypoxic tumor region is most susceptible to the oxygen modulation and suffered the most percent drop in SaO_2 when the mouse was inspiring 20% O_2 air. In addition, the hypoxic region was least capable of returning to baseline SaO_2 levels when the gas setting was returned to flowing pure O_2. In contrast, the majority of the other regions were able to achieve at least 90% of the baseline SaO_2 values within 6 minutes.

From the GFP image of the MWC (Figure 6.3), it is evident that the hypoxic area corresponds to a region in the tumor where there is a lack of vascular network. It is common for fast-growing tumors to experience hypoxia, especially in tissue that is at a distance far from the blood supply. Compromised and irregular neo-vasculature within the tumor give rise to inefficient dissemination of oxygen through the bloodstream. Tissue that is ill supported by the vasculature, such as in the hypoxic tumor region, then has to rely on the slow diffusion of oxygen through interstitial spaces in the tissue. It is hypothesized that the lack of efficient vascular network around the hypoxic region is one of the main causes of the higher severity of drop in tissue oxygenation and slower recovery rate. Tumor tissues, that have high demand for oxygen and are distant from the vascular network, would have a smaller reserve of available oxygen. A constant supply of diffused oxygen is necessary to

keep SaO_2 at baseline values. A decrease in oxygen in the bloodstream will decrease the oxygen diffusion distance and essentially cut the supply to distant tissue. As a result, these tissues will be more impacted by the oxygen gas modulation. Similarly, it will take a longer period for the tissue to re-equilibriate as the diffusion process will take a longer period to reach more distant tissue.

6.5   Investigating significance of GFP excitation with broadband illumination

Figure 6.6(a) shows the normalized spectral sensitivity of the system consisting of a combination of the spectrum of the broadband light source, the spectral transmission of the optical system, and the detector's wavelength-dependent quantum efficiency. This data was obtained by reflecting the light source off a 99% reflectance Spectralon standard in a configuration similar to what was used for the MWC experiments. Figure 6.6(b) shows the normalized excitation and emission spectra of GFP (data from Thermo Fisher Scientific). GFP has excitation and emission peaks at 489nm and 508nm, respectively. Comparing Figures 6.6(a) and (b), it is observed that the broadband light source contains energy in the GFP's excitation wavelength range. This section describes an experiment that was carried out to investigate whether the resultant GFP excitation due to the lamp's spectrum is significant and if it should be considered in the modelling of the measured absorbance curve (Equation 6.7) when GFP-transduced tumor tissue are being imaged.
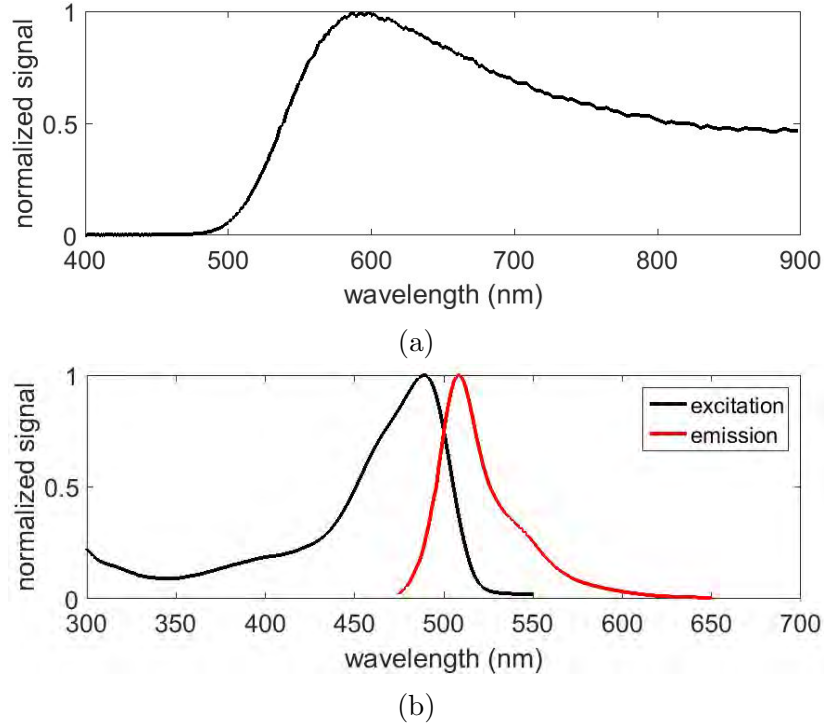
Figure 6.6: (a) Normalized spectrum of the light source used for spectral imaging of MWC. (b) Excitation and emission curves of GFP.

Spectral imaging of a MWC with an implanted MDA-MB-231/GFP tumor xenograft was carried out with the full spectrum of the light source. After completion of this data acquisition, a 520nm longpass filter (LPF) was inserted in front of the light source to block most of the GFP excitation wavelength and a second set of spectral imaging experiments was carried out on the same animal. Similarly, two spectral measurements of the 99% reflectance Spectralon were done with the full and filtered light source. This enabled computation of the absorbance maps of the MWC under the two different illumination conditions (with and without GFP excitation). Representative absorbance curves at a location at the center of the MWC are shown in Figure 6.7. A comparison of the two curves shows that there is excellent agreement between them over the spectral range from 520-800nm. There are small differences in the absorbance curves at wavelengths above 800nm but this is probably due to slight variation in the transmission of the 520 LPF. From this result, it is concluded that the GFP fluorescence being excited by the broadband

light source is small and does not affect the absorbance measurements that were used to derive SaO_2 maps in the MWC.
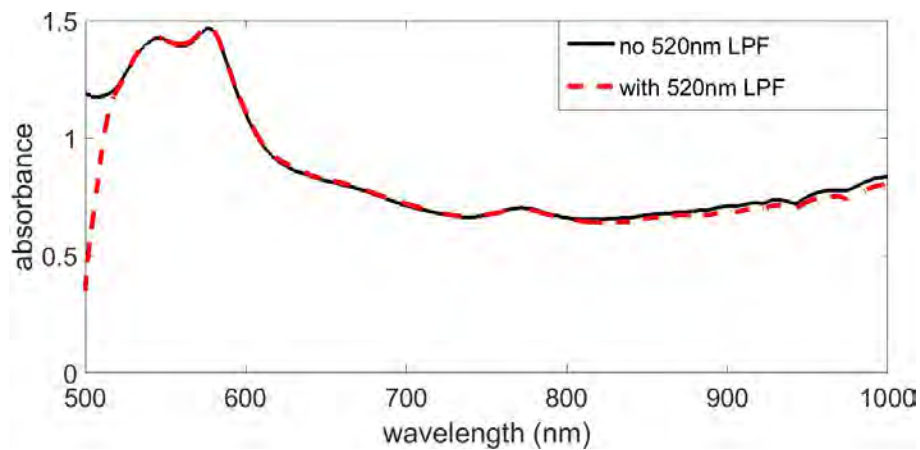
Figure 6.7: Two representative absorbance curves of the center of a MWC as measured with the full spectrum of the lamp (black solid line) and with a 520nm LPF light (red dashed line).

CHAPTER 7

Oxygenation as an Early Biomarker of Response to Neoadjuvant Chemotherapy

7.1   Background and motivation

Having established the capabilities of the spectral imaging system, this chapter discusses an application for which the system can be used to better understand the biological mechanisms behind early response to neoadjuvant chemotherapy (NAC) for breast cancer patients.

NAC, or preoperative chemotherapy, has become a standard treatment offered to breast cancer patients with the main purpose of either downstaging unresectable tumors to operable sizes or improving surgical outcomes in terms of breast conservation and cosmesis. A standard NAC regimen consists of multiple cycles of chemotherapy that are administered over a few months [90] before changes in tumor volume can be used to determine treatment response and endpoints of NAC. During the course of treatment, patients may suffer from acute or delayed adverse effects. The side effects, which include ulcerations, gastrointestinal perforation, cardiac dysfunction, and thromboembolic complications [91, 92] adversely impact patients' quality of life. Therefore, it is imperative to evaluate tumor response to treatment early in the treatment regimen to avoid exposing non-responders to unnecessary drug toxicity and to facilitate optimization of treatment strategies for each individual.

Chemotherapy often involves targeting adaptive molecular pathways of tumor cells, thereby leading to downstream effects such as changes in perfusion, metabolic rate, and/or oxygen utilization in the malignant tissue. Changes in these surrogate biomarkers could precede tumor volume changes [93, 94] and, therefore, could be useful in predicting treatment response early in the treatment regimen. Recently, there has been evidence that measurements of oxyhemoglobin levels might be a promising biomarker that can be used to delineate responders from non-responders

24 hours after the first cycle of NAC [95]. Patients that ultimately showed partial or complete response exhibited a temporary spike in oxyhemoglobin levels, while such change was absent in non-responders. Despite the important clinical implications of this finding, the biological mechanism behind such a phenomenon has yet to be determined.

The use of the orthotopic mouse MWC model is especially well suited for multi-modal *in vivo* studies of breast cancer xenografts that can be used to investigate the abovementioned phenomenon. Being an orthotopic model, the breast cancer tumor cells are implanted in the native site of breast cancers. Therefore, this model better mimics the biology of breast cancers than ectopic animal models. Both high-resolution optical imaging and magnetic resonance imaging (MRI) techniques are compatible with this MWC model and they can be used to investigate dynamic spatiotemporal changes of breast cancer xenografts in vivo. Such capabilities are critical in investigating a range of possible biological changes that take place post-chemotherapy and possibly provide clues on how to improve response to chemotherapy.

In this chapter, the spectral imaging methods described in Chapter 6 were used in a pilot study with a small group of animals to evaluate if response to NAC in MWC mice was accompanied by similar trends in blood oxygenation that were observed in human subjects. Imaging tools to study various factors that might possibly explain oxygenation changes after receiving NAC were also developed and are discussed separately in later chapters.

7.2   Oxygen dissociation curve

The imaging system and data processing methods used in this work yield information about SaO_2. It is important to tie the discussion with a closely related parameter, pO_2, which is the partial pressure excerted by free oxygen molecules in the blood plasma.

The amount of free oxygen, and bound oxygen attached to hemoglobin, are

governed by the oxygen dissociation curve, as shown in Figure 7.1 (reproduced from [96]). Oxygen molecules that are bound to hemoglobin do not impinge on oxygen electrodes and do not contribute to the measurement of pO_2. Generally, the higher the pO_2, the higher is the SaO_2.

Figure 7.1 also illustrates that the oxygen dissociation curve shifts according to factors affecting allosteric regulation of oxygen affinity to hemoglobin. Lower body temperature and higher pH are two common factors that shift the oxygen dissociation curve to the left. Higher temperature or increased acidity cause a shift to the right. The latter is also known as the Bohr effect. Assuming similar pO_2 values, tissue with lower temperature and higher pH will experience higher SaO_2. Understanding how physiological parameters modify the oxygen dissociation curve is important in the understanding of variations in measured SaO_2 values. Furthermore, maintaining respiration rate and body temperature during experiments is important to help eliminate factors that can undermine the detection of drug-induced changes in SaO_2.
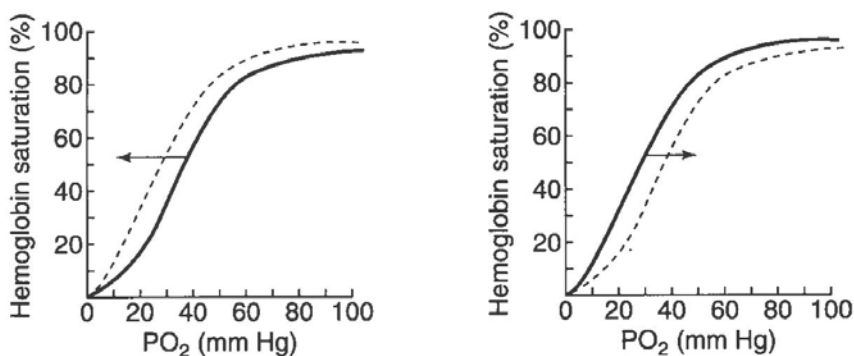
Figure 7.1: Oxygen dissociation curves. Lower temperature and reduced acidity can cause the dissociation curve to shift left (left graph). Higher temperature or increased acidity cause a shift to the right (right graph).

7.3 Possible explanations for drug-induced changes in tissue oxygenation

The main motivation behind the work described in this chapter comes from a clinical study [95] that reported a temporary spike in oxygenation observed in both partial

and pathologic complete responders, independent of the type of chemotherapy regimen they received. More importantly, the increase in oxygenation occurred very rapidly (24 hours) after the initial round of NAC.

The two main factors that govern the demand and supply of oxygen in tissue cells are the rate of utilization of oxygen by tissue cells and the blood perfusion rate. Changes in one or both will lead to a change in tissue pO_2 and SaO_2. With reference to the discussion in Section 3.1, there are two metabolic pathways that cells can undergo, namely oxidative phosphorylation and glycolysis. Cells typically undergo a mix of both metabolic pathways, although the percent dependence on each pathway is dependent on the status of the cells. Therefore, both the metabolic rate and the type of metabolic pathway are important factors in determining the rate of utilization, and hence, extraction of oxygen from blood. On the other hand, blood perfusion affects the steady-state delivery of blood to tissues through the capillary bed. Upstream factors that could lead to blood perfusion changes include differences in blood flow rate, density of red blood cell (RBC) in the blood stream, density of capillaries, vascular abnormalities, and vasodilation/constriction. An imbalance between demand and supply of oxygen to tissue cells would tip the scale on oxygen saturation one way or the other.

In contrast, any factors that modify the oxygen dissociation curve would result in a change in measured SaO_2, even if there is neither a change in metabolism nor blood perfusion. Apart from the pH and temperature changes mentioned earlier, an increased concentration of other dissolved gases in the blood, such as carbon monoxide, could lead to a lower SaO_2. Under such circumstances, the heme groups on a hemoglobin would be occupied by those molecules. If oxygen is incapable of replacing them due to lower affinity, the oxygen-load on hemoglobin would be decreased. Another factor that can lead to a shift in the oxygen dissociation curve to the left is an elevated concentration of methemoglobin (metHb). In metHb, one or more of the heme groups in the hemoglobin contains a ferric (i.e. Fe^{3+}) instead of a ferrous (Fe^{2+}) center. This results in a higher affinity between oxygen and metHb, making it more difficult for oxygen to be released to tissue cells. This is inspite of

a higher resulting SaO_2 value, which is otherwise associated with increased tissue oxygenation. Certain chemotherapy drugs, such as doxorubicin (DOX), induces an increase in the amount of nitric oxide (NO) [97] in cancer cells. Since it is known that high amounts of NO leads to elevated concentrations of metHb [98], it is possible that chemotherapy can affect SaO_2 .

In this dissertation, multimodal imaging tools were developed to specifically study glycolytic metabolism, blood perfusion, and oxygen saturation in the MWC. How these imaging modalities can be used to investigate possible mechanisms driving drug-induced SaO_2 changes are summarised in Table 7.1. It should be emphasized that Table 7.1 represents the causality of various effects only if each of them is considered independently while other metrics stay unchanged. In reality, different factors might arise simultaneously, and could either negate or amplify their effects on resultant SaO_2.

Table 7.1: Biological changes and their effects on images, if considered independently

Biological changes	SaO$_2$	Effects on oxygenation	Effects on other imaging signals
Overall decreased metabolic rate	Increase	Decreased demand for both O$_2$ and glucose	Weaker signals in nuclear images
Metabolic switch to glycolysis	Increase	Decreased demand for O$_2$ but higher demand for glucose	Stronger nuclear signals
Increased blood flow rate	Increase	Higher rate of supply of O$_2$	Higher perfusion as measured by MRI
Increased blood pressure	Increase	Higher rate of supply of O$_2$	Higher perfusion as measured by MRI
Increased production of RBC	Uncertain	Higher rate of supply of O$_2$	No change in perfusion as measured by MRI
Increased density of capillaries	Increase	Higher rate of supply of O$_2$	Higher perfusion as measured by MRI
Vasodilation	Increase	Higher rate of supply of O$_2$	Higher perfusion as measured by MRI
Lower pH	Decrease	Higher rate of supply of O$_2$	High acidity measured by optical pH imaging
Increased metHb	Decrease	Lower rate of supply of O$_2$	Unknown
Increased dissolved gases in blood, other than O$_2$	Decrease	Lower rate of supply of O$_2$	Unknown

7.4 Methodology and experimental protocols

The experimental protocol illustrated in Figure 7.2 was developed to investigate the potential of using the spectral imaging system to monitor changes in tumor SaO$_2$ in the early stages of treatment. Initially, either MDA-MB-231/GFP or MCF-7/GFP breast cancer cells were orthotopically injected into the left fourth mammary fat pad of female SCID mice. The cells were allowed to grow into solid tumors

before MWCs were surgically implanted. Next, baseline SaO_2 maps were obtained by spectral imaging. Shortly after, treated animals were given an IV injection of 3mg/kg DOX while control animals receive an IV injection of the same volume of vehicle (saline). Multiple spectral imaging experiments were carried out during the first three days after treatment to monitor SaO_2 changes in the MWC. MRI of tumor volume was performed periodically to measure tumor growth rates. In the event that the structural integrity of the MWC was compromised, it was surgically removed from the animal and metallic surgical clips were used to close the wound. Evaluation of tumor growth continued after the surgical clips were removed. Treated animals that exhibited a delayed or slower tumor growth rate as compared to untreated control animals, were categorized as responders.

Based on the differences in their immunoprofiles, breast cancer cell lines can be broadly classified into several sub-types. Classification originally include lumina A, lumina B, basal, and HER2. However, recent studies indicate the existence of another sub-type, known as Claudin-low. MDA-MB-231 cells are known as triple negative cells because they are characterized by the lack of expression of estrogen receptors (ER), human epidermal growth factor receptors (HER2), and progesterone receptors (PR). Due to such a immunoprofile, MDA-MB-231 cells were orginally classified as basal phenotypes. However, more recently, they are identified as a Claudin-low subtype. Unlike MDA-MB-231, MCF-7 cells are ER-positive and they belong to the lumina A sub-type. Because they over-express estrogen receptors, slow release estrogen pellets were implanted in the animals before the injection of MCF-7 cells to stimulate tumor growth. Both MDA-MB-231 and MCF-7 cells are known to be responsive to chemotherapy [99].
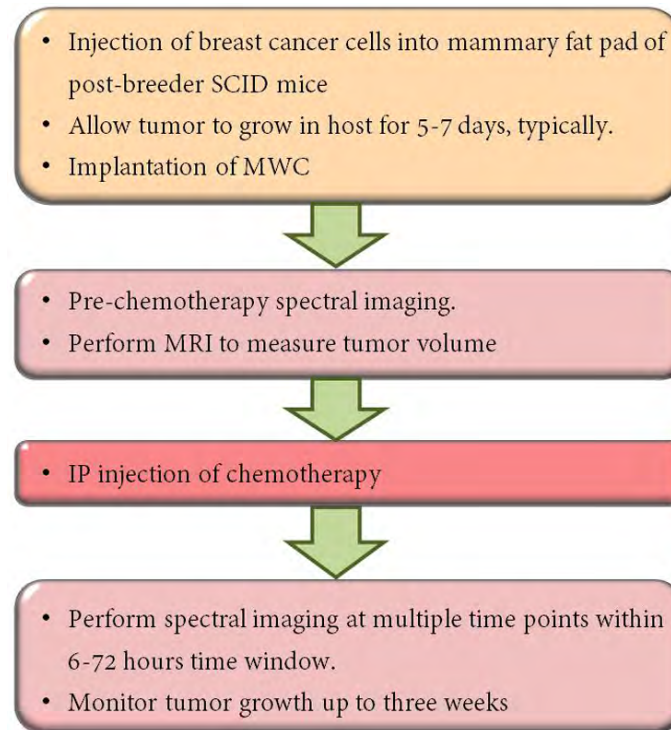
Figure 7.2: Experiment protocols to investigate oxygen saturation changes and response to treatment.

7.5 Experimental results

7.5.1 Imaging SaO_2 of MDA-MB-231 tumors

This section starts with the presentation of experimental results obtained with MDA-MB-231 tumor xenografts. SaO_2 maps of a treated and untreated animal are shown in Figures 7.3(a) and (b). A graph of the percent change in tumor volume is shown in Figure 7.3(c). There was limited data on the growth rate of the untreated animal as the animal was sacrificed prematurely due to a compromised MWC. The imaging time points referred to in the figures are with respect to the time point when the animal received chemotherapy, although the control animal received a vehicle-only injection.

(a)

(b)

(c)
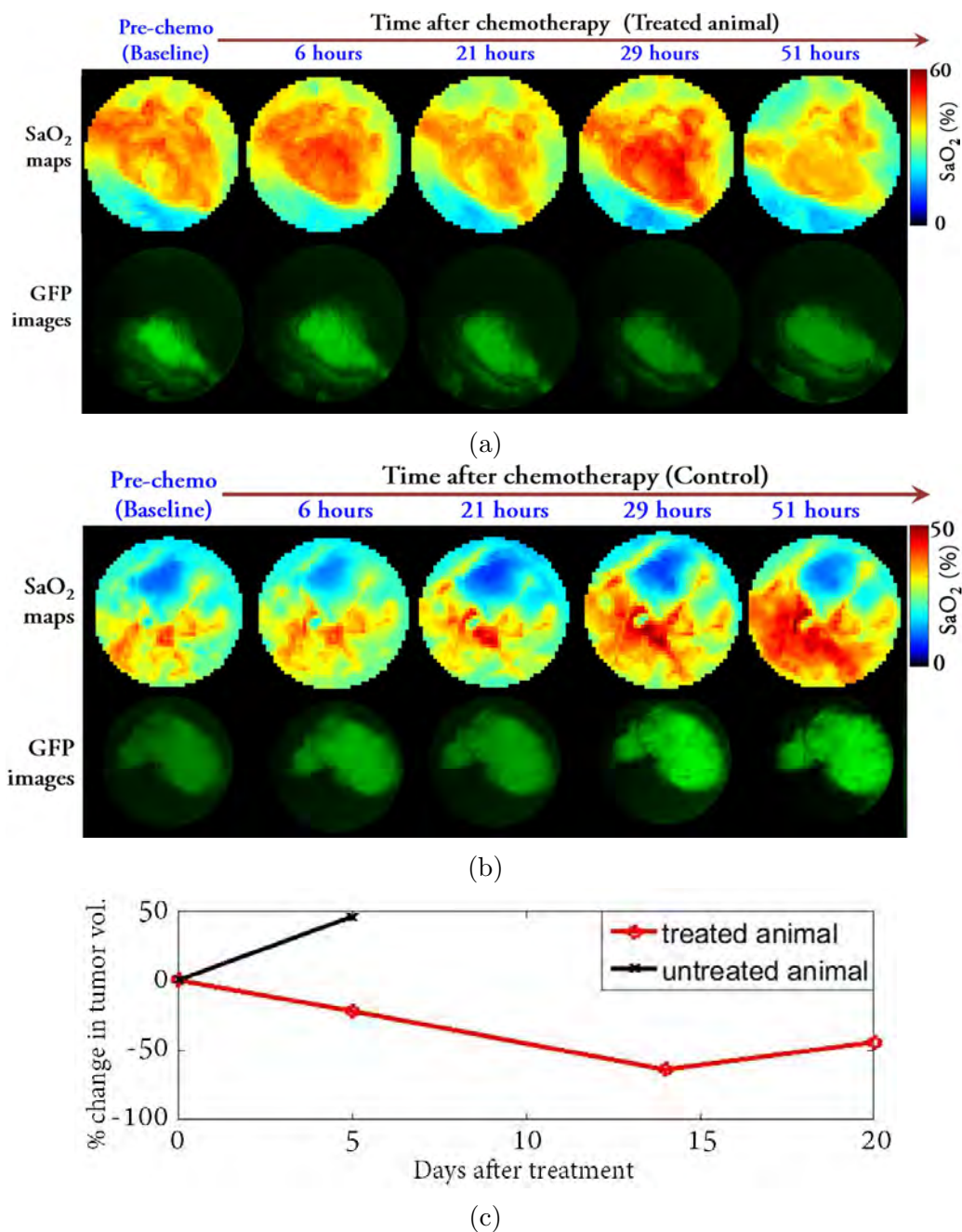
Figure 7.3: SaO$_2$ maps of a (a) treated and an (b) untreated animal. (c) Graph of percentage change in tumor volume, compared to baseline values. The imaging time points referred to in the figures are with respect to the time point when the animal received the chemotherapy, although the control animal received a vehicle-only injection.

The SaO_2 maps were used to perform ROI analysis of the mean SaO_2 values of the MWC. Tumor (T) and surrounding tissue (S) ROIs were selected based on co-registered GFP images of the MWC taken at each imaging time point. The mean and standard deviation of the SaO_2 values within the ROIs were computed and are presented as a bar graph in Figure 7.4(a). The percentage change of the mean SaO_2 values within the ROIs was computed and is plotted in Figure 7.4(b).

It was observed from Figures 7.3(a) and (b) that the changes in the GFP images of both animals were gradual and minimal. On the other hand, there were significant changes in the SaO_2 maps over time. Firstly, looking at the imaging results of the treated animal, the mean baseline SaO_2 of the tumor was 0.406. The regions of comparatively high SaO_2 corresponded to areas with visible vasculature on the GFP image. The region of high SaO_2 extended beyond the visible GFP tumor towards the top half of the MWC. After receiving an IV injection of 3 mg/kg of DOX, the MWC was imaged at multiple time points corresponding to 6, 21, 29, and 51 hours after treatment. The mean SaO_2 values in the tumor first increased by 10.6% before dropping to near baseline values. It then subsequently increased by 18.9% and eventually fell to near baseline values again. The cyclic nature of the variation in SaO_2 values were not observed in the surround tissue of the same animal. Instead, the mean SaO_2 values in that ROI were consistently below baseline values. MRI of the tumor over 20 days following treatment revealed that the tumor decreased in volume, reaching it's minimum at about two weeks after treatment. Subsequently, there was a small increase in size a week later. Based on the tumor volume measurements alone, it was likely that there was a certain degree of response to chemotherapy in the animal.

In contrast to the treated animal, it was observed that more than half of the tumor of the control animal had a baseline SaO_2 lower than 0.25, which was considered hypoxic. Six hours after receiving a vehicle-only injection, the mean tumor SaO_2 increased slightly from 0.233 to 0.254. However, the mean tumor SaO_2 subsequently plunged to 0.097 and the SaO_2 remained below 0.13 until the last imaging time point. Although the tumor became increasingly hypoxic, the opposite was

(a)

(b)
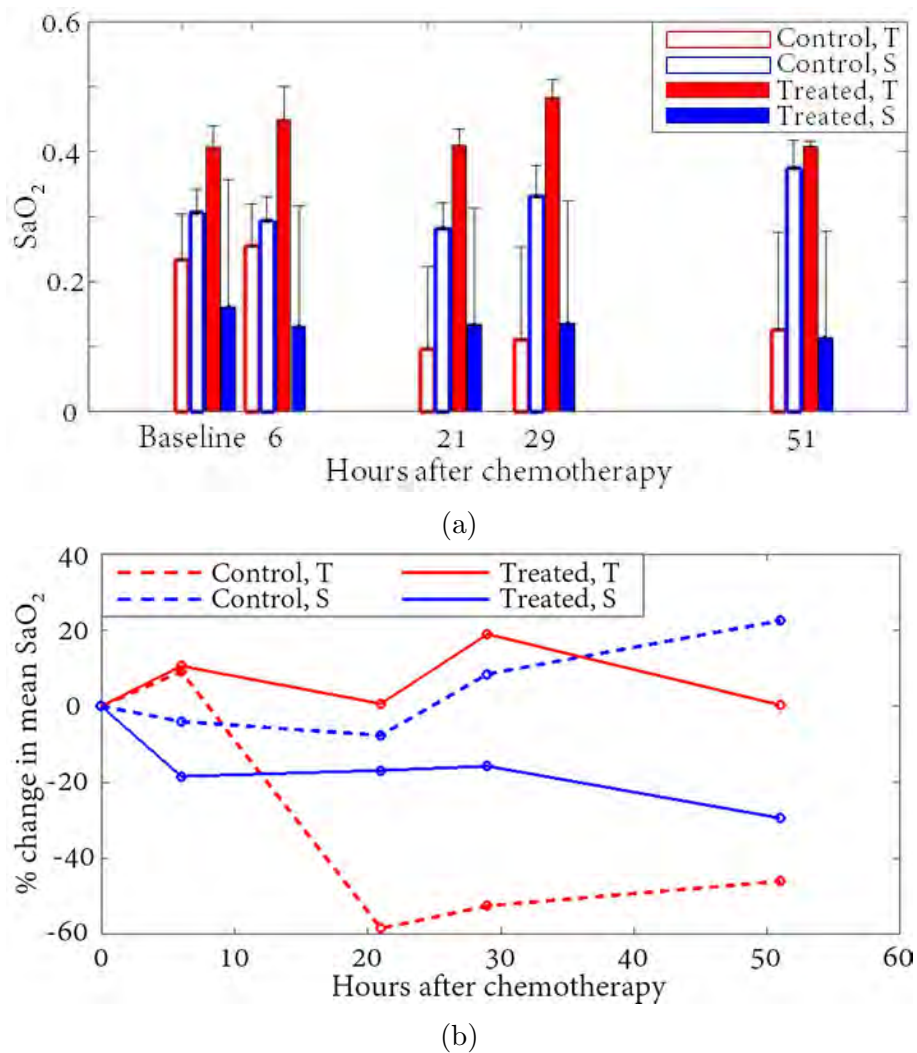
Figure 7.4: Analysis of SaO_2 changes of MDA-MB-231 xenografts. (a) A bar diagram showing the mean SaO_2 values of tumor (T) and surrounding tissue (S) before and after treatment. Error bar indicate a standard deviation of the SaO_2 values within each ROI. (b) A plot showing the percent change of mean SaO_2 values within the tumor and surrounding tissue before and after treatment.

true for the surrounding tissue. The mean SaO_2 of the surrounding tissue ROI increased from a baseline value of 0.305 to 0.374 at the final imaging time point. The SaO_2 maps also reveal that the extent of the MWC that had greater than 0.4 SaO_2 expanded over time. Notably, the well-oxygenated area extended into part of the tumor that was at the top-left quarter of the MWC. Although there was limited data on the longer term growth rates, there was an approximately 50% increase in tumor volume in the control animal 5 days after baseline measurements. This is in contrast to the gradual decrease in tumor volume in the treated animal.

7.5.2 Imaging SaO_2 of MCF-7 tumors

This subsection shows the results for four MCF-7 tumor xenografts, which include two controls and two animals treated with 3mg/kg of DOX. Baseline SaO_2 measurements were obtained shortly before treatment and multiple SaO_2 measurements were taken at multiple time points between 6 and 75 hours after injections. Images of the SaO_2 maps and corresponding GFP images are shown in Figures 7.5(a)-(d). As compared to MDA-MB-231 xenografts, tumors from the MCF-7 cell line appear to have a more heterogeneous structure. For instance, the GFP images in 7.5(a) showed that the tumor had two distinct parts to it, one with a much weaker fluorescence than the other. Although heterogeneity was also observed in the GFP images for the other three animals, the heterogeneity was less remarkable.
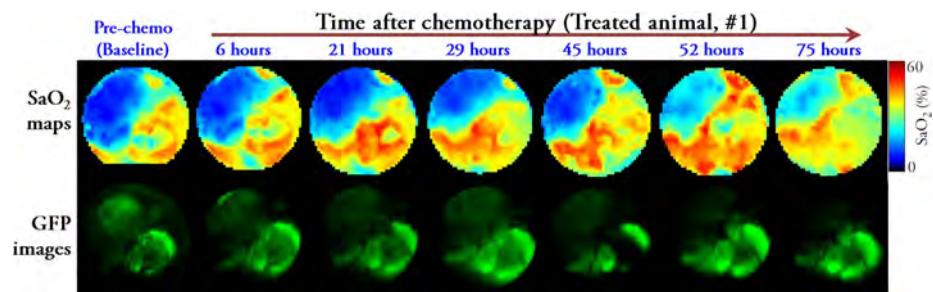
(a)
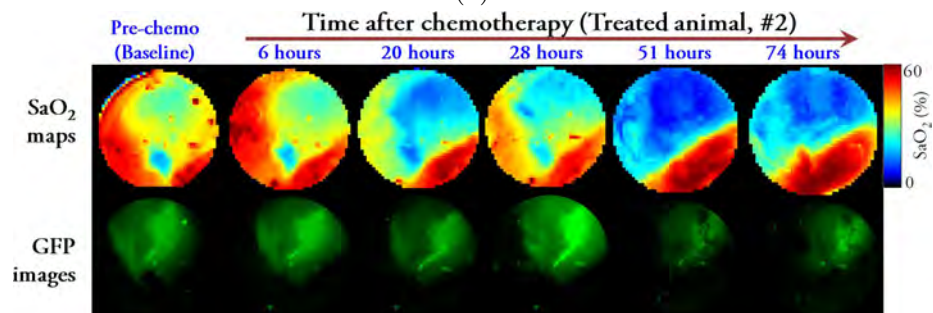
(b)
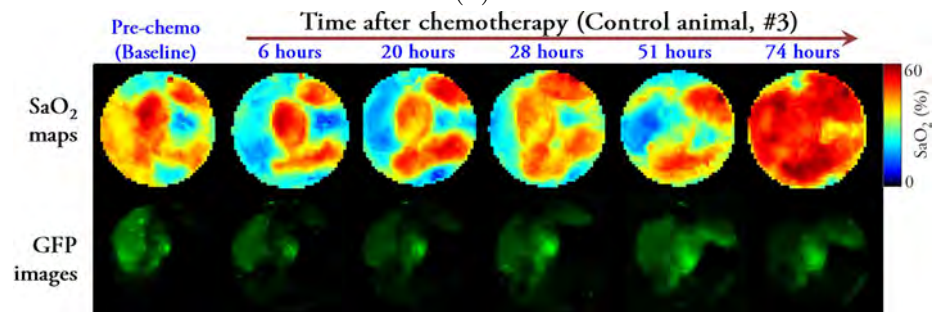
(c)
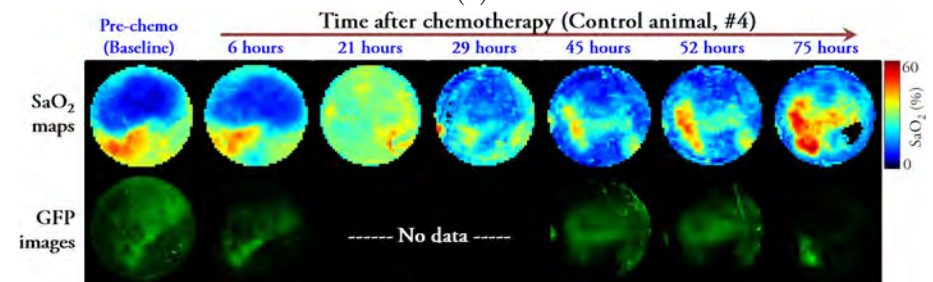
(d)

Figure 7.5: SaO$_2$ maps of MCF-7 xenografts before and after treatment. (a) and (b) are SaO$_2$ maps of treated animals while (c) and (d) are those of control animals. Due to presence of bleeding in the MWC that obscured GFP signals, 2 GFP images in set (d) were not available.

In Figure 7.5(d), there are no GFP images at the 21 and 29 hour imaging time points and this was due to the presence of bleeding in the MWC of animal #4. The injury was a result of an attempt to replace a cracked glass coverslip of the MWC. As a consequence, the blood obscured the fluorescence of the GFP tumor. Although the bleeding cleared within 40 hours, the SaO_2 measurements of the underlying tissue were compromised. Therefore, this animal was excluded from furthur analysis.

In addition, the tumor in one of the treated animals (animal #1, Figure 7.5(a)) had two distinct lobes and they were analyzed individually. Because the tumor covered most of the MWC and there was not much surrounding tissue in the clear FOV, the analysis of that animal was restricted to the two tumor ROIs. For animals #2 and #3, tumor (T) and surrounding tissue (S) ROI analyses were carried out on each of them.

Bar diagrams of the mean tumor and surround tissue ROIs of the animals are shown in Figures 7.6(a) and 7.6(b), respectively. Standard deviation of the SaO_2 values within the ROIs are indicated on the bar diagrams. The percentage change in mean SaO_2 of different ROIs is plotted in Figure 7.6(c). Lastly, the tumor growth rates of the four animals are shown in Figure 7.7.
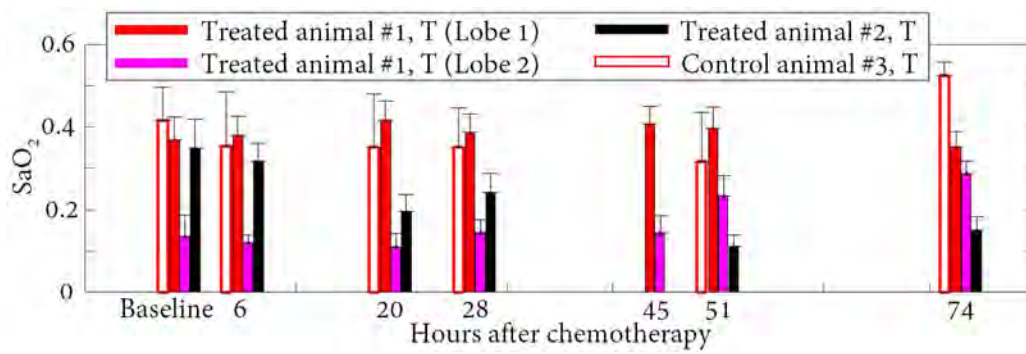
(a)
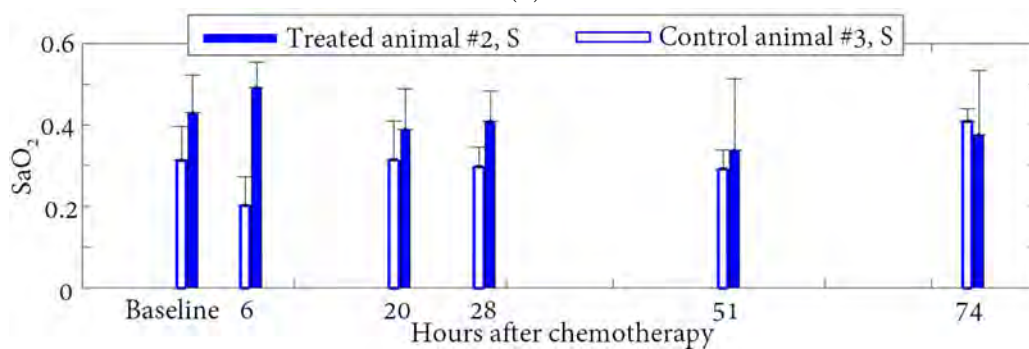
(b)
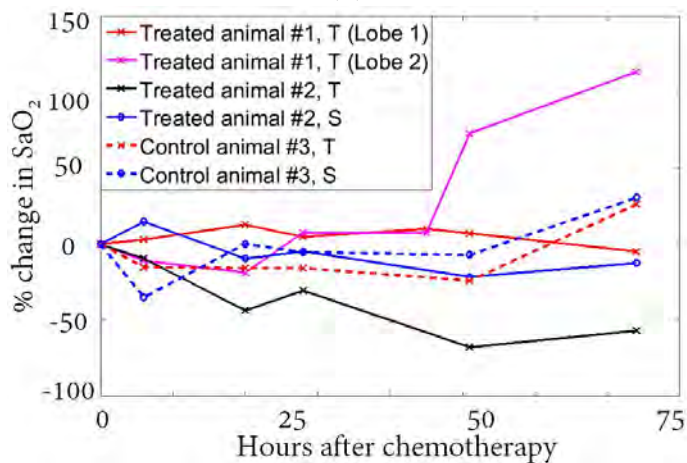
(c)

Figure 7.6: Analysis of SaO_2 changes of MCF-7 xenografts. (a) A bar diagram showing the mean SaO_2 values of tumor (T) before and after treatment. (b) A bar diagram showing the mean SaO_2 values of normal surrounding tissue (S) before and after treatment. Error bar indicate a standard deviation of the SaO_2 values within each ROI. (b) A plot showing the percent change of mean SaO_2 values within the tumor and surrounding tissue before and after treatment.
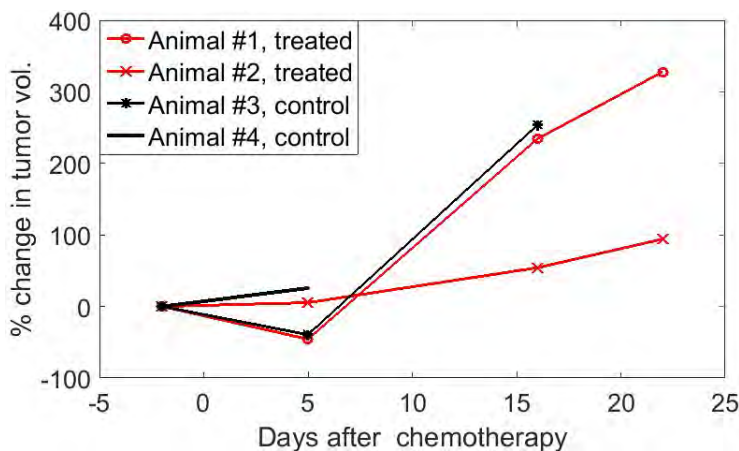
Figure 7.7: MCF-7 tumor volume measurements at multiple time points before and after treatment (3mg/kg DOX).

The discussion here starts with the analysis of the treated animal #1 with two distinct tumor lobes (Figure 7.5(a)). The region on the lower right quarter of the MWC with significantly stronger GFP signal will be referred to as lobe 1, while the part on the top left quarter of the MWC is referred to as lobe 2. Tumor lobe 1 had a mean baseline value of 0.369. Although there was less than a 13% change in mean SaO_2 over the 75 hours monitoring period, the SaO_2 maps showed that the area with greater than baseline SaO_2 expanded over time. An exception was the last image when the mean SaO_2 dropped to approximately baseline value and the previously high SaO_2 region at the bottom portion of the tumor became less oxygenated.

Tumor lobe 2 of the same animal had visibly weaker GFP signals than lobe 1 and it's fluorescence got progressively weaker. This tumor region was hypoxic and it had a low mean baseline SaO_2 of 0.135. After receiving chemotherapy, hypoxia persisted in this region and mean SaO_2 values remained lower than 0.15 up until 45 hours after treatment. After that, the mean SaO_2 of the region increased and reached 0.288 at 74 hours after treatment. At this time, the GFP in the ROI had disappeared almost completely. The difference in SaO_2 between the two ROIs became smaller and this was reflected in the last SaO_2 map for the animal, which showed a relatively more uniform SaO_2 across the chamber. Likewise, the mean SaO_2 values of the two ROIs at the 74-hour time point shown in Figure 7.6(a) were more similar than before

treatment. MRI results showed that the tumor had a relatively modest decrease in volume 5 days after treatment. However, it grew rapidly from then on and within 22 days, it reached a size more than 3 times as large as before treatment. Since the growth rate was similar to that of the control animal #3, it is likely that this animal did not respond to chemotherapy.

Next, looking at the SaO_2 maps of treated animal #2, it is shown that the tumor started out being less oxygenated ($SaO_2 = 0.349$) than surrounding tissue ($SaO_2 = 0.429$). The difference in the SaO_2 values between tumor and the surrounding tissue became increasingly larger over time. The difference in SaO_2 was most prominently illustrated in the SaO_2 map obtained 51 hours after treatment when most of the tumor had SaO_2 below 0.2 while that of the surround tissue was close to 0.6. Although the area of the GFP in the MWC seemed to have decreased slightly over time, MRI showed that there was in fact a slow tumor growth. Since the growth was slower than that of the control animal #3, it is possible that this animal did respond to chemotherapy.

Animal #3 was a control that did not receive chemotherapy. From its GFP images and MRI tumor volume measurements, it was clear that the tumor was rapidly growing. In 16 days, the tumor grew to 254% of its pre-treatment tumor volume. The SaO_2 maps of this animal were changing very dynamically and it appeared that there was a correlation between areas of high SaO_2 and the region towards which the tumor was growing. For example, on the top right corner of the baseline SaO_2 map of the MWC, there was a relatively high SaO_2 of approximately 0.5-0.6. However, there was no GFP signal in this region. The SaO_2 of that area remained in the high range over time and it coincided with the tumor eventually growing into that region. On the other hand, the left part of the tumor had a relatively low SaO_2 in the range of 0.2-0.3 and there was a corresponding weakening of the GFP signals in that region over time. However, it was unclear why there was an abrupt elevation of SaO_2 of the entire MWC at the 74-hour imaging time point. Aggressive tumors are often plagued by ill-developed and leaky vessels. One possible explanation for the increase in SaO_2 across the whole MWC could be the growth of

such vasculature and there was, at that point, an over supply of oxygenated blood. Since the GFP signal at the 74-hour time point seems to have weakened as compared to the previous imaging time point, it could be that the metabolic activity of the tumor decreased. The lower metabolism and over supply of oxygenated blood could have contributed to the elevated SaO_2 .

7.6   Further discussion about the study

Motivated by a need to investigate if chemotherapy brought about early changes in SaO_2 that could help predict response to treatment, this proof of concept study was carried out. The study demonstrated that the fluorescence and spectral imaging system was able to monitor dynamic changes in the SaO_2 in the MWC that might occur in the early stages (within 3 days) after chemotherapy. Together with MRI, the multimodal imaging capabilities were used to correlate the SaO_2 changes in the tumor and normal surrounding tissue with ultimate responses to treatment. Table 7.2 summarizes the results of animal experiments that were done with MDA-MB-231 and MCF-7 breast cancer xenografts.

A total of 6 animals were used in this commbined study, one of which was excluded from the analysis due to tissue injury and presence of bleeding. Of the 5 remaining animals, 2 were controls while 3 were treated with identical chemotherapy protocols. Based on tumor volume measurements, one animal from each cell line was found to have responded to the treatment. For the responding MDA-MB-231 animal, there was a cyclic variation in mean tumor SaO_2. Two spikes in mean tumor SaO_2 occured at the 6- and 29-hour time points. At those time points, the mean tumor SaO_2 values were 11% and 19% above baseline. In contrast, for the responding MCF-7 animal, the mean tumor SaO_2 was consistently below baseline. In both responding animals, the difference in mean SaO_2 between tumor and surrounding tissue became greater over time compared to baseline values. In the case of the responding animal with a MDA-MB-231 tumor, the mean baseline SaO_2 of the normal surrounding tissue was lower than that of the tumor tissue. 51 hours after

chemotherapy, the mean SaO_2 of the normal surrounding tissue decreased, while that of the surrounding tissue remained approximately the same as baseline. On the other hand, for the responding animal with a MCF-7 tumor, the mean baseline SaO_2 of the normal surrounding tissue was higher than that of the tumor tissue. 74 hours after chemotherapy, the mean SaO_2 of the tumor decreased significantly, while the decrease of the mean SaO_2 of the surrounding tissue was modest.

Figure 7.8 is a scatter plot of the percent change of mean SaO_2 in all 5 animals, which consist of both cell lines. Data for the animals that responded to treatment are depicted in red while the rest are depicted in black. From this plot, it is inconclusive whether differences in mean SaO_2 in the MWC model can predict ultimate response to chemotherapy. A larger study is necessary to further investigate if the tissue oxygenation changes observed in responding patients can be recapitulated in animals. It is also possible that the metabolic rate in mice greatly differs from human patients and changes may have taken place much more rapidly after receiving treatment. Thus, more frequent monitoring of the SaO_2 changes might be needed. Lastly, characteristics of clinical disease are rarely fully represented by xenografts grown from cultured cell lines. As a result, this study could be improved by the use of a more representative animal model, such as the use of PDX models (to be discussed in Chapter 10).

Table 7.2: Summary of chemotherapy and SaO_2 results of two sub-types of breast tumor xenografts.

Cell line	Animal	ROI	Response to chemo.	Trends of % change of SaO_2 from baseline
MDA-MB-231	#1	T	Yes	Cyclic behavior. 11% and 19% increase at 6 and 29h after chemo. Near baseline at other times.
MDA-MB-231	#1	S	Yes	Consistently below baseline.
MDA-MB-231	#2	T	Control	Small increase before plunging to 46-58% below baseline.
MDA-MB-231	#2	S	Control	Slight decrease before gradually climbing to 22% above baseline.
MCF-7	#1	T, lobe 1	No	Mostly above baseline. Max. increase of 13% at 20h after chemo.
MCF-7	#1	T, lobe 2	No	Within ±15% of baseline before sharply increasing to 113% above it.
MCF-7	#2	T	Yes	Consistently below basleine.
MCF-7	#2	S	Yes	Spiked to 15% above baseline before falling below it, through the rest of the monitoring period.
MCF-7	#3	T	Control	Mostly below baseline before jumping to 26% above at the last time point.
MCF-7	#3	S	Control	Fluctuated between ± 35% about baseline.
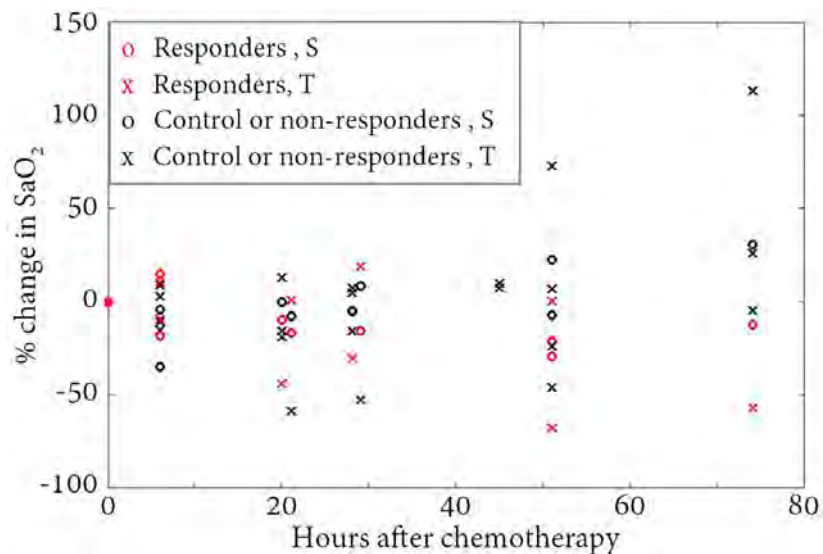
Figure 7.8: A combined plot of percent change in mean SaO_2 of animals that had either MDA-MB-231 or MCF-7 tumors. Red corresponds to responders while black corresponds to either control or non-responding animals. The markers 'o' and 'x' are used to depict surrounding tissue (S) and tumor (T) ROIs, respectively.

CHAPTER 8

Nuclear Imaging of the MWC

8.1   Pre-clinical 3D PET imaging using the ModPET system

Another imaging modality routinely used in hospitals to detect and evaluate cancer is positron emission tomography (PET). PET is a nuclear imaging technique done with trace amounts of radiopharmaceuticals. Examples of positron-emitting radionuclides suitable for PET imaging include ^{11}C, ^{15}O, ^{18}F, ^{64}Cu and ^{68}Ga. By combining them chemically with suitable agents to produce radiopharmaceuticals, they can be used to study a range of physiological phenomena such as hypoxia (^{64}Cu-ATSM[†]and FMISO[†]) and glycolytic metabolism (^{18}F-FDG[†]).

The half life of radionuclides is an important consideration for practical use. FDG (short for ^{18}F-FDG) has a half life of 109.7 minutes, which is sufficiently long for performing a PET scan, yet decays fast enough to have negligible remaining radiation within a day. FDG is currently the most common radiopharmaceutical used for tumor detection. FDG is often introduced as an analog to regular glucose. Figure 8.1 shows a drawing that compares the two molecules. FDG is structurally similar to glucose except a ^{18}F isotope replaces the hydroxyl group on the 2-carbon of the glucose molecule. Both glucose and FDG are actively transported into the cytosol of live cells through processes facilitated by a family of glucose transporter (GLUT) proteins. Once inside cells, glucose and FDG are phosphorylated into glucose-6-phosphate and FDG-6-phosphate, respectively. Unlike glucose-6-phosphate, FDG-6-phosphate cannot undergo further glycolysis through conversion into fructose [100]. Instead, it accumulates and is retained intracellularly.

Malignant tumor cells exhibit abnormally high levels of glycolytic metabolism and over-expresses certain glucose transporters such as GLUT-1 and GLUT-3. In

---

[†]Refer to Appendix A for full chemical name.

contrast, normal cells predominately undergo oxidative phosphorylation for energy production. As a result, the uptake rate of FDG is significantly higher in malignant cells and cancer tissue has more signal in a PET scan. It should be noted that FDG is not cancer specific and does accumulate in regions where there are high levels of metabolism such as inflammed or injured tissue undergoing tissue repair. In the context of WC experiments where the animal has undergone surgical implantation of the WC structures, these factors have to be taken into consideration when interpretating imaging results.

(a) (b)
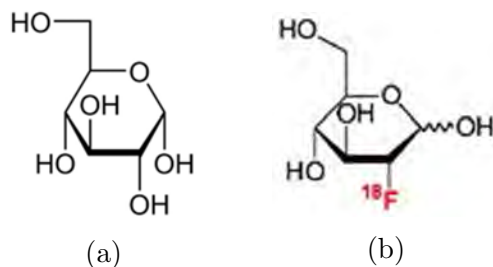
Figure 8.1: Molecular structure of (a) glucose and (b) FDG.

Figure 8.2 illustrates the radioactive decay of ^{18}F isotope on the FDG molecule. An unstable parent radionuclide first undergoes positron emission whereby a positron (β^+ particle) with high kinetic energy is emitted. It gradually loses kinetic energy, predominantly through Coulomb interactions with electrons. As a consequence of the random change of the direction due to each scatter event, a positron traces a tortuous path. There are a number of different outcomes for positrons [101] but the majority ($\approx 63\%$) of them undergo free annihilation with an electron after having reached thermal energy (100 eV or less) through dissipating most of the kinetic energy. It is estimated that the radial range over which 90% of the positrons travel in water before annihilation is 1.8mm [102]. Generally, the higher the kinetic energy of the positron, the larger the penetration depth in the medium [103]. When a positron finally encounters and annihilates with a free electron, a pair of counter-propogating 511keV gamma rays are emitted. However, variations in the linear momentum of the positron and electron can give rise to the emmission of a pair of gamma rays that are slightly different from 180° with respect to each other. The

mean free path of a 511keV photon is approximately 7cm in tissue [104] and since the cross-sections of mice are smaller than that, absorption and/or compton scatter of the gamma rays are negligible. For the MWC experiments described in this work, the ModPET imaging system built and characterized by Stephen Moore [105] was used to detect the emitted gamma rays and reconstruct the spatial distribution of FDG uptake in an animal.

^{18}F-FDG $\xrightarrow{\text{Positron emission}}$ β^+ $\xrightarrow[\text{an electron}]{\text{Annihilation with}}$ $2\,\gamma$ (511 keV)
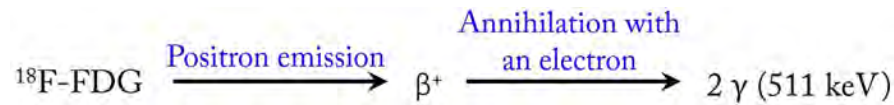
Figure 8.2: Decay process of FDG.

In this system, two stationary gamma ray cameras are placed on opposite sides of the animal, as shown in Figure 8.3(a). The gamma ray camera consists of a 25mm thick Thallium doped Sodium Iodide scintillator, NaI(TL), coupled to a 3×3 PMT array. The counter propagating gamma rays are detected by gamma ray detectors on opposite sides of the body and the time of arrival are recorded during the experiment. A pair of gamma rays which arrived within a stipulated time window (i.e. coincidence resolving time) on opposite gamma ray detectors is regarded as an coincident event. The search for coincident events is done in software. There are 18 PMT readings (9 from each gamma ray camera) associated with a coincident event. The mean-detector-response-function (MDRF), that is pre-determined from measurements, allows the maximum likelihood estimation of the spatial location on the camera where a gamma ray hit. By performing the maximum-likelihood estimation for both gamma rays associated with a coincident event, a line-of-response (LOR) is determined. This calculation is performed for all the detected coincidence pairs and a list of LOR are obtained.

Not all recorded coincident events are true coincidences. In fact, coincidence events can fall into one of the following three categories: true, scattered and random. True coincidence occurs when counter-propagating gamma rays were emitted during an annihilation event and the pair of rays were unscattered before detection. A schematic illustrating this is shown in Figure 8.3(b). On the other hand, scattered

events are the result of positron annihilating with a bound electron and when the emitted gamma rays have undergone one or more Compton scatter events before detection. As a result, the path of the emitted gamma ray pair is not colinear. Coincident signals that originate from two different annihilation events constitute random coincident events.

Since there are different possibilities (true, scattered and random coincidence events) that result in a LOR, the location where the electron-positron annihilation occured has to be estimated based on the their associated probabilities. A list-mode maximum-likelihood reconstruction algorithmn[†] is implemented to estimate the voxels in the 3D space between the gamma ray cameras where the electron-positron annihilation events occured. In the end, 3D reconstruction of the FDG distribution in the animal is obtained.

(a)   (b)
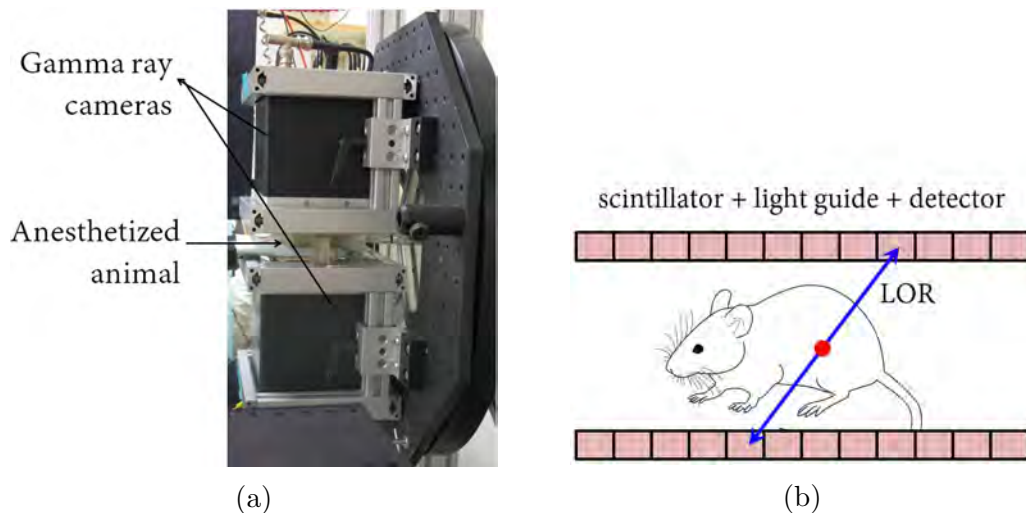
Figure 8.3: ModPET system. (a) Photograph of the ModPET system. (b) Schematic of positron/electron annihilation event (red dot) giving rise to counter-propagating gamma rays (blue arrows). Detection of near simultaneous events on two detectors establishes a line-of-response (LOR).

[†]Refer to Section 5.8 of [105] for details of the list mode maximum-likelihood expectation-maximization algorithmn implemented.

8.2   2D nuclear imaging with a β-imager

The previous section described a 3D tomographic method to image the FDG uptake distribution. The system requires sophisticated hardware and electronics to handle the large amount of raw data needed for subsequent 3D reconstruction. In this dissertation, work was also done to explore the use of a 2D β-imager [106] as an alternative method to study glycolytic metabolism.

With reference to Figure 8.2, instead of gamma-rays, this 2D nuclear imaging methodology relies on the detection of positrons that have escaped through the WC before having a chance to annihilate with an electron. A 3μm ultrathin P47 phosphor is used to absorb the positron's energy and emit visible light that can be detected by a CCD or CMOS detector. P47 is a trade name for a rare earth scintillator, $Y_2SiO_5:Ce^{3+}$, otherwise known as yttrium silicate activated with cerium[†]. The doping of yttrium silicate with Ce^{3+}, which has a larger ionic radius than Y^{3+} [107], creates crystal defects and, hence, emitting centers in the material. The exact emission spectra of the P47 was not measured but several references indicate that the emission range is from 350 - 700nm [108, 109]. A high-quality scientific-grade CCD detector (Roper Scientific, VersArray 1300B) was used to detect the optical emission. It has a quantum efficiency greater than 65% in that spectral range and is well suited to image the visible light from the scintillator.

The ultrathin scintillator used in the MWC experiments consists of a 3μm layer of P47 powder that was deposited on a 3μm thick transparent Mylar substrate [106]. It was cut to shape and placed in direct contact with the tissue in the MWC after the coverslip was removed. The animal was placed in a supine position in the mouse holder and the MWC imaged with a pair of Nikon Nikkor 50mm f/1.2 camera lenses. The lenses were configured to work at unit magnification. Imaging was done within a light tight chamber as illustrated in Figure 8.4.

There are several key features that make the experimental setup suitable for low-light-level applications such as imaging weak luminescence from the ultrathin

---

[†] Often, phosphor is used synonymously with scintillator in the literature.

scintillator. Firstly, the detector employs a back-illuminated design that improves its quantum efficiency. Secondly, the detector is cryogenically cooled to -100°C during experiments to minimize noise due to dark current (0.58 nA/cm^2) . Thirdly, the camera digitization rate and, thus, read out rate can be decreased to 50kHz to minimize read out noise (4.5 e$^-$ @ 50 kHz read out rate). A 1MHz fast read out rate can be used to find best focus and adjust the position of the object. Lastly, imaging takes place within a well-sealed light tight chamber, which prevents room lights from overwhelming the weak signal from the scintillator.
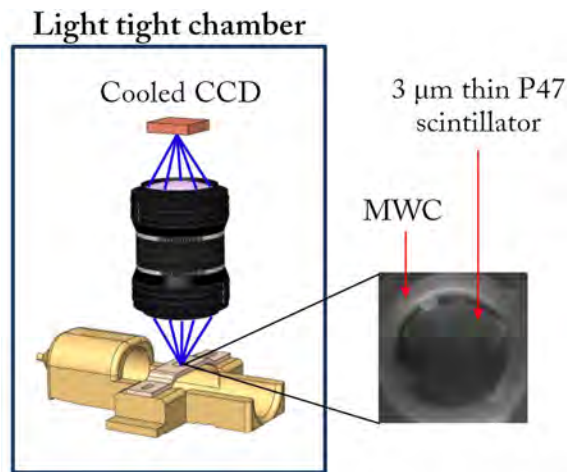
Figure 8.4: Experimental setup of the imaging system.

In addition to imaging luminscence from the scintillator, the system is capable of performing fluorescence imaging. A broadband source filtered with a suitable excitation filter was coupled into a pair of fiber light guides. The light guides were inserted into the imaging chamber through drilled holes. Care was taken to ensure that the openings were well sealed around the fiber light guides so that the chamber remains light tight. An appropriate emission filter was placed between the two camera lenses during fluorescence imaging.

8.3 Experimental results with nuclear imaging in the MWC

8.3.1 Using the β-imager to observe changing phenotype of tumor

As a tumor progresses over time, it's phenotype can evolve and change. This section describes how the nuclear and fluorescence imaging capabilities of the β-imager system were used to compare the glycolytic activity of a MDA-MB-231/GFP breast cancer tumor in a MWC at two different stages of the disease.

The first nuclear imaging experiment with a MWC on the β-imager was carried on day 9 after cell innoculation. For this experiment, the animal was fasted but was given free access to drinking water for about 14 hours before 2.2 mCi of FDG was given through an IV injection. Subsequently, 10-minute exposure images were taken consecutively for the next hour.

A GFP fluorescence image of the tumor taken on the system is shown in Figure 8.5(a) while a nuclear image taken about an hour after the FDG injection is shown in Figure 8.5(b). As it takes time for FDG to be distributed and taken up by cells, it is typical to evaluate images that are taken 30-60 minutes after FDG injection. To help identify the tumor region and the corresponding spatial distribution of FDG, an outline of the GFP image is overlayed on both the GFP (Figure 8.5(c)) and nuclear images (Figure 8.5(d)).

(a) GFP image of MWC.

(b) Nuclear image of MWC.

(c) Outlined of strong GFP signal.

(d) Nuclear image with GFP outline overlayed on it.
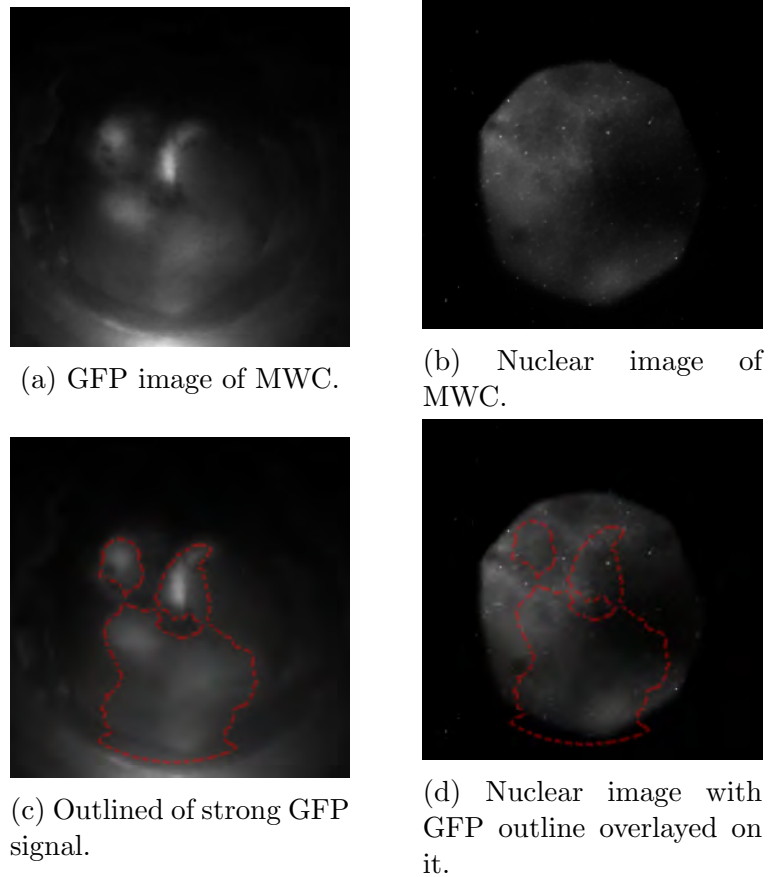
Figure 8.5: Nuclear and GFP fluorescence images of MWC obtained with the β-imaging system. Scintillator on tissue in MWC in all images.

In reference to Figure 8.5(a), it was observed that there is non-uniformity in the strength of the GFP signal in the tumor. This implies that some parts of the tumor may be more viable than others. Secondly, although a large part of the tumor exhibited high FDG uptake, there exists a GFP region that has lower FDG signal. This corresponds to a region of the tumor where GFP signal was relatively weaker. There was also significant FDG uptake in non-tumor regions in the MWC. It is possible that the nearby surrounding region adjacent to the tumor has undergone altered metabolism, resulting in high FDG uptake or this may be associated with a region of inflammation due to the surgery.

Eleven days after that experiment (20 days after cell innoculation), a similar

experiment was carried out on the same animal. The animal received 932 μCi of FDG and 30-minute exposure image acquisitions were obtained on the β-imager. The results are shown in Figure 8.6. Figure 8.6(a) shows the raw image. The salt and pepper appearance is attributed to the gamma rays from annihilation events impinging on the CCD detector directly. The image was processed with a 7x7 median filtering kernal and the result is shown in Figure 8.6(b). Lastly, a GFP image taken on a microscope is shown in Figure 8.6(c).

Figure 8.6(b) shows that, with the exception of a small region in the upper right, the majority of the tissue did not have significant FDG uptake. This is in contrast with what was observed 11 days earlier when more than half of the tissue showed high FDG uptake. There is a clear correspondence in the GFP and FDG images at this time point. In addition, there was little FDG uptake in surrounding regions where there is no GFP signal. This is unlike the earlier results where high FDG uptake was observed within and outside the tumor region (Figure 8.5(d)).

(a)	(b)	(c)
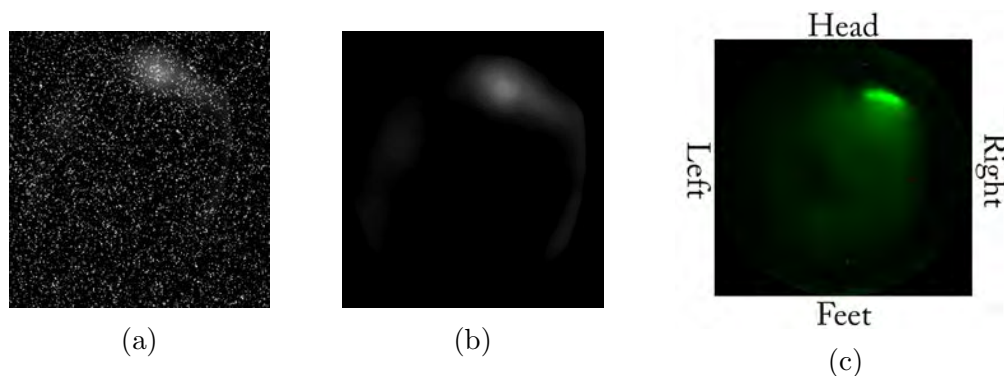
Figure 8.6: Nuclear imaging results on the β-imager and corresponding fluorescence image. (a) Raw nuclear image. (b) Nuclear image after median filtering with a 7x7 kernel. (c) A 1X GFP image of the MWC taken on a fluorescence microscope is shown for convenient side-by-side comparison. Scale between the first two images and the last may differ slightly.

8.3.2   Validation of β-imager results with 3D PET imaging

PET is a well established method in clinical tumor imaging. Therefore, the preclinical PET imaging system, ModPET, was used to validate the nuclear imaging

results obtained on the β-imager. To do that, PET imaging was carried on the same day as when the β-imager results shown in Figure 8.6 were obtained.

The animal was fasted but was given free access to drinking water for about 6 hours before 133 μCi of FDG was given through IV injection. Subsequently, the animal was allowed to recover from anesthesia and was kept warm on a heating pad. Approximately 45 minutes after injection, the animal was put under anesthesia and positioned on the PET system for calibration. Note that the time delay between the injection and imaging was intentional, as it takes time for the FDG to be taken up by and concentrated in the tumor tissue. Before the start of an imaging session, the two gamma cameras were placed 32mm apart and the mouse was positioned between the cameras such that the count rates on both cameras were approximately balanced. As a rule of thumb, the acquisition time for each run of an experiment should be set such that there are approximately a million coincident pairs detected. In this experiment, a 90s acquisition time was sufficiently long to achieve that condition. After preparation was completed, the animal had about 91 μCi of activity remaining and ten sets of PET data were acquired in total. In addition to the PET imaging, a coronal photograph of the mouse was captured to facilitate image registration. This optical image capture capability is part of the ModPET instrument.

The results of this experiment are shown in Figure 8.7. Figure 8.7(a) and (b) show the sagittal and coronal slices of the 3D reconstruction of the FDG distribution, respectively. Figure 8.7(c) shows a coronal image superimposed onto the photograph of the animal. The dotted lines indicate the outline of the MWC. As expected, the strongest signals come from the heart and bladder of the animal. Within the MWC, there is a small area that has three times as much signal as the surrounding region. A blown up image of the hot spot on the MWC is shown in Figure 8.7(d). Figure 8.7(e) is a GFP image that was taken on a microscope using a 1X objective. It shows the large size of the tumor that covers about two thirds of the area of the MWC. Nevertheless, there is a small region that exhibited much stronger GFP signal compared to the rest of the tumor. Comparing Figure 8.7(b) with Figure 8.7(e), it can be seen that the region with high FDG signals corresponds closely

with the region of the tumor that has the strongest GFP signal. The other portions of the tumor, although visible by the GFP signal, did not show high FDG signal. This result exemplifies the fact that heterogeneity is present, even within a single tumor that originated from the same cancer cell line. More importantly, this result corroborates results obtained on the β-imager.
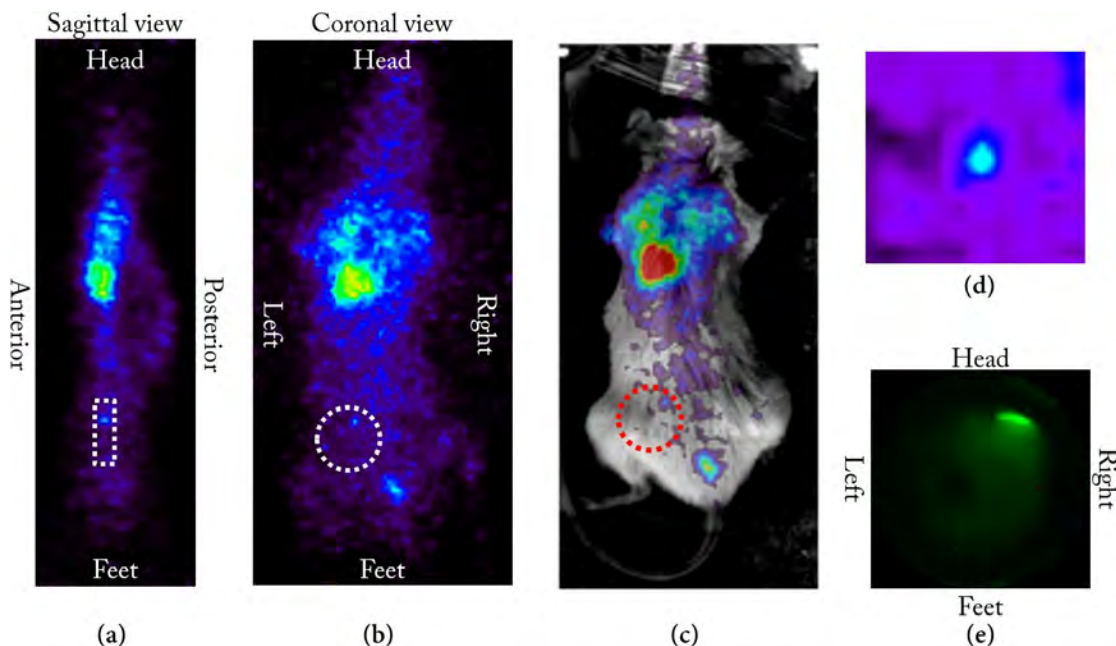
Figure 8.7: PET imaging results. (a) Sagittal view and (b) coronal view of the distribution of FDG in the animal. (c) The coronal PET imaging result superimposed onto a registered optical photograph of the mouse. Dotted lines indicate outline of MWC.

8.3.3   Depth sensitivity of the β-imager

As mentioned in Section 8.1, the radial range for which 90% of positrons travel in water before annihilation is 1.8mm. It is expected that the thin scintillator placed in direct contact with the mammary tissue would be able to detect positron emission that occurs within an approximately 1.8mm thick tissue section below the scintillator. Figure 8.8 shows a typical MRI axial view of a breast cancer tumor in a MWC that, in this case, grew to approximately 4mm below the surface. Therefore, the results from the *beta*-imager would be indicative of the metabolic status of a

large part of this tumor. Given the minimal amount of data processing required and the relatively simple design of the system, the β-imager could be a useful alternative to PET imaging.
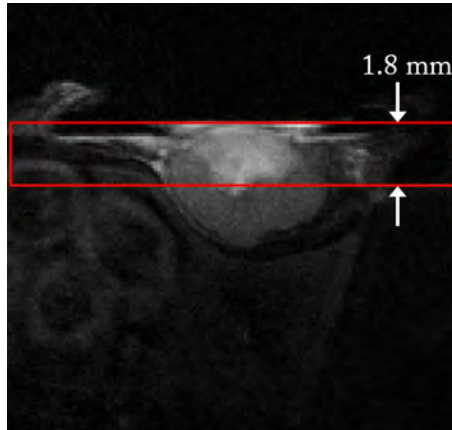
Figure 8.8: GFP image of MWC taken on a microscope.

An experiment with a FDG phantom was carried out to better understand and characterize the depth sensitivity of the β-imager. A capillary tube with a 0.2×4.0mm cross-section containing 847 μCi of FDG was submerged at an approximate angle of 26° in a water bath. A piece of 3μm thick P47 scintillator was placed on the water surface as depicted in Figure 8.9(a). A 10-minute exposure image of the visible luminscence was captured by the β-imager. The result is shown in Figure 8.9(b). The image shown was background subtracted and median filtered with a 3×3 kernel. A contour plot of the normalized signal in that image is presented in Figure 8.9(c). The luminscence intensity, averaged across the 4mm wide phantom, vs the distance of the FDG phantom below the water surface is shown in Figure 8.9(d).

(a)

(b)

(c)

(d)
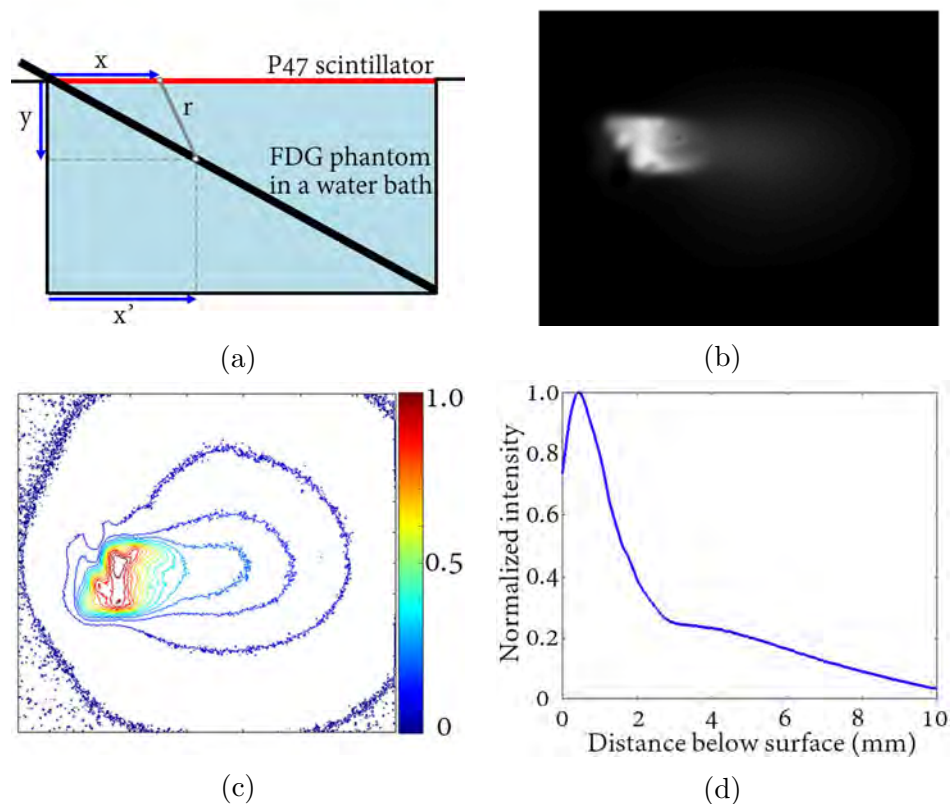
Figure 8.9: β-imager depth sensitivity experimental results. (a) Schematic of experimental setup. A 847 μCi phantom (in black) is submerged in a water bath and a P47 scintillator (in red) is placed on the water surface. (b) A 10-minute exposure image of the visible luminescence. (c) A contour plot of the normalized signal of the luminescence image. (d) A plot of luminescence intensity against distance of FDG below water surface.

Figure 8.9(d) shows that there is a rapid drop in luminscence signal as the distance of the FDG from the scintillator increases from 0 to 3mm. The rate of decrease in luminscence was more gradual as the distance increased beyond 3mm. The extended size of the FDG phantom, the geometry of the setup and the statistical distribution of the positron range in water can explain the observed results.

Figure 8.10, which is reproduced from [110], shows the statistical distribution of ^{18}F positron range in the horizontal direction in water media. It should be noted that the horizontal range is a projection of the 3D radial range.
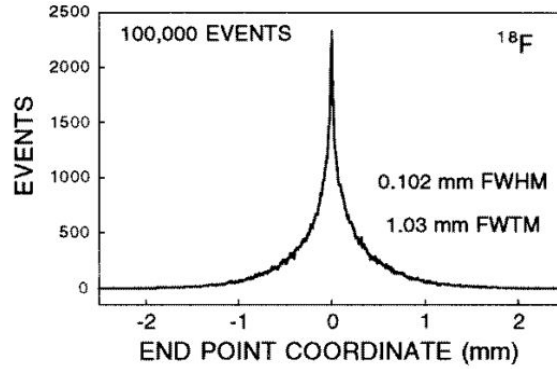
Figure 8.10: Graph, reproduced from [110], showing statistical distribution of ^{18}F range in the horizontal direction in water.

The curve in Figure 8.10 has a cusp-like appearance, which can be modelled by [111]

$$Pr(r) = C\ e^{-\frac{r}{r_1}} + (1 - C)\ e^{-\frac{r}{r_2}}, \tag{8.1}$$

where C, r_1 and r_2 are constants that determine the shape of the curve, and r is the radial distance between a point source position and the detection location. If the phantom is modeled as a line source made up of discrete point sources, the luminescence signal at a particular horizontal position directly above the line source is given by the following equations:

$$r(x'; x) = \sqrt{y^2 + (x - x')^2}, \tag{8.2}$$

$$I(x) = \int_0^L C\ e^{-\frac{r(x';x)}{r_1}} + (1 - C)\ e^{-\frac{r(x';x)}{r_2}}\ dx', \tag{8.3}$$

where x is the horizontal distance along a line on the scintillator that is directly above the line source, y is the vertical distance associated with r and x' is the horizontal position along the line source (Figure 8.9(a)). The equations state that the measured signal at a particular point x along a horizontal line on the scintillator is modelled to be a weighted sum of signals contributed by the discrete point sources along the line source.

By choosing the parameters c $= 0.08$, $r_1 = 0.025$ and $r_2 = 1.35$, the simulated results based on Equation 8.3 is shown in Figure 8.11(a). Although there are differences in the scale of the normalized intensity, the simulated result has the same characteristic curve as the experimental data. Futher work has to be carried out to determine if the distribution of the radial range of positrons in water can be well-represented by Equation 8.1. The plot of the positron radial range distribution that produces that simulated intensity curve is shown in Figure 8.11(b).

In view of these preliminary results, it is concluded that the β-imager is most sensitive to radionuclides that are within 2mm from the surface of the MWC. Since the tumors are typically small and grows close to the surface of the MWC, the β-imager is a viable tool to qualitatively study the glycolytic metabolism of tumors in the MWC. However, due to the non-linearity of the radial range distribution, further work has to be done to enable the system to be used for quantitative measurements.
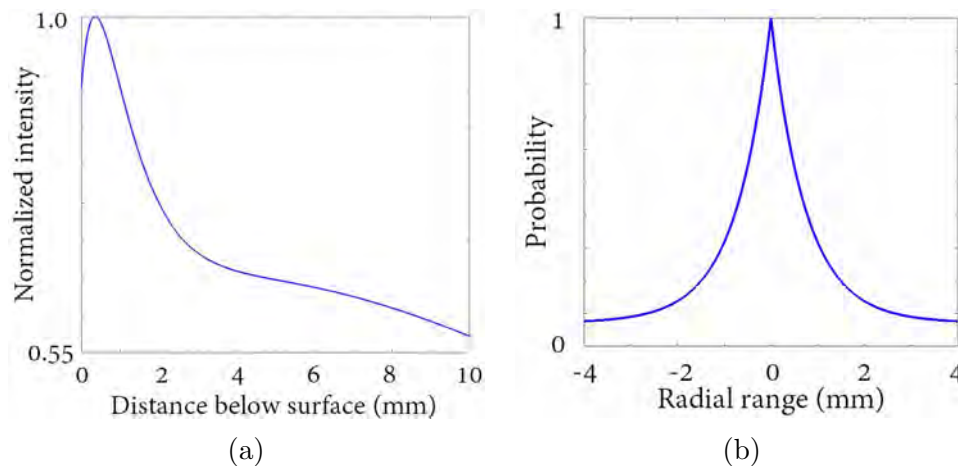
Figure 8.11: Simulated results of the intensity of luminescence based on Equation 8.3.

CHAPTER 9

MRI of the MWC

9.1   Background on MRI

MRI is a non-ionizing 3D imaging method and if imaging and operational guidelines are followed, it poses very minimal health risk to the imaged subject. Because of these features, MRI has found clinical applications ranging from the functional imaging of the brain [112] to the imaging of fetal development [113]. According to a 2013 statistics provided by the Organization for Economic Co-operation and Development, for every 1000 population in USA, there were 106.9 MRI exams being performed [114]. Although it is considered a mature technology that is being widely used in the clinic for a variety of purposes, active research continues to expand its capabilities beyond the current state-of-the-art.

The main components of a MRI scanner consist of a strong superconducting magnet, gradient coils, and RF coils. Because water is abundant in living tissue, the vast majority of MRI scanners are configured to use hydrogen protons in water to provide images. A hydrogen proton, which is a paramagnetic material, can be manipulated with magnetic fields based on the principles of nuclear magnetic resonance (NMR). Each proton possesses a magnetic moment (spin). The sum of these spins gives rise to a net magnetization, $\vec{\mathbf{M}}$. When a sample is placed in a strong homogeneous magnetic field of strength B_o, it's magnetization, $\vec{\mathbf{M}}$, will align with the magnetic field. If $\vec{\mathbf{M}}$ is perturbed away from alignment, $\vec{\mathbf{M}}$ will precess about the direction of B_o. The resonant angular frequency for $\vec{\mathbf{M}}$ as it precesses about the axis, is known as the Larmor frequency, ω. It is dependent on the gyromagnetic ratio (γ) of the proton and the magnitude of the net magnetic field (B_o), as described by the famous Larmor equation,

$$\omega = \gamma \ B_o. \tag{9.1}$$

The direction of the static magnetic field, B_o, of a MRI scanner is traditionally assigned as the z-axis. Gradient coils in the MRI scanner are used to create small gradients in the strong, static and homogeneous B_o field. This creates a spatially varying field such that the Larmor frequency is position-dependent along the gradient direction. This is important for imaging purposes as it enables the selective excitation of an imaging region and enables the return signals to carry information about where it originated from.

To simplify the description of how the magnetization $\vec{\mathbf{M}}$ behaves under the influence of a radiofrequency (RF) magnetic field, the bahavior is considered in a rotating reference frame that has an angular frequency of the circularly polarized RF field whose frequency closely matches the Larmor frequency. In the rotating frame, the net magnetization that is initially aligned along $\hat{z}$, is tipped away from alignment by the RF field. Once the magnetization is tilted away from the z-axis into the transverse plane, the RF field is switched off. The excited magnetization continues to precess about the z-axis as it relaxes back to equilibrium and gradually becomes aligned with the B_o once again. Simultaneously occuring is the dephasing of the individual spins with respect to one another, contributing further to the decrease in the net transverse magnetization. The time constants associated with the decrease of the transverse component due to dephasing and the recovery of the longitudinal component of the spins are known as T2 and T1, respectively. Because T1- and T2-relaxation are dependent on the physical and chemical microenvironment in which the perturbed protons exist, the relaxation parameters provide information about the tissue microenvironment.

A typical MRI sequence consists of repeating sets of RF pulses to manipulate the magnetization in a variety of ways. There are a large number of different sequences that have been designed to accomplish anatomical imaging, as well as specialized applications, such as diffusion-weighted (DW) [115], perfusion [116] and pH imaging [117]. The great beauty of MRI lies in its capability to achieve multiple imaging

techniques easily on the same scanner, often without need to re-configure any hardware. Different information about the living tissue can be extracted by changing the magnitude and timing of the gradient and RF magnetic fields in the scanner, which are computer controlled.

9.2   MRI experimental setup

Figure 9.1(a) shows a Bruker 7T MRI scanner (BioSpec 70/20 USR) with a 200mm clear bore that enables small-animal studies. The scanner is computer controlled with Bruker's MR software package, ParaVision. Different sequences and post-processing algorithms are pre-loaded and available for use. A Bruker linear RF transmit coil and a 12mm diameter ^{1}H single-turn surface receive coil (Doty Scientific, Inc.) were used in the MWC imaging experiments. The surface coil achieves high sensitivity for the tissue under the MWC. The linear RF transmit coil has an approximately 7.2mm inner diameter (Figure 9.1(b)). For imaging, the animal was prepped and the surface coil was fixed over the MWC as shown in Figure 9.1(c). The animal was then positioned inside the transmit coil such that the surface coil position was near the isocenter of the scanner.

MRI experimental results of the MWC, which mainly consist of anatomical imaging, DW imaging, and perfusion imaging of breast cancer tumor xenografts, are presented in the following sections of this chapter.

9.3   Anatomical imaging of the MWC with T1- and T2-weighted MRI

9.3.1   Background

Anatomical MR imaging is acheived by judiciously selecting suitable imaging parameters to provide contrast between different tissue types. Images that emphasizes the differences in T1 or T2 are termed T1- and T2-weighted images, respectively. T1 relaxation, also known as spin-lattice relaxation, occurs due to spins "tumbling" and transferring energy to the lattice. T1 relaxation is most effective when the "tumbling" rate is close to the Larmor frequency. On the other hand, T2 relaxation
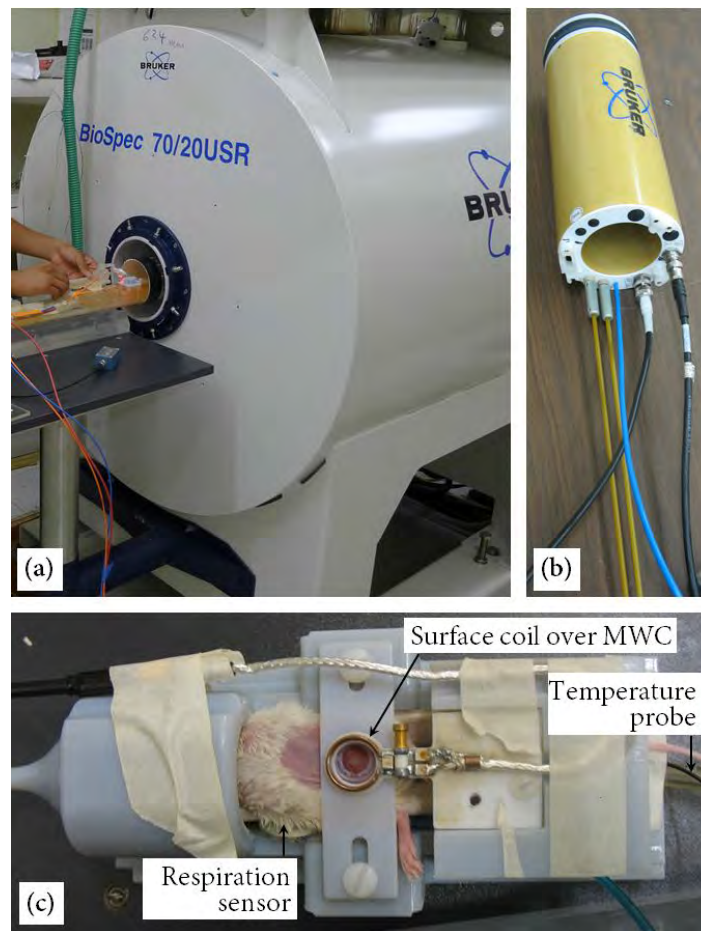
Figure 9.1: MRI experimental setup. (a) A Bruker 7T BioSpec 70/20 USR MRI scanner. (b) Linear transmit coil that has an approximate 7.2mm inner diameter. (c) An anesthetized mouse with a single-turn surface receive coil placed over the MWC. Body temperature and respiratory monitoring systems were used during animal experiments.

is often known as spin-spin relaxation. It arises due to the magnetic field of individual spins which introduces non-uniformity to the local magnetic field. As a result, the variation in magnetic field sensed by individual spins leads to each of them experiencing a slightly different resonant frequency and, hence, they become dephased over time. From various studies performed at different field strengths [118–121], approximate T1 and T2 values of selected tissue types are given in Table 9.1.

Table 9.1: Approximate T1 and T2 values of different types of tissue

Tissue	T1 (ms)	T2 (ms)
Water	4600	2000
Muscle	1000	50
Fat	250	70
Blood	2000-2800	15 (venous), 46 (arterial)

One of the common MRI sequence is the spin-echo sequence in which a 90° RF pulse is used to initially excite the magnetization and a 180° RF pulse is used to refocus signal at a delayed time, referred to as the echo time (TE). In MRI, Fourier data of an object are acquired line by line using multiple repetitions of the sequence with different spatial weighting. The time between each repetition is called TR. The general expression of the MRI signal of a spin echo sequence is given in Equation 9.2,

$$S = \rho \left[1 - e^{\left(-\frac{\text{TR}}{\text{T1}}\right)} \right] \ e^{\left(-\frac{\text{TE}}{\text{T2}}\right)}, \tag{9.2}$$

where ρ is the proton density. T1 and T2 image weighting can be achieved by selecting suitable TR and TE parameters.

9.3.2   Experimental results of anatomical imaging

A Multi-Slice Multi-Echo (MSME) MRI sequence and a Rapid Acquisition with Relaxation Enhancement (RARE) [122] were used to obtain multiple slices of 2D T1-weighted and T2-weighted images, respectively. By collecting multiple sequential image slices that span the MWC, 3D anatomical information can be obtained.

Typical parameters used in a MSME and RARE sequence to obtain 2D image slices of the MWC xenograft are given in Table 9.2.

Table 9.2: Typical parameters used in MSME and RARE MRI sequences

Parameters	MSME, T1-weighted	RARE, T2-weighted
TR (ms)	500	5000
Effective TE (ms)	10.7	56
FOV (mm)	25.6	25.6
Number of slices	15	15
Slice thickness (mm)	1	1
Slice gap (mm)	0.2	0.2
Pixel size (μm)	100	100
Image matrix size	256×256	256×256
RARE factor	N.A.	8
Fat saturation	No	Yes
Number of averages	1	2
Imaging duration (min.)	2.1	5.3

Figures 9.2(a) and (b) show 5 sequential axial slices of a MWC MDA-MD-231 tumor xenograft obtained with T1- and T2-weighting sequences, respectively. To illustrate the differences in the images produced by the two different sequences, the center slice of Figures 9.2(a) and (b) are expanded, annotated and shown in Figures 9.2(c) and (d), respectively.

Tumor appears darker than surrounding tissue on T1-weighted images as tumor tissue has a longer T1. On the other hand, the mammary fat pad that surrounds the tumor has a shorter T1 and appears brighter than the tumor.

Due to its higher T2 value, tumor tissue shows up bright on T2-weighted images. The T2-weighted image shown in Figure 9.2(d) reveals tumor heterogeneity that was not seen in the T1-weighted image. Possible explanations for the heterogeneous appearance of the tumor include the presence of higher amounts of deoxyhemoglobin in the darker regions and higher water content in the brighter regions. Abnormally high water content suggests the onset of necrosis. Due to the high contrast of the tumor with respect to the surrounding tissue, T2-weighted images are often used to calculate tumor volume and monitor tumor growth rates.
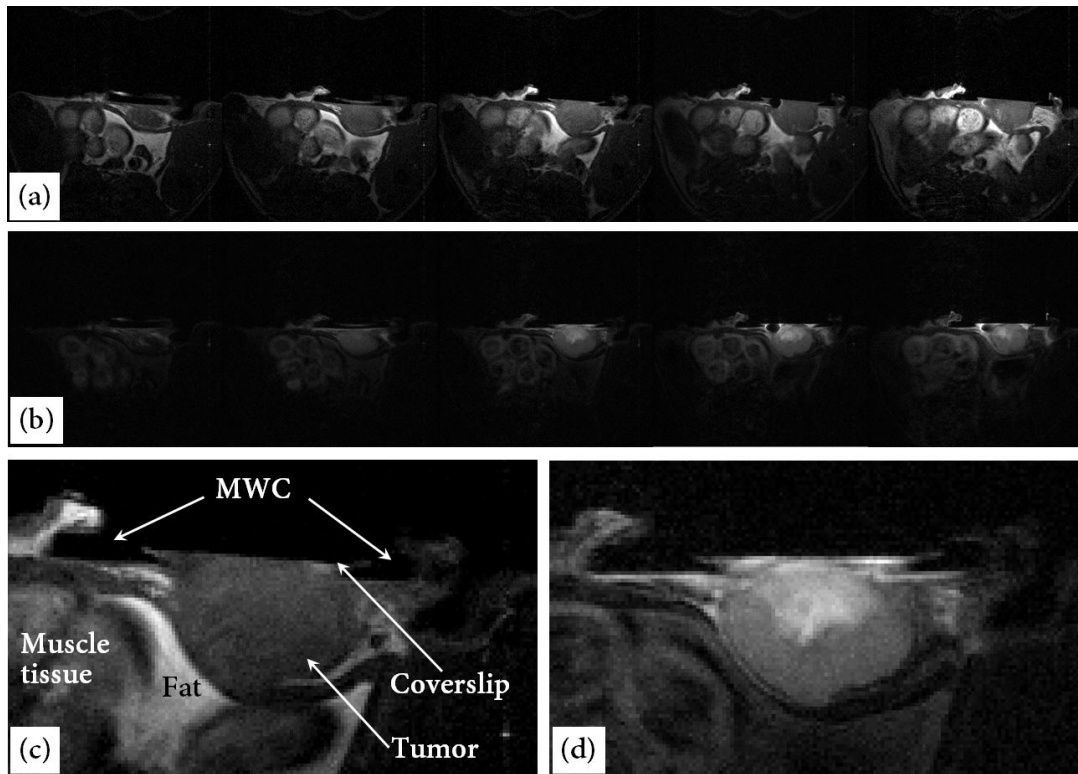
Figure 9.2: T1- and T2-weighted axial images of a MDA-MD-231 xenograft. (a) 5 slices of T1-weighted axial images of the tumor. (b) Co-registered slices of T2-weighted images. (c) and (d) are expanded views of the middle slice image shown in (a) and (b), respectively.

T1-weighted coronal images of the same animal are shown in Figure 9.3. Coronal images are those parallel to the surface of the MWC. The leftmost image represents the slice closest to the surface and progressively deeper sections of the MWC are shown on the right. Imaging parameters are similar to those used for T1-weighted axial imaging (Table 9.2). Coronal images can be used to identify the location of non-fluorescent tumor (e.g. PDX) with respect to the MWC and are useful in co-registering tumor location with MWC images obtained from other imaging modalities.
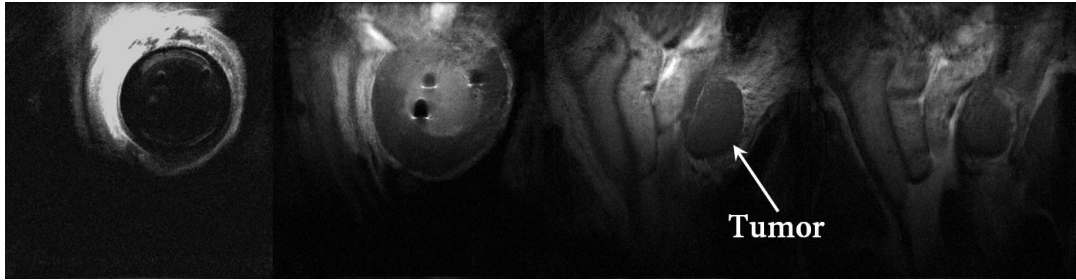
Figure 9.3: T1-weighted coronal images of a MDA-MB-231 xenograft. The topmost (left) and three other deeper coronal sections of the MWC are shown.

A few examples of axial T2-weighted images of MCF-7 xenografts are shown in Figures 9.4(a)-(c). The images are cropped to show details of the tumor more clearly. These are MR images of the MCF-7 MWC animals that received chemotherapy in the study discussed in Chapter 7. The MR images were taken 4 days after administration of chemotherapy. The animals associated with Figures 9.4(a)-(c) correspond to those of Figures 7.5(a)-(c). The axial images of the treated animal shown in Figure 9.4(c) shows evidence of necrosis in the middle part of the tumor where there is a signal void. Interestingly, with reference to the last GFP image in Figure 7.5(a), there was a weakening of GFP signals at the center of the tumor 4 days before the MR images were taken. Similar comparisons can be made with the other animals and this illustrates how multimodal imaging of the MWC helps to extract different types of information about a tumor xenograft.
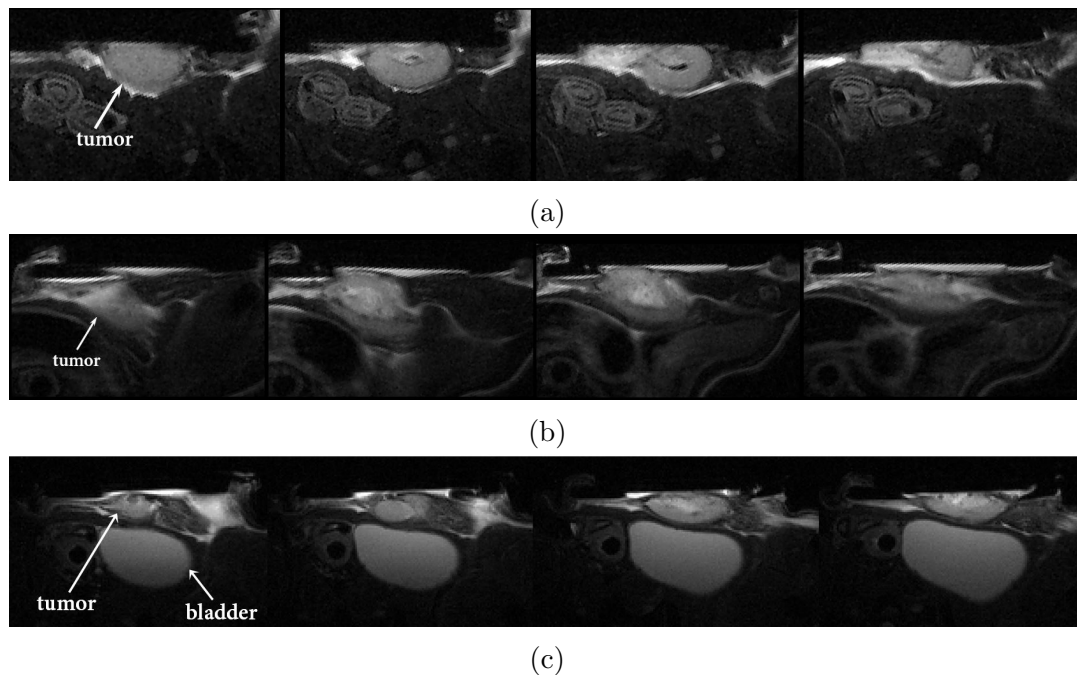
Figure 9.4: Axial T2-weight images of MCF-7 xenografts in animals that received chemotherapy 4 days before. Images shown in (a) - (c) correspond to images belonging to three different animals.

9.4 Diffusion-weighted MRI

9.4.1 Background

Anatomical imaging allows the visualization of the tumor and organ structures on the macroscopic level. However, the early changes that accompany tumorigenesis and the evolution of the disease often occur at the cellular level. Diffusion-weighted (DW) MRI, otherwise known as diffusion-weighted imaging (DWI) is a method of quantifying the effective displacement of water protons due to brownian motion. By quantifying water mobility in tissue, it is possible to obtain information and understand certain aspects of the tissue of interest at the cellular level. For instance, a low apparent diffusion has been associated with the restriction of water movement in highly cellular tumors (i.e. 600-900 cells/high power field[†]). The presence of

---

[†]Cellularity, as defined by the number of cells/high power field, refers to the number cell count in a 400X microscope image.

macromolecules and highly disorganized tissue structures have also been thought to lead to lower diffusivity of water molecules. Currently, although the exact physical mechanisms that lead to lower effective diffusion in malignant tissue remains a point of contention, DWI has been evaluated in its capability to detect and evaluate tumors [123, 124] and as an early biomarker of treatment response [125, 126]. There is a strong interest in making DWI more integrated into clinical practice, however, various proposed clinical applications requires further validation [115]. The MR-compatible MWC murine model presents an opportunity to evaluate the utility of DWI for cancer studies. In this section, the application of DWI to study breast cancer xenografts *in vivo* is presented.

The common method of making MRI sensitive to diffusion processes is through the use of pulsed gradient fields [127]. A simplified version of the DW spin-echo MRI sequence is shown in Figure 9.5.
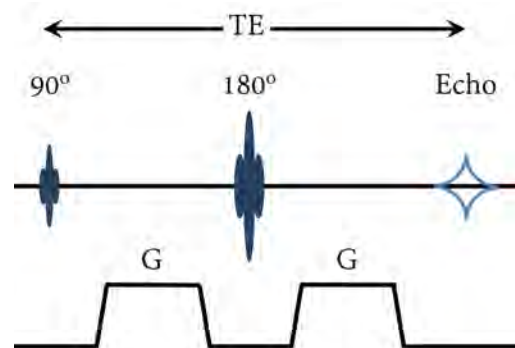
Figure 9.5: A diagram showing the spin-echo MRI sequence used for DW imaging.

By first applying a 90° RF slice excitation pulse, water protons in a desired tissue location are excited into the transverse plane. These magnetically excited spins can then act as freely diffusing endogenous tracers. Subsequently, a pulsed gradient alters the Larmor resonant frequency of the transverse spins by imparting a phase shift to those spins. This is then followed by a 180° pulse that is applied to invert the phase of the spins. Because of the 180° phase flip, the subsequent similar gradient pulse has the effect of rewinding the phase shift that was imparted by the first gradient pulse. However, in the presence of diffusion of the transverse spins, there

is a net displacement of the spins during the time period between the two gradient lobes. As a consequence, the second gradient lobe does not completely undo the phase acquired by the spins before the 180° pulse was applied. The net residual distribution of phases results in a signal attenuation, which can be expressed as

$$S = S_o e^{-<\phi^2>} = S_o e^{-bD},$$
(9.3)

where S and S_o are the attenuated and unattenuated signals respectively, and ϕ represents the residual phase of the moving spins, which has a Gaussian distribution. The b value is a parameter determined by the strength and the timing of the gradient lobes. The general form of b is given by

$$b = \gamma^2 \int_o^{TE} \left[\int_0^t G(t')dt' \right]^2 dt,$$
(9.4)

where γ is the Larmor frequency, TE is the echo time, G is the gradient applied during DWI sequence and t is the length of time that the gradient was applied. The mean diffusion distance, D, is expressed by

$$D = \frac{1}{2t} \left\langle (\vec{r} - \vec{r_o})^2 \right\rangle,$$
(9.5)

where $(r - r_o)$ is the net displacement of the spins during the length of time, t. A more detailed mathematical description of the various parameters involved in DW MRI can be found in [128].

Pure water at ambient temperature has a D value of approximately 2.4 x 10^{-3} mm^{2}s^{-1} [129]. However, in living tissues, the value tends to be smaller because factors such as compartmentalization, viscosity of macromolecules, and tortuosity of the extravascular space can restrict the diffusion process. Therefore, what is measured in MRI is the apparent diffusion coefficient (ADC). A large range of ADC values for pathological tissues have been reported.

9.4.2 Experimental results of diffusion-weighted imaging

An example of DWI of a MDA-MB-231 MWC xenograft is presented in this section. A series of T2-weighted images of the MWC were acquired to enable the selection

of a suitable location to perform DWI. In this case, a 1mm thick axial slice at the isocenter was selected. Next, DWI in three orthogonal directions of the diffusion gradients was performed. In each direction, 10 different b-values ranging from 0 to 1600 s/mm^2 were used. Six representative raw DW images are shown in Figure 9.6. As the b-value associated with a certain gradient direction increases, the sensitivity of the MRI signal to diffusion in that direction increases. As a result, signals attenuate more significantly, in accordance with Equation 9.3. Figure 9.7 shows plots of the signal variation with different b values at two different locations in the tumor.
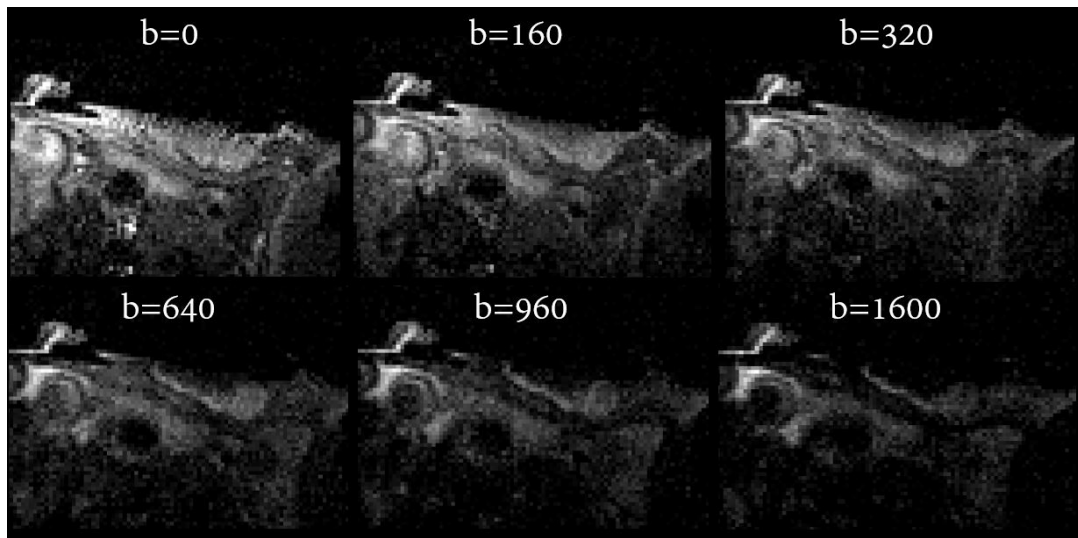
Figure 9.6: Raw images obtained by applying different b-values in the MRI sequence.
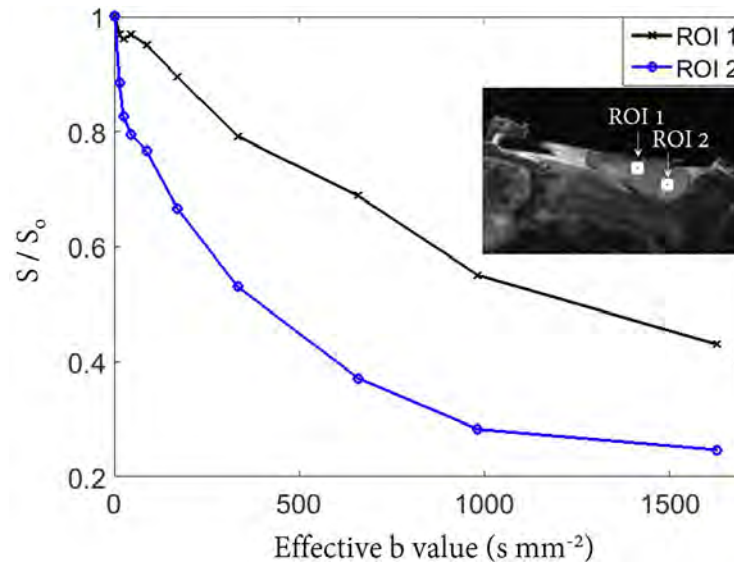
Figure 9.7: Variation of normalized signal, S/S_o, of two ROIs were plotted against the effective b values used during the DW MRI sequence. Inset shows the locations of the two ROIs in the tumor tissue.

The signal change with respect to b-values at each spatial location was fitted to an exponential decay as shown in Equation 9.3, which allows a map of apparent diffusion coefficient, ADC, in the three orthogonal directions to be derived. Figure 9.8(a) shows a cropped T2-weighted image of the MWC that shows the ROI of the tumor. Figures 9.8(b)-(d) show the ADC maps associated with the x-, y-, and z-direction. Black pixels in the images indicate poor fitting results ($R^2 < 0.5$). Poor fitting could be a result of low signal levels and motion artifacts. From the ADC values associated with the 3 orthogonal directions, a map of the root mean squares of ADC was computed. The result is shown in Figure 9.9.

In this animal, the T2-weighted image showed a fairly uniform signal across the tumor. However, the ADC maps in Figures 9.8(b)-(d) reveal that the mobility of water within the tumor was heterogeneous. There was a higher mobility of water protons in a tumor region close to the surface, as compared to the lower regions of the tumor. It is known that necrotic cells swell and their cell membranes are compromised [130]. Since enlarged cells sizes and compromised cell membranes would result in less restriction in water mobility, the high ADC values in the tumor

could imply the onset of necrosis. Typically, viable and intact tumor cells have lower ADC values than normal tissue because tumor cells are often densely packed with a large degree of restriction.

In the image shown in Figures 9.8(b)-(d), the ADC maps of the tumor in the three directions appear to be very similar and this implies that the water mobility is isotropic in the tumor. Nevertheless, there are regions outside the tumor that have anisotropic ADC values. For instance, there is a strip of tissue under the tumor (indicated with an arrow in Figure 9.8(d)) that has relatively higher ADC values in the z-direction than in the x- and y-directions. One possible explanation could be the presence of muscle tissue with fibers oriented along the z-direction. Nevertheless, other factors such as the presence of extracellular fibrosis and glandular formations could also be responsible for the variations in the diffusion directionality [115].
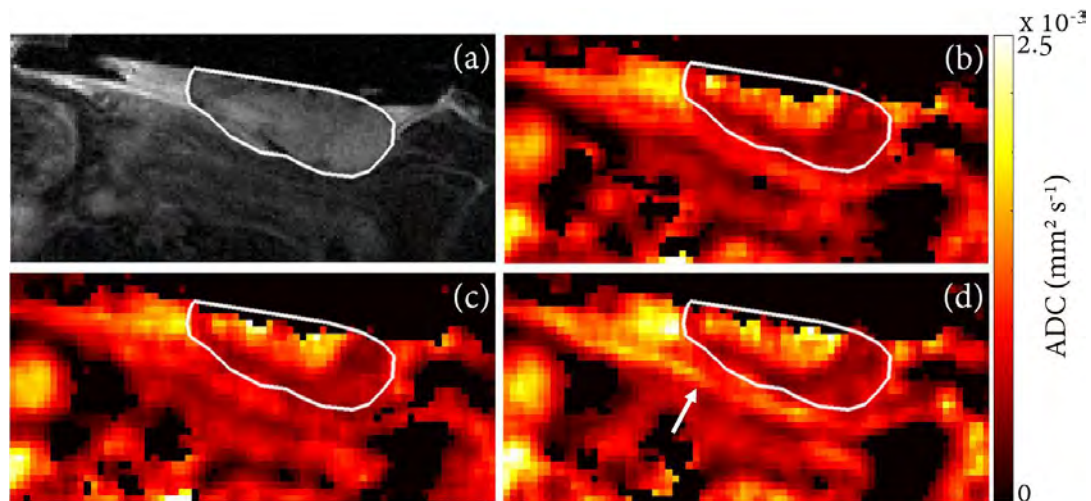
Figure 9.8: Anatomical image and DWI results. (a) A cropped T2-weighted image showing the selected ROI of the MWC. (b)-(c) are ADC maps of the ROI in x-, y-, and z-directions. The outline of the tumor is superimposed on all images for easy visualization.
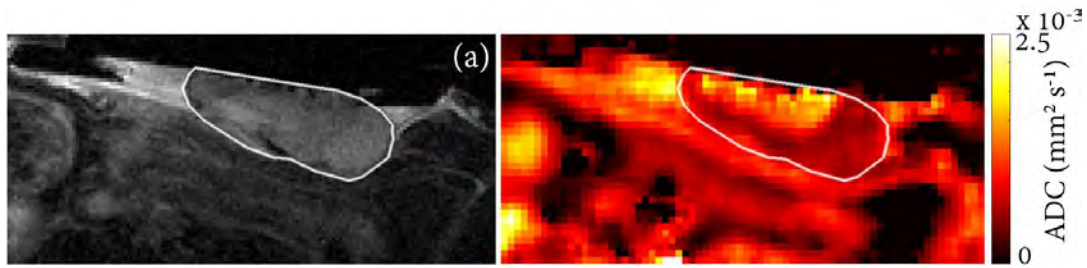
Figure 9.9: Anatomical image and DWI result. (a) A cropped T2-weighted image shown here for easy comparison side-by-side comparison. (b) A map of the magnitude of ADC with an outline of the tumor superimposed on it

9.5 Perfusion Imaging in the MWC

9.5.1 Background

DW imaging is a method of studying the incoherent Brownian motion of magnetic spins in the extravascular space of tissue. Perfusion imaging, on the other hand, enables the study of steady-state delivery of blood to tissue through the microcirculation in the capillary network [131, 132].

One of the motivations of performing perfusion imaging in MWC is to use it as a tool to understand oxygenation changes that occur after NAC (refer to Chapter 7). Although it is possible to extract information about perfusion through a number of different imaging techniques [133, 134], it is desirable to use MRI to image perfusion in the MWC for a number of reasons. Firstly, the MWC model is MRI compatible and the advantages of MRI being a non-invasive, non-ionizing 3D imaging modality have been highlighted. MRI also was extensively used to image the anatomy and growth rates of the MWC tumors. Extending the capabilities of MRI to perfusion studies requires minimal additional costs and hardware re-configuration. Secondly, there are various well established MRI imaging methods that are capable of achieving quantitative and qualitative perfusion imaging. Many of these techniques have been applied to study blood perfusion in the brain [135], lungs [136] and liver [137]. Therefore, the approach taken in this dissertation work is to adapt well-established MRI sequences to MWC studies. To the best of the author's knowledge, there has

not been any published work on the application of MRI perfusion imaging to study breast cancer tumor xenografts in a MWC murine model. Lastly, being able to obtain co-registered anatomical images and perfusion maps of the tumor on the same imaging modality is convenient in the subsequent analysis and interpretation of the results.

There are four main ways of studying perfusion with MRI, namely through the use of intravoxel incoherent motion (IVIM) imaging methods, dynamic susceptibility contrast (DSC) enhanced methods, dynamic contrast enhanced (DCE) methods, and arterial spin labelling (ASL) methods. Because of the random directions of microcirculation in capillaries, water proton microcirculation affects the signal obtained in diffusion imaging. This is most significant at low b-values due to high degree of motion in flowing blood. As a result, the signal attenuation with respect to b-values resembles a double exponential curve and information about perfusion levels of the tissue can be derived from the method. The application of IVIM to the MWC model was explored in the dissertation work of Rachel Schafer [26], a former graduate student of Prof. Gmitro. The discussion of perfusion imaging in this dissertation is focused on DCE MRI and ASL methods.

9.5.2 Qualitative perfusion imaging with DCE MRI

DCE MRI requires the injection of a paramagnetic MR contrast agent that has a low molecular weight and is capable of providing contrast through the modification of T1 relaxation of nearby tissue components. The most common MR contrast agents are gadolinium-based (Gd). Gd^{3+} ions in the contrast agent are strongly paramagnetic and produce an oscillating magnetic field as the molecule tumbles and interacts with water protons. This facilitates the energy transfer between the Gd^{3+} ions and nearby water protons. The resultant shortened T1 of the water protons provides the contrast seen in DCE MR images. By obtaining a series of T1-weighted images before, during and after the injection of the contrast agent, the signal changes that occur provide qualitative visualization of the delivery and washout of the agent in the tissue. Quantitative measurements of perfusion requires

additional information such as the arterial input function (AIF), T1 maps and modelling of the pharmacokinetics of the agent. The main challenge of quantitative DCE MRI is obtaining accurate estimation of the AIF, which is defined as a measure of the time-dependent concentration input to the tissue [138]. Nevertheless, even without AIF, the calculation of various temporal signal parameters to capture characteristics of the enhancement-washout patterns from DCE MRI can be useful for evaluating perfusion or for sub-typing tumors [139].

The experimental results of DCE MRI of a MCF-7 breast cancer xenograft in the mouse MWC model are now presented. A MCF-7 tumor was imaged on day 10 after tumor cell innoculation. A commercial Gd[DTPA-BMA] (Omniscan) MR contrast agent, diluted 10:1 was used for the DCE MRI experiment. A tail vein catheter was placed in the animal before it was positioned in the MR scanner. Next, 15 sequential 1mm thick axial T1-weighted images of the tumor were obtained to visualize the tumor. A suitable slice location for DCE MRI was selected from the series of anatomical images. The T1-weighted anatomical image of the tumor that corresponds to that slice location is shown in Figure 9.10(a). It should be noted that the FOV of the DCE MRI was shifted slightly to the right with respect to the anatomical image to have a more central view of the tumor.

After selecting the desired axial slice location, the DCE MRI sequence, with the key parameters listed in Table 9.3, was started. Approximately 50s of baseline imaging data were acquired before 200μl of the diluted contrast agent was injected over a time period of approximately a minute. The entire duration of the scan was approximately 16 minutes.

Table 9.3: DCE MRI experimental parameters

Parameters	Values
TR (ms)	40
TE (ms)	4.4
Excitation flip angle (degrees)	20
Number of images	186
Imaging duration (min.)	15.9
Fat suppression	Yes
Slice thickness (mm)	1
Pixel size (μm)	200×200
Image matrix size (μm)	128×128
FOV (mm)	25.6

Figure 9.10(b) shows an image from the DCE MRI scan that was taken before the injection of the contrast agent. Figure 9.10(c)-(i) are representative images obtained at different time points during the DCE MRI scan. From these images, one can appreciate that there were different uptake rates of the contrast agent at different locations. From Figure 9.10(i), it appears that there were two distinct sections of the tumor that had different uptake of the contrast agent. The most rapid initial enhancement of signal occurred at the pheriphery of those two sections and this is most clearly illustrated in Figure 9.10(d)-(f). Subsequently, there was continuously increasing enhancement in the left section of the tumor. On the other hand, there was a gradual wash out of signals on the right section of the tumor.
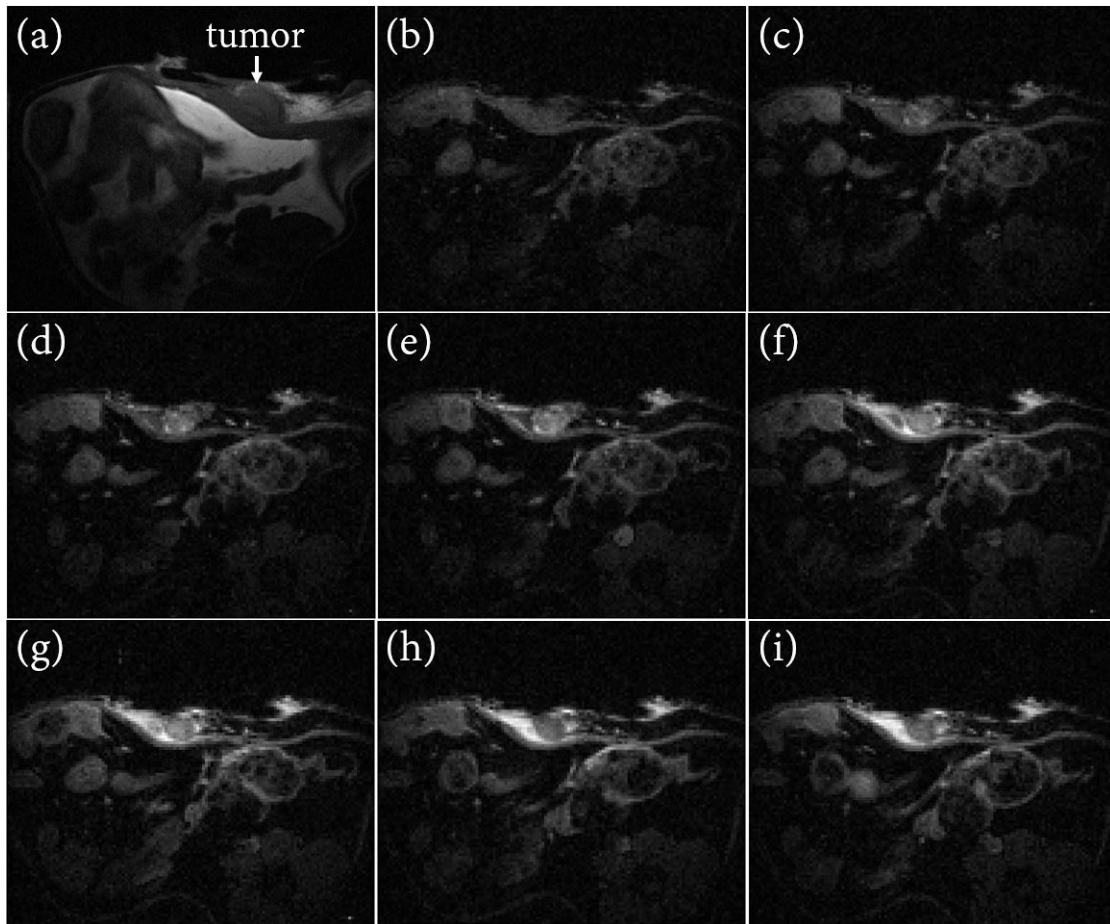
Figure 9.10: Raw images of DCE MRI. (a) T1-weighted image of the axial slice which DCE MRI was performed on. (b) Raw MR image of the tumor before injection of contrast agent. (c)-(i) Raw images of the tumor taken at different time points after injection of contrast agent.

The plots of the temporal signal variation at three different locations on the tumor, ROIs 1-3, are shown in Figure 9.11. The plots at those locations illustrate three distinct characteristic enhancement-washout patterns often observed in tissue [140]. In ROI 1, there was rapid enhancement with plateauing of signal. In ROI 2, the tissue exhibited progressive enhancement of signal at a slower rate as compared to ROI 1. In ROI 3, there was rapid enhancement followed by a rapid washout of signal. This particular type of heterogeneous pattern of enhancement in the clinical setting raises a red flag as it is often observed in pathological tissues with poor clinical outcomes. The rapid uptake suggests a high level of angiogenesis and the

rapid washout rate implies that the vascular system is highly permeable. These characteristics are often associated with malignancy.

Although the enhancement patterns most frequently encountered can be broadly categorized into one of the three patterns as described above, it is difficult to identify the exact physiological factors that are responsible for a certain pattern. Generally, high vascular density and high vascular permeability would lead to a rapid signal enhancement. Poorly developed and shunted vascular system would impede the delivery of agent to the extravascular tissue spaces and result in a reduced and slower signal enhancement. Tissue that is not supported by a viable vascular system tend to exhibit slower enhancement. Nevertheless, the slow diffusion of contrast agent from neighboring regions could result in a gradual signal enhancement. Tissue with high cell density and disorganization allows the extravasated contrast agent to pool in the tissue for longer periods of time, which can explain the plateauing of the signals observed in ROI 1.
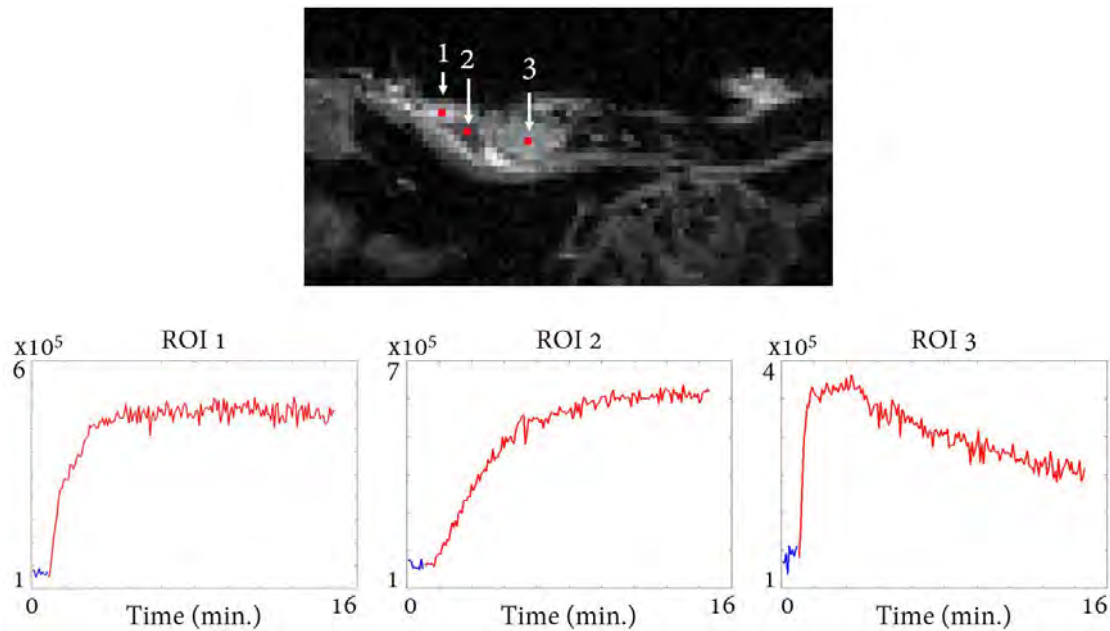
Figure 9.11: DCE MRI analysis. Top image shows the locations of ROIs 1-3 in the tumor. Bottom row are plots of the dynamic signal variation that occured in ROIs 1-3. Three distinct types patterns were observed. In ROI 1, there was rapid enhancement with plateauing of signals. In ROI 2, there was progressive enhancement of signals. In ROI 3, there was rapid enhancement followed by a rapid wash out of signals. Baseline signals acquired before the injection of the MR contrast agent are shown in blue, while the signals acquired after injection are shown in red.

Another example of a DCE experiment is presented here. The experimental protocols are the same as above, except that the animal was implanted with a MDA-MB-231 tumor. The raw DCE MR images taken before injection of the contrast agent, within a minute after injection, and 15 minutes after injection are shown in Figures 9.12(a), (b) and (c), respectively. Similar to the example given above, there was rapid signal enhancement at the periphery of the tumor (Figure 9.12(b)). This was followed by a gradual signal enhancement in the inner portions of the tumor (Figure 9.12(c)). In addition, the plots of the temporal signal variation at three different locations on the tumor, ROIs 1-3, are shown in Figure 9.11. The three characteristic enhancement patterns were observed at different locations within the tumor. However, it is noted that the signal enhancement was approximately an order of magnitude smaller than the previous example. Furthermore, in contrast to

the example shown in Figure 9.11(c), ROI 1 exhibited a more rapid washout pattern whereby its signal levels were almost back to the baseline level within 16 minutes of imaging period.
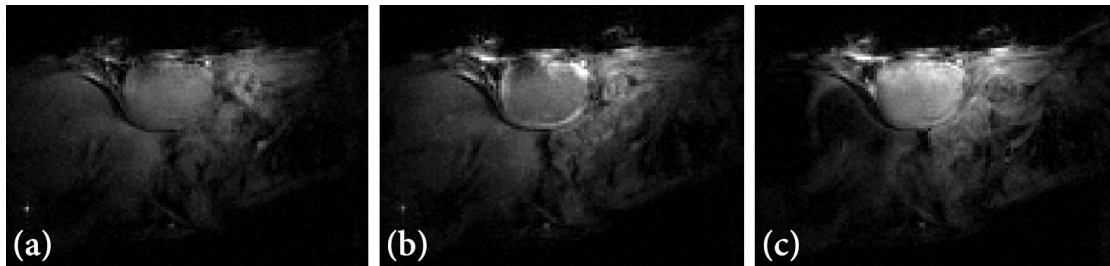
Figure 9.12: Raw DCE MRI images of a MDA-MB-231 tumor (a) before injection of contrast agent, (b) within a minute after injection, and (c) 15 minutes after injection. A distinct enhancement at the periphery of the tumor was observed during the early imaging time point (b) and this was followed by a gradual increase in enhancement in the inner portion of the tumor tissue (c).
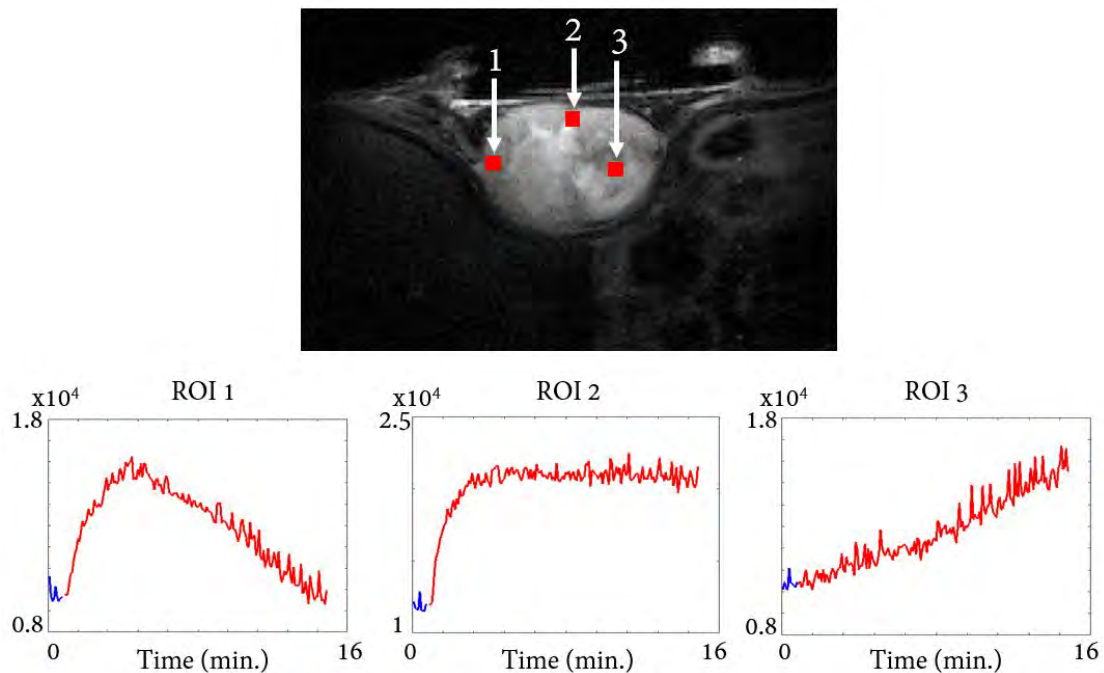
Figure 9.13: The top image shows a T2-weighted axial MR image of the tumor and the locations of ROIs 1-3. The bottom panel shows plots of temporal signal variation at the three ROIs. Baseline signals acquired before the injection of the MR contrast agent are shown in blue, while the signals acquired after injection are shown in red.

In summary, DCE MRI was successfully applied to the MWC mouse model. The method requires the injection of a paramagnetic contrast agent (Omniscan) to provide dynamically changing T1-contrast. The temporal signal changes in the images allow the qualitative visualization of perfusion in the tumor. Additional estimation of AIF and modelling of the pharmokinetics is necessary for quantitative measurements of perfusion to be made with DCE MRI.

9.5.3   Perfusion imaging with an arterial spin labelling (ASL) technique

Due to the challenges of quantitative DCE MRI, an alternative method based on a type of ASL technique was explored. In contrast to DCE MRI, the ASL approach does not require exogeneous contrast agent. Instead, it relies on the inversion of magnetization of water protons in the arterial blood to create endogeneous tracer, which is used to provide quantitative measurements of tissue perfusion.

ASL techniques are predominantly used to study perfusion of the brain [141]. Nevertheless, applications of the technique to the study of other organs have also been demonstrated [116, 142, 143]. In this dissertation work, a type of ASL technique, known as Flow-sensitive Alternating Inversion Recovery (FAIR) combined with the RARE readout sequence, was explored to evaluate its utility in quantifying perfusion of breast cancer xenografts in the MWC mouse model. A brief description of the FAIR sequence is given in this section and greater details can be found in [144–146].

With reference to Figure 9.14, the perfusion imaging with the FAIR pulse sequence requires the acquisition of a series of interleaved selective control images and non-selective tagged images. For the acquisition of selective images, a 180° pulse is applied as a slice selective gradient is applied. This inverts the magnetization of protons in the inversion slice location of the tissue. There is time delay between the time of application of the 180° pulse and the time of image readout (inversion time, TI) to allow perfusion and T1 relaxation of the inverted magnetic spins. After that, an imaging sequence is applied after the inversion time delay to obtain signals from a slice location in the tissue. The signals in the imaging slice depends on the

T1 relaxation and outflow of inverted protons from the inversion slice, and in the inflow of untagged protons. The imaging slice and the inversion slice are centered about the same position. The inversion slice is typically slightly thicker than the imaging slice, to ensure that the inversion pulse within the imaging slice is uniform. The imaging of a non-selective tagged image utilizes a similar pulse sequence, except that the 180° pulse is applied without a slice selective gradient. As a consequence, a global inversion is achieved. The process is repeated a number of times with varying inversion times TI.
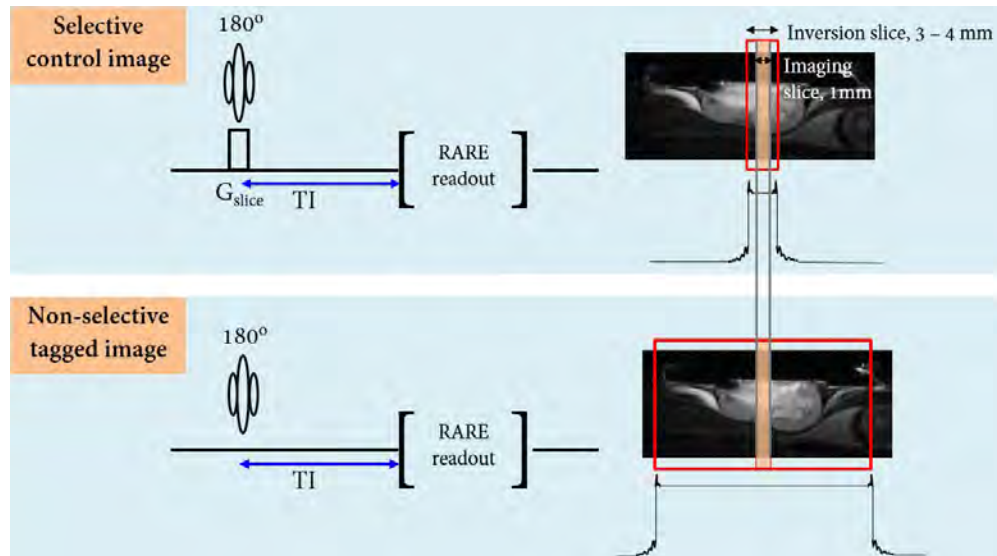
Figure 9.14: A schematic illustrating the FAIR-RARE MRI pulse sequence used for quantitative perfusion imaging. 22 interleaved selective control images (top) and non-selective tagged images (bottom) were obtained with the use of 22 different TIs that range from 30-2300ms.

The series of selective and non-selective images allows the computation of perfusion, based on the following equation:

$$\frac{1}{T_{1,\text{app}}} = \frac{1}{T_1} + \frac{f}{\lambda}, \tag{9.6}$$

where $T_{1,\text{app}}$ is the apparent T1 that combines the effect of intrinsic T1 relaxation and signal change due to the flow process, f is perfusion, and λ is the tissue-blood partition coefficient, which is defined as

$$\lambda = \frac{[\text{g of water per g of tissue}]}{[\text{g of water per g of blood}]}. \qquad (9.7)$$

There are numerous other well-established ASL techniques that have been developed. Some of them require inversion at the proximal end of the blood flow and imaging on the distal end. Those kinds of techniques work on the assumption that blood flow is unidirectional and they would not work well if that assumption is not valid. In tissue such as tumor where the vascular network is often tortuous, the global inversion technique employed by the FAIR-RARE MRI sequence provides the advantage of being able to more accurately measure perfusion in cases when blood flows in both directions aross the imaging slice.

In the following section, experimental data with FAIR-RARE are presented. Typical values of key imaging parameters used during FAIR-RARE MRI of the MWC are given in Table 9.4.

Table 9.4: FAIR-RARE MRI experimental parameters

Parameters	Values
Inversion slice thickness (mm)	4
Imaging slice thickness (mm)	1-2
Inversion slice margin (mm)	1-1.5
RARE factor	36
Image matrix size	64×64
Pixel size (μm)	400×400
Number of different TIs	22
Range of TI (ms)	30 - 2300
Recovery time (s)	10
Scan duration (min.)	8.5
Fat suppression	On

The choices of imaging parameters, such as inversion slice thickness and inversion slice margin, affect the accuracy of perfusion results. Referring to Figure 9.14, there are inevitable imperfections in inversion slice selection profiles, especially on the extreme sides of the selected slice. As a result, there is non-uniformity in the inversion of protons within the slice. The slice will consist of fully and partially inverted protons, which are not accounted for in the mathematical model used to

calculate perfusion results. Therefore, accuracy can be improved by using signals in a thinner imaging slice within the inversion profile where the inversion profile is more uniform. However, the use of a large slab margin introduces inaccuracies as well, because the perfusion of protons within the slab margin is not properly accounted for in the post-processing of selective and non-selective images. Thus, a balance has to be struck between imaging in the uniformly inverted slice and avoiding inaccuracies due to the perfusion of protons in the slab margin. In view of those considerations, perfusion imaging with different slice and margin parameters was tested. However, because there is no gold standard to compare the FAIR-RARE perfusion imaging results against, the exact effects of the selection of different parameters was difficult to access.

Figure 9.15 shows an example of perfusion imaging of a MDA-MB-231 tumor with FAIR-RARE. In this case, a 5mm inversion slice and 2mm imaging slice were used. Figure 9.15(a) is a T2-weighted axial MR image of the tumor at the same location. Figure 9.15(b) shows the measured perfusion map superimposed on the anatomical image. The result shows that the perfusion values of the surrounding tissue are higher than those within the tumor tissue. This result suggests that there is a higher rate of delivery of blood per unit mass of surrounding tissue, as compared to the tumor tissue. This is consistent with what was observed from the DCE MRI experiment performed on this animal (Figure 9.12). The presence of rapid enhancement of DCE signals around the periphery of the tumor but not in the inner portion of the tumor tissue suggests that there is a higher density of vasculature outside and at the periphery of the tumor.

Figure 9.15: (a) A T2-weighted axial image of the tumor. (b) The perfusion map superimposed on the anatomical image. A 5mm inversion slice and 2mm imaging slice were used.

Figure 9.16 shows the results of perfusion imaging on another animal with a MDA-MB-231 tumor. This time, a 4mm inversion slice and 2mm imaging slice were used. The 1mm slab margin used here is slightly smaller than the 1.5mm slab margin used in the previous example. Figure 9.16(a) shows a T2-weighted anatomical image that corresponds to the perfusion map. The bright region within the tumor suggests onsest of necrosis. The perfusion map depicted Figure 9.17(b) shows that the perfusion within the tumor is significantly lower than surrounding tissue. Poor perfusion of the tumor often leads to deprivation of blood and nutrients, which can then lead to tissue death.

Figure 9.16: (a) A T2-weighted axial image of the tumor. (b) The perfusion map superimposed on the anatomical image. A 4mm inversion slice and 2mm imaging slice were used.

As a final example, Figure 9.17 shows the results of perfusion imaging on an animal implanted with a MCF-7 tumor. A 4mm inversion slice and 2mm imaging slice were used in this experiment. Figure 9.17(a) shows a T1-weighted anatomical

image of the tumor (indicated by an arrow pointing to a dark region) and it resides in a layer of fatty tissue. The size of the tumor is small in this case. Figure 9.17(b) shows the corresponding perfusion map. As indicated by arrows on the images, the the perfusion value in the MCF-7 tumor tissue is higher than the other parts of the tumor. This is in contrast to the other examples where perfusion in those MDA-MB-231 tumors are lower than surrounding tissue.
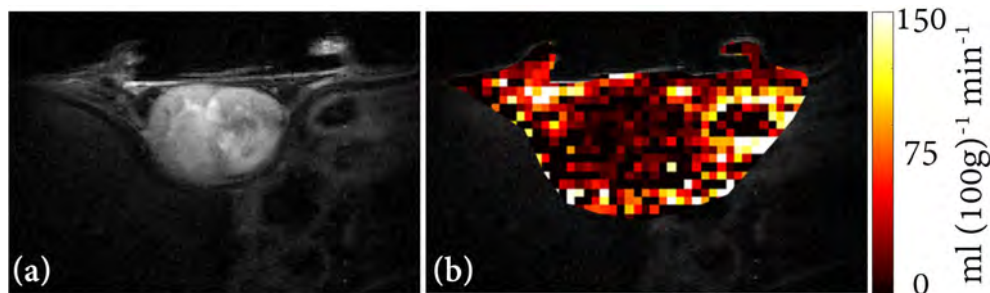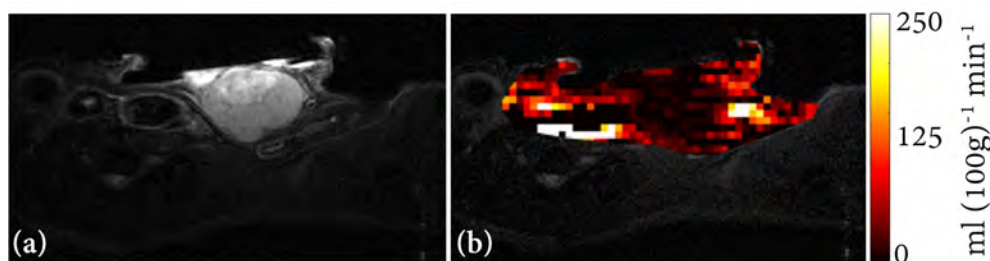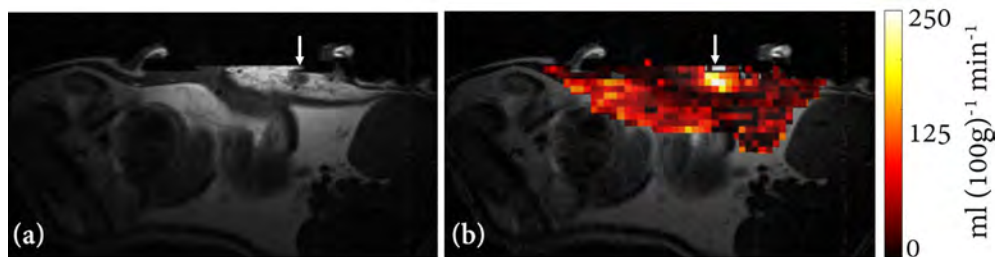

Figure 9.17: (a) A T1-weighted axial image of the tumor. (b) The perfusion map superimposed on the anatomical image. A 4mm inversion slice and 2mm imaging slice were used.

CHAPTER 10

Multimodal Imaging of PDX in the MWC Murine Model

10.1   Overview of PDX

The advantage of using WC animal models as pre-clinical research tools for cancer studies is the ability to leverage unique capabilities of various imaging modalities to non-invasively study a dynamically evolving tumor within a natural biological system. The imaging tools that were developed in this dissertation work can be useful for numerous purposes such as verifying response to treatment, evaluation of treatment strategies and understanding of mechanisms behind various behaviors of tumors. The ultimate goal is to obtain useful knowledge about the disease that is translatable into the clinic and benefits patients. Apart from developing imaging techniques to study tumors, another crucial aspect of the work involves having an animal model that can recapitulate the characteristics and response patterns of human cancer. Because of selecive pressures that laboratory cultured cancer cells are subjected to, the heterogeneity and behavior of tumors in human patients are often not well represented in tumor xenografts grown from cell lines.

One of the ways to improve the clinical translational power of the MWC mouse model for breast cancer research is to use patient derived xenografts (PDX) [147]. The preparation of PDX animals, previously described in Section 2.1.2, initially involves the use of tissue samples obtained from patient biopsies. The biopsied tumor tissue is implanted and allowed to proliferate in an NSG mouse until a larger size tumor tissue is grown. That larger tumor tissue can then be extracted, frozen and be available for use in future animal studies. Because the xenograft preparation process involves minimal exposure of the tissue to artifical settings such as passaging of the cells in the laboratory, it is presumed that the PDX tumor retains its original phenotypical behavior better than cultured cancer cells.

Through a collaboration with Dr Ghassan Mouneimne of the University of Arizona and availability of PDX tissue initially obtained from the University of Utah, work was done to incorporate this breast cancer PDX into the orthotopic MWC murine model. In the following sections, *in vivo* imaging of the PDX was demonstrated with various imaging capabilities described in the earlier chapters. By demonstrating the capability of studying various aspects of the PDX in the MWC murine model, a pre-clinical animal model with strong clinical translational power was achieved.

10.2   Experimental results with MRI

10.2.1   Anatomical MRI

In the earlier chapters of this dissertation, xenografts were grown from GFP tranduced cancer cells. Tumor tissue could be easily delineated from surrounding tissue with the use of fluorecence imaging. However, the PDX tissue is not transduced to express fluorescent proteins. As a result, anatomical MRI of the tumor had to performed to determine the position of the tumor within the MWC. A few examples of T2-weighted anatomical images of PDX tumors are given in this section.

Figures 10.1 and 10.2 show examples of T2-weighted MR images of axial slices across PDX tumors in two different animals. The axial slices are 1mm thick with $100 \times 100 \mu$m pixel size. Figure 10.3 is an example of T2-weighted MR images of 0.5mm thick coronal slices across a PDX tumors. Similarly, in-plane pixel size of those images is $100 \times 100 \mu$m .

The axial images show the presence of voids within the tumors. These types of structures were not observed in xenografts grown from cultured cells. The heterogeneous structure of the tumor is especially remarkable in the images shown in Figure 10.2.
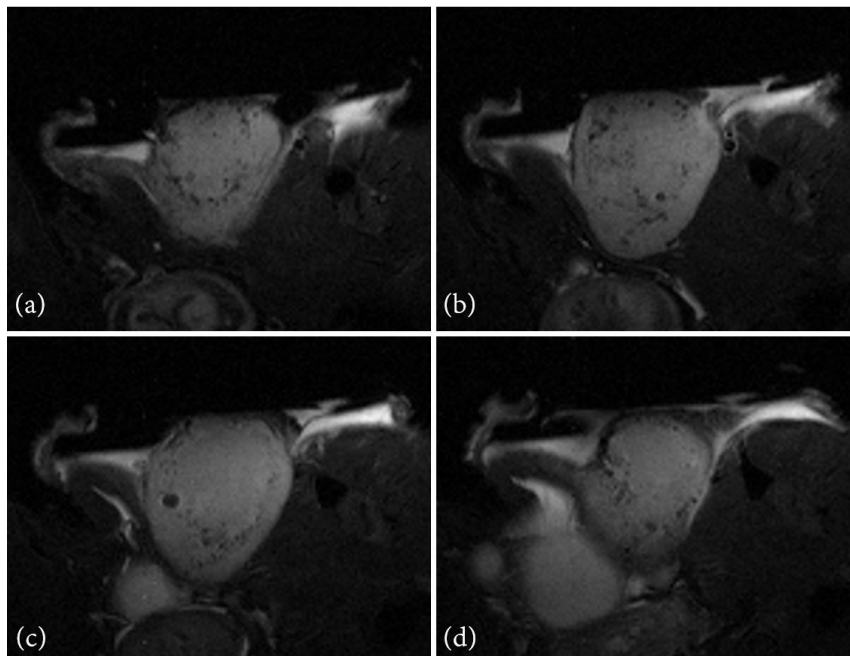
Figure 10.1: T2-weighted axial MR images of a PDX tumor. Four serial axial slices are shown in (a)-(d).
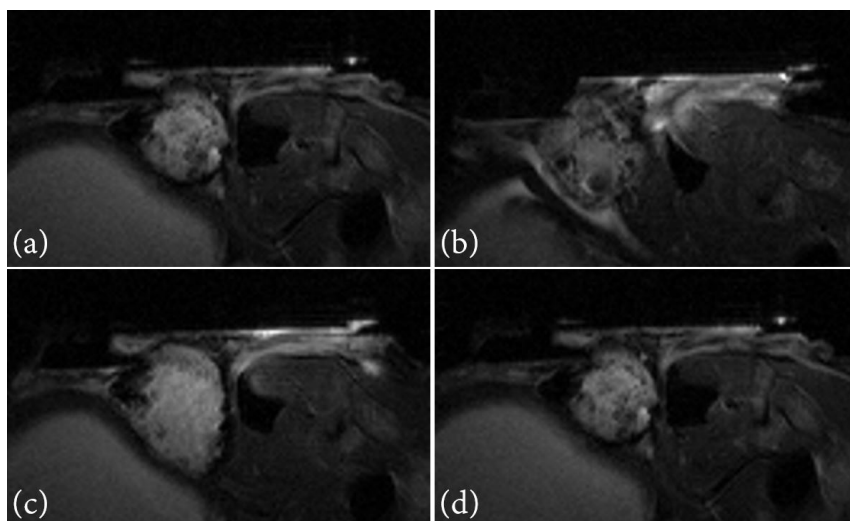
Figure 10.2: T2-weighted axial MR images of a PDX tumor. Four serial axial slices are shown in (a)-(d).
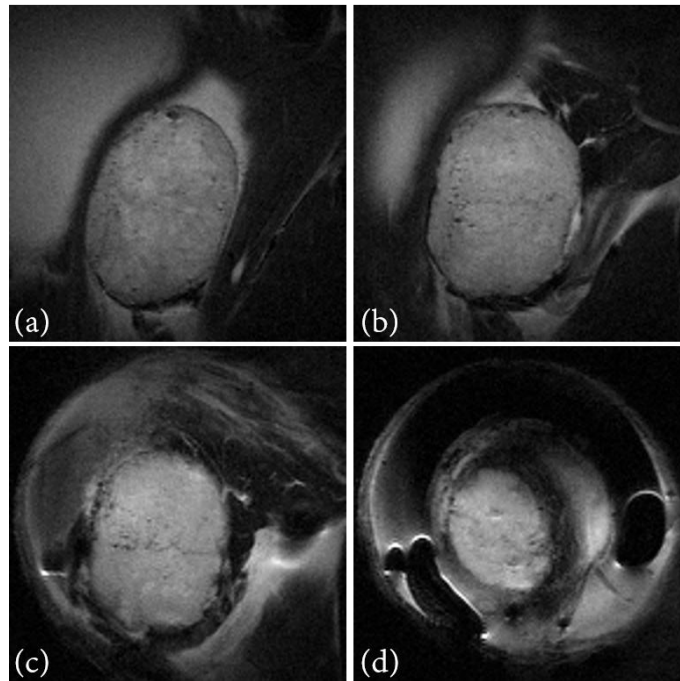
Figure 10.3: T2-weighted coronal MR images of a PDX tumor. Four serial axial slices from bottom up are shown in (a)-(d).

10.2.2   DWI

DWI of a PDX tumor was performed using a 2mm thick coronal slice in a MWC animal. DWI in 3 orthogonal directions was performed with three different b-values (b=0, 300, and 600 s mm^2). A T2-weighted image of the tumor that corresponds to the location where DW MRI was performed is shown in Figure 10.4. The ADC maps of the tissue in x-, y-, and z-directions are shown in Figures 10.5(a)-(c). The root mean square of the ADC values in the three directions was computed and the resultant ADC map is shown in Figure 10.5(d).

The ADC values of the tumor are visibly lower than those of the surrounding tissue, especially at the edge of the tumor. The mobility of water in the tumor tissue appears to be isotropic, while that of surrounding tissue is not. The surrounding tissue has higher ADC values in the x-direction (mobility of water diffusion is less restricted), as compared to y- and z-directions. This could be because of the presence of more organized tissue structures that are aligned along the x-direction in those

areas.
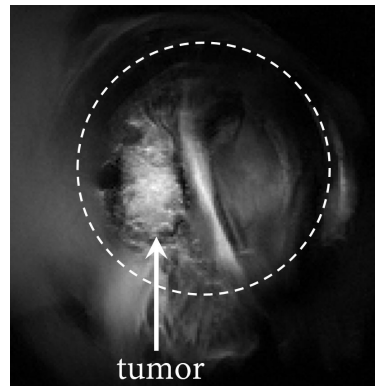
Figure 10.4: A T2-weighted coronal MR image of the PDX tumor (indicated with an arrow). Dashed circle indicates the boundary of the MWC.
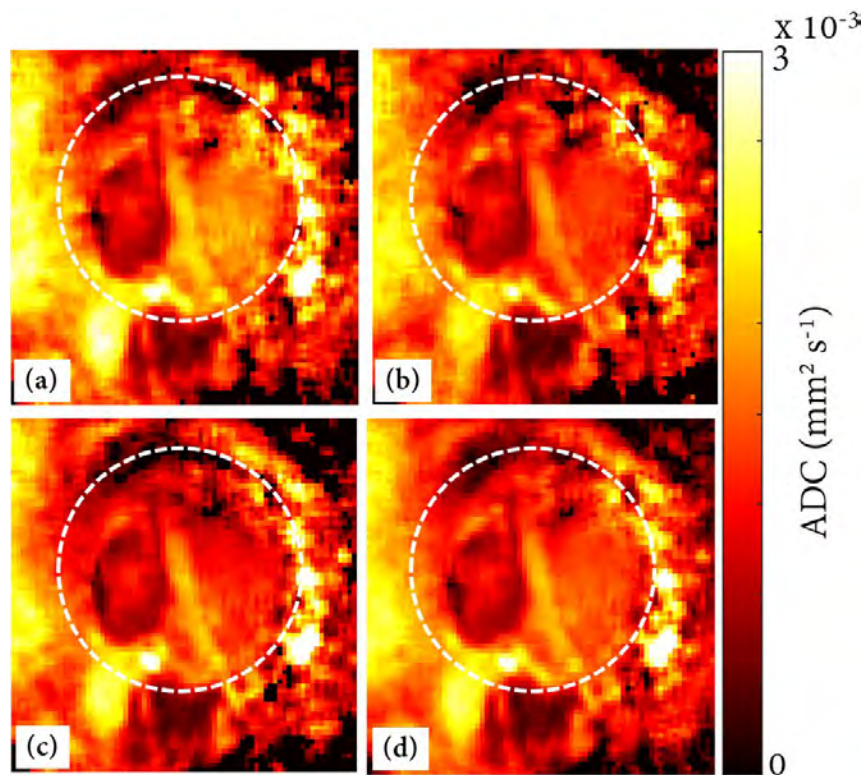
Figure 10.5: Results of ADC imaging in the coronal plane. (a)-(c) show ADC maps in the x-, y- and z-directions. (d) A map of the root mean square of the ADC values in the three orthogonal directions. Dashed circle in each image indicates the boundary of the MWC.

10.2.3   Perfusion imaging with DCE MRI

A DCE MRI experiment was performed on a PDX animal on day 41 after tumor tissue implantation. A tail vein catheter with a 59cm long infusion line was placed in the animal before it was positioned in the MR scanner. DCE MRI was performed on a 2mm thick axial tissue slice and the T2-weighted anatomical image at that location is shown in Figure 10.6. Other key parameters of the DCE MRI sequence are similar to those listed in Table 9.3. A diluted solution of Omniscan, a Gd-based MR contrast agent, was used in this DCE MRI experiment (refer to Section 9.5.2). Approximately 45s of baseline imaging data were acquired before 200μl of the diluted contrast agent was injected over a time period of approximately a minute. Over a period of 30s, an additional volume of saline, equivalent to the dead volume in the infusion line, was then used to slowly flush the infusion line to ensure full delivery of the contrast agent. The entire duration of the MRI scan was approximately 16 minutes.
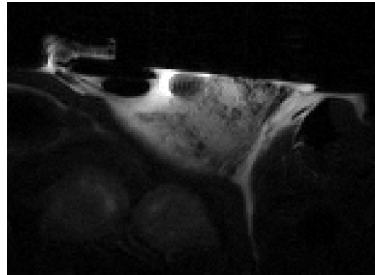
Figure 10.6: T2-weighted axial MR image of the PDX tumor, where DCE imaging was performed.

The time dynamics of the signal variation at various 3x3 pixel ROIs in the tissue are shown in Figure 10.7, with the locations of the ROIs indicated on inset images. Figures 10.7(a)-(c) show rapid signal enhancements, which was followed by plateauing of the signal. The temporal gradients of the initial enhancement curve were different in these three cases, from the slowest in (a) to the fastest in (c). Figure 10.7(d) shows a progressive enhancement of signal throughout the imaging period. Figures 10.7(e)-(f) show rapid signal enhancement followed by a

continuous washout of signal. Figures 10.7(a)-(f) are examples of the three distinct characteristic enhancement-washout patterns that were discussed in Section 9.5.2. In addition, Figures 10.7(g)-(i) show a fourth enhancement-washout pattern that was observed in the PDX tumor of this animal. In Figures 10.7(g) and (h), there were rapid signal enhancement, which were quickly followed by a rapid decrease in signal intensity. Subsequently, there was progressive enhancement thoughout the later part of the imaging period. The first signal maxima occurred approximately at the time when the injection of the contrast agent ended, while the post-injection minima occurred approximately 1.5 minutes afterwards. Figure 10.7(i) shows a similar pattern but with significantly higher signal levels. The first signal maxima and post-injection minima occurred at approximately 1.8 and 5 minutes after the start of the injection. The exact mechanisms behind this temporal variation pattern is yet to be determined.
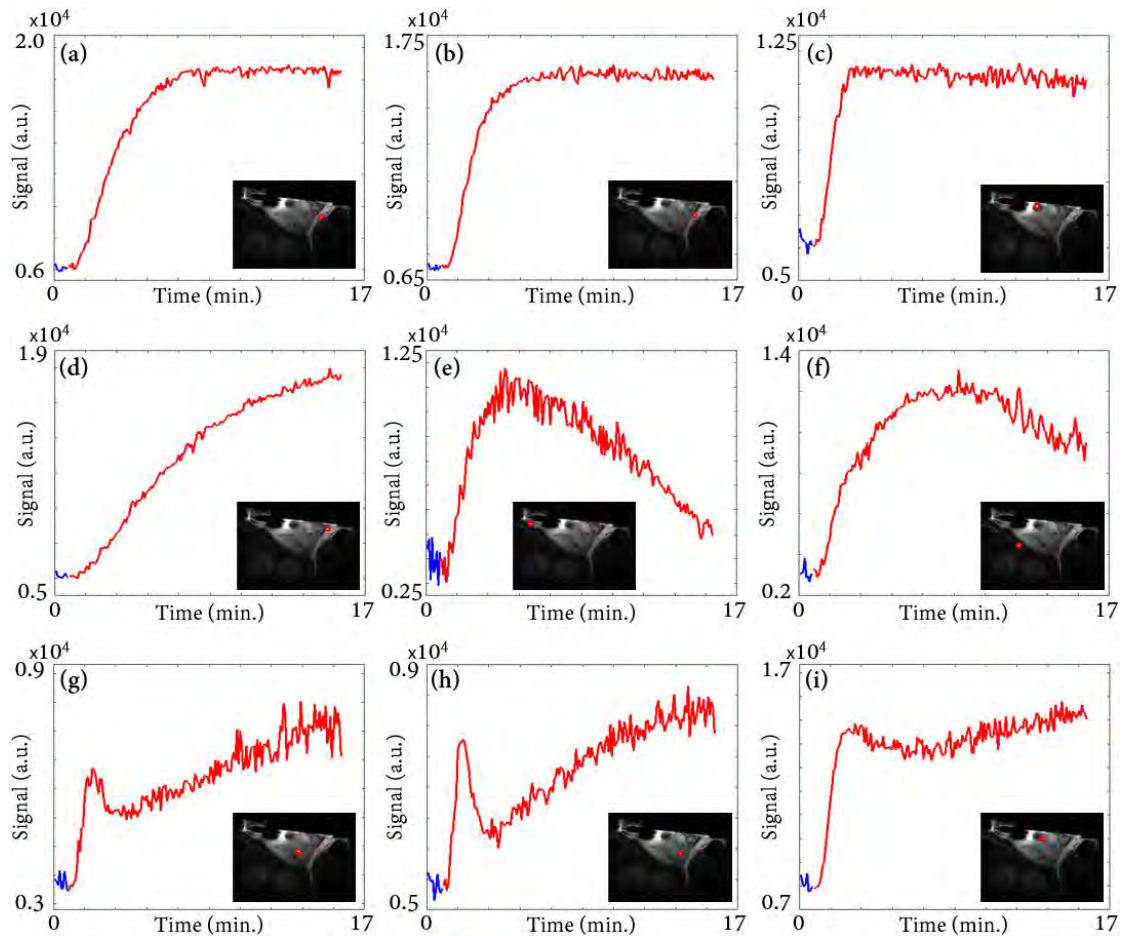
Figure 10.7: Results of DCE imaging of a PDX tumor in the axial plane. Baseline signals acquired before the injection of the MR contrast agent are shown in blue, while the signals acquired after injection are shown in red. The locations of the 3x3 pixel ROIs associated with each graph are indicated by red boxes drawn on the inset anatomical MR images.

10.2.4   Perfusion imaging with FAIR-RARE

This section presents an example of using the FAIR-RARE MRI sequence to measure perfusion in a PDX tumor. The imaging and inversion slice thickness were chosen to be 1mm and 3mm, respectively. The other imaging parameters follow what was listed in Table 9.4. Figure 10.8(a) shows a T2-weighted axial MR image of the PDX, which corresponds to the location where perfusion imaging was performed. The perfusion map, averaged with a 5×5 pixel kernal, is superimposed on the anatomical

image and is shown in Figure 10.8(b). The black pixels indicate regions where zero and/or non-physical perfusion values were obtained, which is due to low signal levels obtained in those regions.

The T2-weighted anatomical image indicates that onset of necrosis has occured in the region where signal levels are higher as compared to other parts of the tumor. There are regions within the tumor where there were low perfusion values and a portion of those regions overlap with the necrotic part of the tumor. Two regions, the bottom left and right side of the tumor, have significantly higher levels of perfusion.
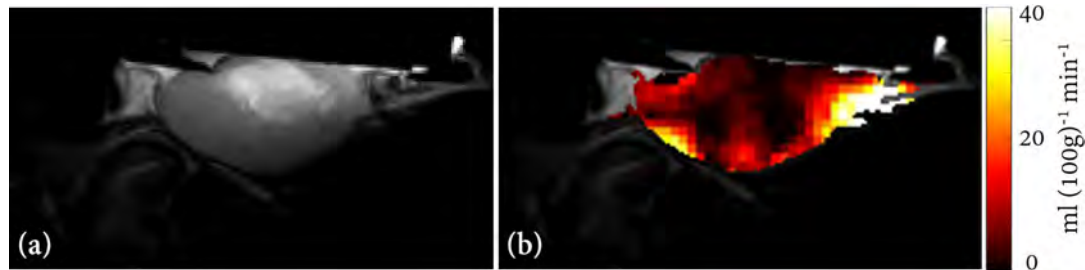
Figure 10.8: Results of anatomical and perfusion imaging of PDX in the axial plane. (a) T2-weighted axial MR image of the PDX tumor. (b) The perfusion map, acquired with the FAIR-RARE technique, is superimposed onto the anatomical image.

10.3 Experimental results with optical imaging

This section presents optical imaging results of the PDX tumor. They include the use of broadband reflectance spectral imaging to monitor changes in SaO_2 in the MWC over days, high resolution fluorescence microscopy of tumor cells and vascular network, and whitelight microscopy of the PDX tumor tissue.

10.3.1 SaO_2 imaging with broadband reflectance spectral imaging

In this section, the tissue oxygenation changes of a PDX tumor were monitored over days with the use of reflectance spectral imaging. Thirty days after the tumor PDX tissue was orthotopically implanted in a NSG mouse, it grew to 101.8 mm^3. A MWC was then implanted on the mouse before imaging experiments were carried out. On days 38, 42, and 43 after PDX tissue implantation, reflectance spectral imaging was

performed to obtain SaO_2 maps of the tumor and the results are shown in Figures 10.9(a)-(c), respectively. The corresponding coronal MR image of the tumor taken on day 41 after PDX tissue implantation is shown in Figure 10.10.
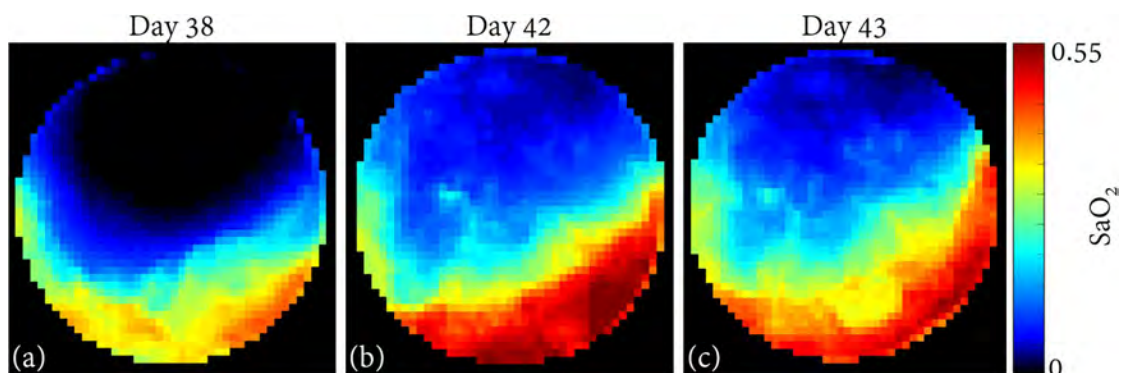
Figure 10.9: SaO_2 maps of the PDX tumor on day 38, 42, and 43 after PDX tissue implantation.
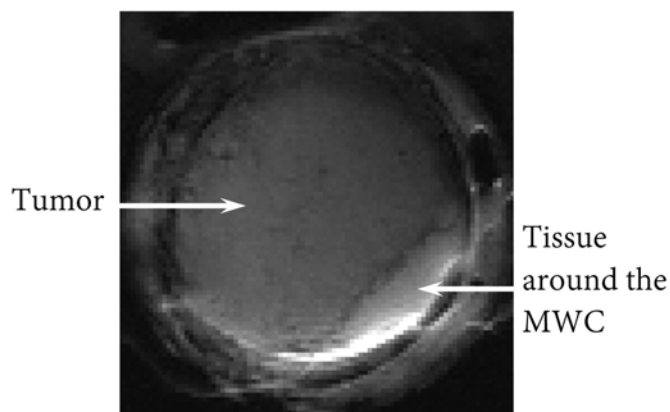
Figure 10.10: Coronal MR image of the PDX on day 41 after tissue implantation.

Comparing the SaO_2 maps with the MR image of the tumor, it can be observed that the tumor exhibited significantly lower SaO_2 values than the surrounding tissue. The tumor on day 38 (Figure 10.9(c)) was very hypoxic but the SaO_2 values of the tumor increased gradually over days. One possible explanation for the increase in SaO_2 from day 38 to day 43 is the development of new vascular network around the hypoxic tumor, which helped increase the delivery of well-oxygenated blood to

that part of the tissue. Fluorescence imaging of the vascular network in the MWC is later described in Section 10.3.3.

In addition, there was a gradient of high to low SaO_2 values at the boundary between tumor and surrounding tissue. This is most clearly illustrated in Figure 10.9(c) where striated levels of SaO_2 was observed.

10.3.2   High resolution confocal microscopy of tumor cells

The transparent glass coverslip of the MWC allows high-resolution microscopic imaging of the PDX tumor. Experimental results of high-resolution fluorescence confocal microscopic imaging of tumor tissue cells in the MWC is presented in this section. Positive staining of the nuclei of PDX tissue cells was achieved by topical administration of approximately $5\mu l$ of $330\mu M$ acridin orange (excitation/emission = 488/510) to the tissue, after removing the glass coverslip of the MWC. After approximately a minute, excess acridine orange was rinsed away with PBS and the glass coverslip of the MWC was put back in place. Since the position of the tumor within the MWC can be easily visualized, the FOV of the microscope was set in a region in the tumor. A high quality 40X objective (Nikon S Plan Fluor, ELWD, NA=0.6) on a confocal fluorescent microscope was used to image the fluorescently stained nuclei of the tumor cells. A series of fluorescence images were collected at different focal planes in the tissue, through motorized control of the microscope stage. In steps of $2\mu m$, multiple fluorescence images through a $40\mu m$ tissue section were obtained. Maximum intensity projection of the images was done through the confocal microscope software and the result is shown in Figure 10.11.
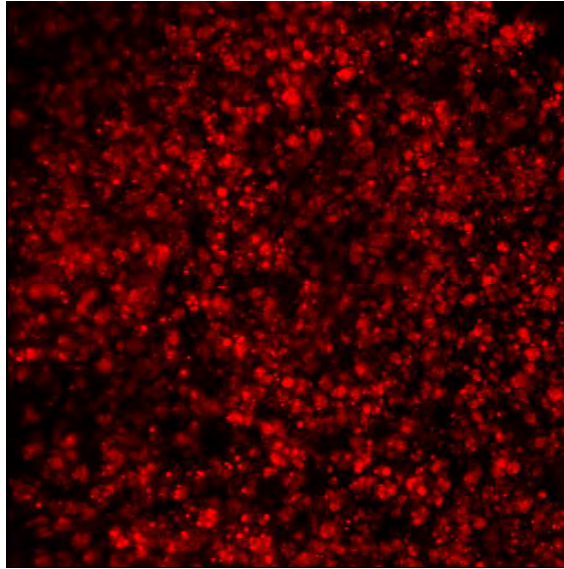
Figure 10.11: A maximum intensity projection of fluorescence images obtained through a 40μm tissue section. The positively stained nuclei of PDX tumor cells can be readily observed in this image.

10.3.3 High resolution confocal microscopy of a vascular network

This section presents experimental results of the visualization of a vascular network in the PDX tumor tissue using confocal microscopy. The contrast agent being used to accomplish this was a fluorescently-labeled bovine serum albumin (BSA) (A34785, Life Technologies). BSA has an approximate molecular weight of 66 kDa. Due to its large molecular weight, it does not leak out readily and is able to stay mostly intravascular for approximately 30-60 minutes. The BSA used in this experiment was conjugated with Alexa Fluor 647 with peak excitation/emission wavelengths at 650/668nm. The injected agent was composed of 1mg of lyophilized powder of Alexa Fluor 647-BSA dissolved in 200μl of PBS.

A tail vein catheter was placed on the animal. The MWC was then focused on the microscope using white-light epi-illumination and a 2X objective lens. Figure 10.12(a) shows a white-light image of the MWC taken with the 2X objective. Upon visual inspection, the tumor was determined to be located in the top half of the MWC. The approximate location of the tumor is outlined in Figure 10.12(a). After

focusing the MWC, imaging was switched to the confocal scanning mode, but with an open pinhole (150μm). With reference to the diagram of the microscope shown in Figure 3.4, a 632.8nm laser was used to excite the contrast agent and emission signal was collected in spectral channel 2 (640nm LP filtered). The gain was set to 95 on that spectral channel and a dwell time of 1.92μs per pixel was used. Starting shortly before the bolus IV injection of the contrast agent, a set of 50 fluorescence images of the MWC was obtained serially over a time period of approximately 25s. Representative fluorescence images taken before and after the injection are shown in Figure 10.12. The fluorescence images of the MWC after the injection of the contrast agent clearly show the vascular network that was present in the tissue. It was observed that comparatively larger vessels had developed in the tumor tissue, and these larger vessels can also be visualized in the white light image of the MWC. It should be noted that the FOV of the white-light image and fluorescence images are slightly different due to difference in the imaging configuration.
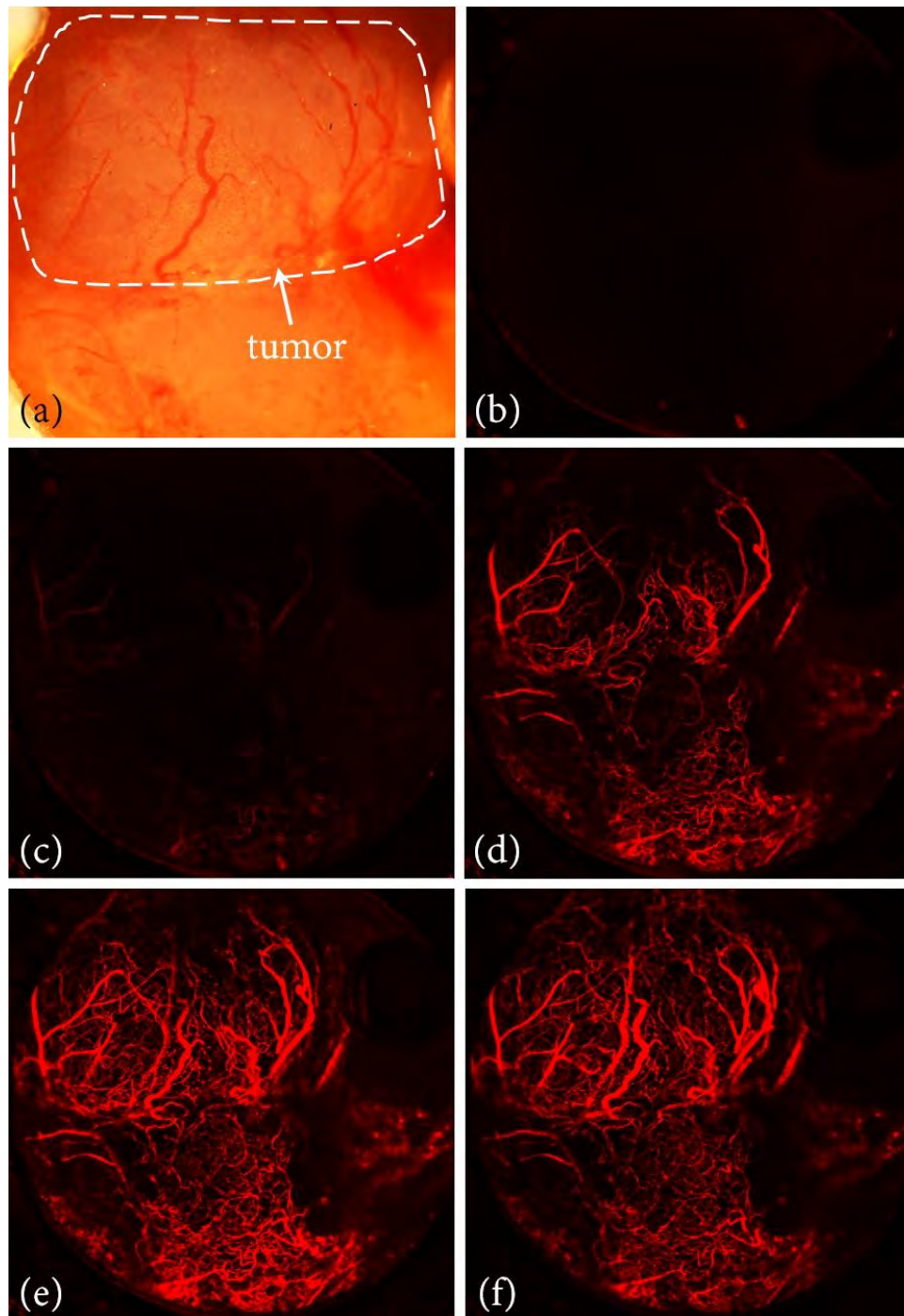
Figure 10.12: White-light and fluorecence images of the MWC taken with a 2X objective. (a) White-light image of the MWC. (b) Fluorescence image of the MWC before injection of the contrast agent. (c)-(f) Representative fluorescence images of the MWC at various time points after injection of the contrast agent.

A higher resolution fluorescence image taken with a 40X objective and a small confocal pinhole (33μm) is shown in Figure 10.13. The use of a small confocal pinhole allows better axial sectioning and individual particles (likely red blood cells) transported within the bloodstream were resolved in the image. In the same tissue region, multiple fluorescence images through a 60μm tissue section were obtained in steps of 0.75μm . A maximum intensity projection of the images was done through software and the result is shown in Figure 10.11.

Subsequently, through use of similar procedures previously described in Section 10.3.2, tissue cells were stained with acridine orange. A 488nm and 633nm laser were simulataneously used to excite the fluorescence from the stained tissue cells and the vascular network. Signals were collected in spectral channels 1 and 2, with gain levels set at 81 and 86, respectively. Images of spectral channels 1 and 2 were pseudo-colored to be green and red, respectively. The combined fluorescence image of the vascular network and tissue cells is shown in Figure 10.15.
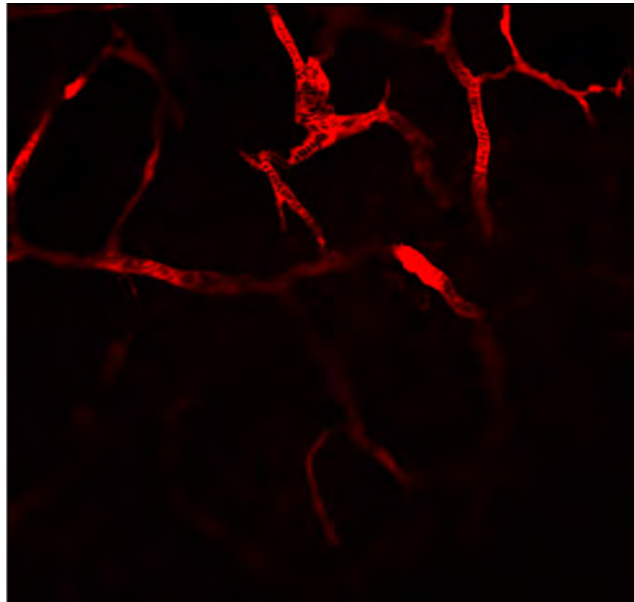
Figure 10.13: A fluorescence image of the vasculature that was taken with the use of a 40X objective and a 33μm confocal pinhole. Individual particles (likely red blood cells) transported within the bloodstream were resolved in the image.
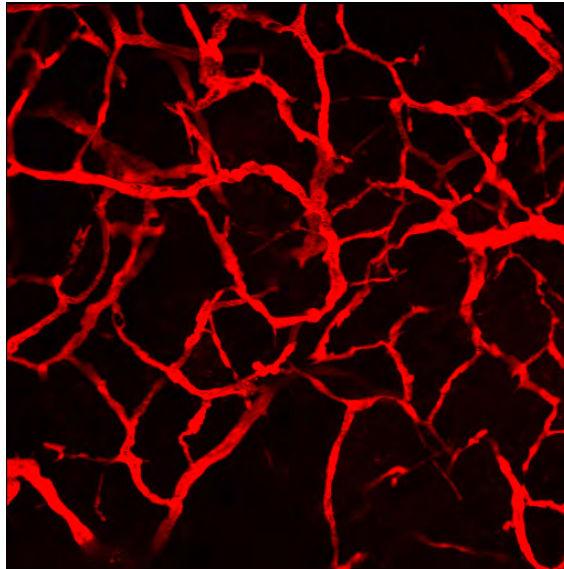
Figure 10.14: A maximum intensity projection of multiple fluorescence images through a 60μm tissue section, which were obtained in steps of 0.75μm. Image taken with a 40X objective and a 33μm confocal pinhole.
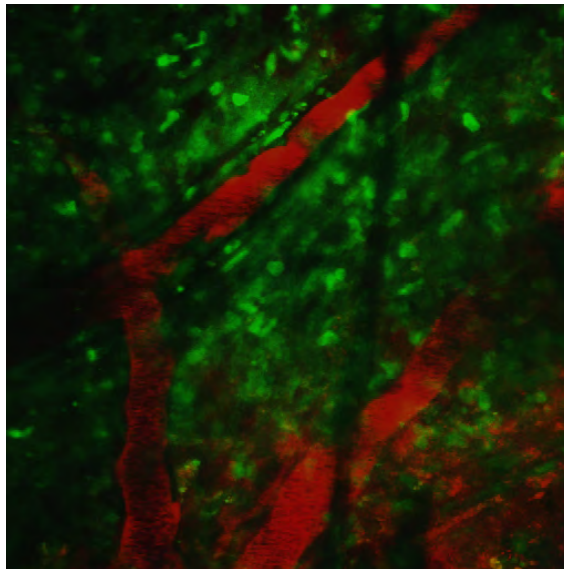
Figure 10.15: A fluorescence image showing the tissue cells around a portion of a vascular network. Image taken with a 40X objective and a 33μm confocal pinhole.

10.3.4 White-light microscopy

In addition to fluorescence confocal microscopy, white-light microscopy is also useful in visualizing the tissue. Figure 10.16 is an example of a white light microscope image of the surface of the PDX tissue, taken with a 4X objective and broadband epi-illumination. In this image, an intricate vascular network and larger vessels can be visualized.
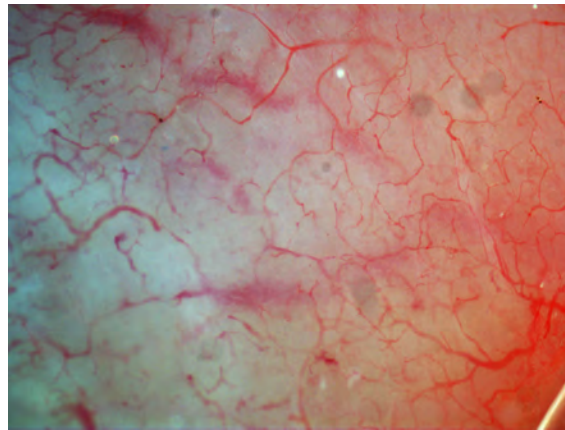
Figure 10.16: White light microscope image of the surface of the PDX tissue, taken with a 4X objective. Intricate vascular network and larger vessels can be visualized.

10.4 Conclusion

This chapter demonstrates the successful engraftment of PDX tumors in NSG mice and subsequent multimodal imaging of the tumor tissue. MRI techniques were performed to visualize anatomy, measure ADC values, and quantify perfusion of the tumor. Optical broadband reflectance spectral imaging was used to measure tissue oxygenation and high resolution microscopy was used to resolve cellular detail of the tumor tissue. On-going work is being carried out to explore the use of other imaging capabilities such as nuclear imaging, ultrasound imaging and computed tomographic imaging of PDX tumors in the MWC model.

CHAPTER 11

Conclusion

11.1 Summary of work

In this dissertation, work was done to develop multimodal imaging approaches to study various aspects of tumor xenografts in the DSFWC and MWC animal models. The main imaging modalities that were developed and utilized include optical fluorescence pH imaging, reflectance spectral imaging, nuclear imaging, and MRI.

For pH imaging, work to improve the accuracy of a ratiometric measurement technique through phantom calibration and accounting for temperature effects was performed. The ratiometric pH imaging technique was used to evaluate whether there was a dose-dependent pH-renormalization effect in DSFWC animals after oral administration of a buffer solution. In addition, the effect of the treatment protocol on tissue with different degrees of acidosis was evaluated.

Work was done to modify an optical setup, which was originally built as an optical scan unit for a confocal microendoscope, to adapt it to be compatible with imaging of the MWC. The resultant fluorescence and reflectance hyperspectral imaging system was used to study tissue oxygenation in the MWC. Experimental work to perform spectral calibration, and to characterize the spectral and spatial resolution of the system was carried out. A model of the optical system was created in a straylight analysis program to understand how straylight in the system can be handled to avoid introducing errors in the spectral measurements. In addition, subroutines written in the Matlab program were written to analyze results of the 3D data cube, to perform spectral decomposition, and to extract physiological information such as SaO_2 .

2D nuclear imaging of 18F-FDG with a β-imager was performed to study glycolytic metabolism in the MWC. In collaboration with Dr Lars Furenlid, 3D pre-

clinical PET imaging was also carried out. The results obtained from the two different methods were compared to evaluate the reliability of using the β-imager as an alternative to study glycolytic metabolism in the MWC model. Depth sensitivity with the β-imager was also studied with a phantom.

MRI was extensively used to study xenografts in the MWC model. Anatomical imaging and functional imaging of the tumors were carried out in this work to provide insights about the status of the tumor. DW imaging was used to study mobility of water in tissue. Qualitative perfusion imaging was achieved with DCE MRI, while quantitative perfusion imaging was achieved with a type of arterial spin labelling technique known as FAIR-RARE.

The advantage of having the ability to combine different imaging techniques to understand complex cancer biology was demonstrated in a study that was carried out to study early response to chemotherapy. Optical reflectance spectral imaging was used to image SaO_2 in the MWC at mutiple time points within the first 70 hours after administration of chemotherapy. Ultimate response was determined by measuring tumor volume from MR anatomical images. Since the demand and supply of oxygen in tissue are largely dependent upon metabolic activity and perfusion, techniques to image these parameters were carried out. Nuclear imaging was use to study glycolytic metabolism while MR techniques were used to study blood perfusion in the tissue.

Finally, the incorporation of PDX tissues in the orthotopic MWC model was successfully carried out. The PDX model presumably recapitulates the characteristics and response patterns of human clinical tumors better than xenografts grown from cultured cells. Therefore, an animal with improved clinical translational power was realized. In vivo imaging of PDX tumors with numerous imaging techniques that were developed earlier was also demonstrated.

11.2 Future directions

The PDX MWC murine model is a new development with numerous areas of research potential that have yet to be fully explored. Currently, the PDX tissue is not modified to express fluorecent proteins. The disadvantage is not being able to use optical means to easily delineate tumor tissue from surrounding tissue. Although modifying the cancer cells to express fluorescent proteins might result in a change in their phenotypical behavior, the convenience of being able to optically delineate cancer cells in the MWC might be a strong motivation for exploring this direction of research. An alternative method of achieving that goal is to inject a fluorescently-conjugated agent that targets cell receptors or DNA components that are unique to human cells. A possible future research opportunity lies in finding those unique molecular targets and the antibodies or peptides that selectively bind to them.

Secondly, it may be useful to use the PDX MWC animal model to test treatment protocols and response patterns associate with different treatment strategies. Since the PDX model presumably recapitulates the characteristics of human clinical disease well, the experimental results should be more reproducible in clinical trials. Currently, a piece of PDX tissue typically takes 4-8 weeks to become successfully engrafted in a NSG mouse. Although the time delay between tissue implantation and successful engraftment might be a barrier to using the animal model to study personalized-treatment protocols, there are other useful applications for the animal model. For instance, information from the genetic profiling of patients' biopsies might give insights to what types of treatment protocols the tumors might respond to and expedite the research needed to answer pertinent questions about cancer biology and/or disease management.

In addition to various research opportunities pertaining to the new PDX model, there are also other imaging techniques that can be developed to further strengthen the versatility of the MWC model. For instance, photoacoustic imaging combines optical excitation and ultrasonic emission to obtain information about the tissue at depths greater than what is possible with traditional optical imaging.

The current rigid 3D printed MWC design provides a stable platform for imaging and fabrication cost is low. Furthermore, the transparent glass coverslip enables high resolution optical imaging to be performed. Implantation of a MWC is fairly simple and takes approximately 15 minutes per animal to complete. However, as expected, the structure does cause a certain level of discomfort to the animal. Due to the animal's chewing of the implanted MWC, the structure often becomes compromised within 2 to 3 weeks and experiments cannot be continued when that occurs. To increase the useful time period of the animal, a different type of WC that is better tolerated by the animals might be necessary. One possible research opportunity could be the use of a transparent, biocompatible, flexible and suturable material in place of the MWC. The use of CLARITY technique [148] has made brain tissue transparent and suitable for optical imaging. It could be possible to use similar techniques to produce transparent, skin-like material that can be used in place of the current MWC design.

In conclusion, the current MWC animal model is a versatile and powerful platform technology that is useful in various types of cancer research studies. A wide range of imaging tools have been successfully developed and demonstrated to be compatible with the animal model. Those imaging tools are capable of extracting anatomical and functional information about the tumor tissue *in vivo* . Nevertheless, there are abundant exciting possibilities ahead that can be explored to further improve its utility for cancer studies.

APPENDIX A

List of Abbreviations

^{18}F-FDG	Fluorodeoxyglucose
2-NDBG	2-[N-(7-nitrobenz-2-oxa-1,3-diazol-4-yl) amino]-2-deoxy-D-glucose
^{64}Cu-ATSM	^{64}Cu-diacetyl-bis(N^4-methylthiosemicarbazone)
ASL	Arterial spin labelling
ATP	Adenosine triphosphate
BCECF	2,7-Bis-(2-carboxyethyl)-5-(and-6-)carboxyfluorescein
BP	Bandpass
BSA	BSA
C-SNARF-1	Carboxy-Seminapthorhodafluor-1
DCE MRI	Dynamic contrast enhanced MRI
DOX	Doxorubicin
DSC MRI	Dynamic susceptibility contrast MRI
DSFWC	Dorsal skinfold window chamber
DW	Diffusion-weighted
DWI	Diffusion-weighted imaging
ER	Oestrogen receptor
FDG	See ^{18}F-FDG
FMISO	^{18}F-fluoromisonidazole
FOV	Field of view
Gd	Gadolinium
GFP	Green fluorescent protein
GLUT	Glucose transporter
Hb	Deoxyhemoglobin
HbO2	Oxyhemoglobin

Hbt	Total hemoglobin
HER2	Human epidermal growth factor receptor
IACUC	Insitutional Animal Care and Use Committee
IP	Intraperitoneal
IV	Intravenous
LP	Longpass
LPF	Longpass filter
LOR	Line-of-repsonse
metHb	methemoglobin
MIBG	Meta-iodobenzylguanidine
MR	Magnetic resonance
MRDF	Mean-detector-response-function
MRI	Magnetic resonance imaging
MRS	Magnetic resonance spectroscopy
MSME	Multi-slice multi-echo
MWC	Mammary window chamber
NA	Numerical aperture
NAC	Neoadjuvant chemotherapy
NMR	Nuclear magnetic resonance
NO	Nitric oxide
NOD/SCID	Non-obese diabetic severe combined immunodeficient
NSG	Non-obese diabetic severe combined immunodeficient gamma
ORCR	Office for the Responsible Conduct of Research
PBS	Phosphate buffered saline
PDX	Patient derived xenografts
PET	Positron emission tomography
PMT	Photomultiplier tubes
PR	Progesterone receptors
PSF	Point spread function
RARE	Rapid Acquisition with Relaxation Enhancement

RF	Radiofrequency
ROI	Region of interest
RBC	Red blood cells
SaO_2	Oxygen saturation
SCID	Severe combined immunodeficient
SNARF	Seminapthorhodafluor
SPECT	Single-photon emission computed tomography
TCA	Tricarboxylic acid
TE	echo time
Ti	Titanium
TR	Repetition time
WC	Window chamber

REFERENCES

[1] C. E. Meacham and S. J. Morrison. Tumour heterogeneity and cancer cell plasticity. *Nature* **501**(7467) 328–37 (2013).

[2] D. Zardavas, A. Irrthum, C. Swanton, *et al.*. Clinical management of breast cancer heterogeneity. *Nature Reviews Clinical Oncology* **12** 381–394 (2015).

[3] D. P. Tabassum and K. Polyak. Tumorigenesis: it takes a village. *Nature Reviews Cancer* **15**(8) 473–483 (2015).

[4] H. DG and R. DA. Translation of research evidence from animals to humans. *JAMA* **296**(14) 1727–1732 (2006).

[5] M. Yang, E. Baranov, J.-W. Wang, *et al.*. Direct external imaging of nascent cancer, tumor progression, angiogenesis, and metastasis on internal organs in the fluorescent orthotopic model. *Proceedings of the National Academy of Sciences* **99**(6) 3824–3829 (2002).

[6] C. Dray, G. Rougon, and F. Debarbieux. Quantitative analysis by in vivo imaging of the dynamics of vascular and axonal networks in injured mouse spinal cord. *Proceedings of the National Academy of Sciences* **106**(23) 9459–9464 (2009).

[7] M. Makale. Intravital imaging and cell invasion. In D. A. Cheresh (editor), *Integrins*, volume 426 of *Methods in Enzymology*, 375 – 401. Academic Press (2007).

[8] J. C. Sandison. A new method for the microscopic study of living growing tissues by the introduction of a transparent chamber in the rabbit's ear. *The Anatomical Record* **28**(4) 281–287 (1924).

[9] N. K. Reitan, M. Thuen, P. E. Goa, *et al.*. Characterization of tumor microvascular structure and permeability: comparison between magnetic resonance imaging and intravital confocal imaging. *Journal of biomedical optics* **15**(3) 036004–036004 (2010).

[10] M. Stroh, J. P. Zimmer, D. G. Duda, *et al.*. Quantum dots spectrally distinguish multiple species within the tumor milieu in vivo. *Nature medicine* **11**(6) 678–682 (2005).

[11] L. S. Sasportas and S. S. Gambhir. Imaging circulating tumor cells in freely moving awake small animals using a miniaturized intravital microscope. *PloS one* **9**(1) (2014).

[12] S. Bertera, X. Geng, Z. Tawadrous, *et al.*. Body window-enabled in vivo multicolor imaging of transplanted mouse islets expressing an insulin-timer fusion protein. *Biotechniques* **35**(4) 718–722 (2003).

[13] J. Lanzen, R. D. Braun, B. Klitzman, *et al.*. Direct demonstration of instabilities in oxygen concentrations within the extravascular compartment of an experimental tumor. *Cancer research* **66**(4) 2219–2223 (2006).

[14] H. Sorg, C. Krueger, and B. Vollmar. Intravital insights in skin wound healing using the mouse dorsal skin fold chamber. *Journal of anatomy* **211**(6) 810–818 (2007).

[15] D. Kedrin, B. Gligorijevic, J. Wyckoff, *et al.*. Intravital imaging of metastatic behavior through a mammary imaging window. *Nature methods* **5**(12) 1019–1021 (2008).

[16] S. Hak, N. K. Reitan, O. Haraldseth, *et al.*. Intravital microscopy in window chambers: a unique tool to study tumor angiogenesis and delivery of nanoparticles. *Angiogenesis* **13**(2) 113–130 (2010).

[17] L. Hallum, S. Chen, S. Cloherty, *et al.*. Functional optical imaging of intrinsic signals in cerebral cortex. *Wiley Encyclopedia of Biomedical Engineering* (2006).

[18] M. J. Farrar, I. M. Bernstein, D. H. Schlafer, *et al.*. Chronic in vivo imaging in the mouse spinal cord using an implanted chamber. *Nature methods* **9**(3) 297–302 (2012).

[19] E. Brown, L. L. Munn, D. Fukumura, *et al.*. In vivo imaging of tumors. *Cold Spring Harbor Protocols* **2010**(7) pdb–prot5452 (2010).

[20] A. Richmond and Y. Su. Mouse xenograft models vs gem models for human cancer therapeutics. *Disease models & mechanisms* **1**(2-3) 78–82 (2008).

[21] G. D. Basu, L. B. Pathangey, T. L. Tinder, *et al.*. Cyclooxygenase-2 inhibitor induces apoptosis in breast cancer cells in an in vivo model of spontaneous metastatic breast cancer. *Molecular Cancer Research* **2**(11) 632–642 (2004).

[22] G. C. Koo, A. Hasan, and R. J. OReilly. Use of humanized severe combined immunodeficient mice for human vaccine development. *Expert review of vaccines* **8**(1) 113–120 (2009).

[23] A. Fantozzi and G. Christofori. Mouse models of breast cancer metastasis. *Breast Cancer Res* **8**(4) 212 (2006).

[24] G. E. Koehl, A. Gaumann, and E. K. Geissler. Intravital microscopy of tumor angiogenesis and regression in the dorsal skin fold chamber: mechanistic insights and preclinical testing of therapeutic strategies. *Clinical & experimental metastasis* **26**(4) 329–344 (2009).

[25] M. F. Shayegan Salek. *Simultaneous Optical and MR Imaging of Tissue Within Implanted Window Chamber: System Development and Application in Measuring Vascular Permeability*. Ph.D. thesis, The University of Arizona. (2013).

[26] R. L. Schafer. *Mammary Window Chamber Model: A Platform For Multi-Modality Cancer Imaging And Dynamic Oxygenation Assessment*. Ph.D. thesis, The University of Arizona. (2015).

[27] R. M. Hoffman. Orthotopic metastatic mouse models for anticancer drug discovery and evaluation: a bridge to the clinic. *Investigational new drugs* **17**(4) 343–360 (1999).

[28] Y. S. DeRose, G. Wang, Y.-C. Lin, *et al.*. Tumor grafts derived from women with breast cancer authentically reflect tumor pathology, growth, metastasis and disease outcomes. *Nature medicine* **17**(11) 1514–1520 (2011).

[29] M. C. Brahimi-Horn, J. Chiche, and J. Pouyssegur. Hypoxia signalling controls metabolic demand. *Current opinion in cell biology* **19**(2) 223–229 (2007).

[30] P. Rich. The molecular machinery of keilin's respiratory chain. *Biochemical Society Transactions* **31**(6) 1095–1106 (2003).

[31] M. G. Vander Heiden, L. C. Cantley, and C. B. Thompson. Understanding the warburg effect: the metabolic requirements of cell proliferation. *science* **324**(5930) 1029–1033 (2009).

[32] J. R. Cantor and D. M. Sabatini. Cancer cell metabolism: one hallmark, many faces. *Cancer discovery* **2**(10) 881–898 (2012).

[33] N. C. Denko. Hypoxia, hif1 and glucose metabolism in the solid tumour. *Nature Reviews Cancer* **8**(9) 705–713 (2008).

[34] O. Warburg, F. Wind, and E. Negelein. The metabolism of tumors in the body. *Science* **123**(3191) 309–314 (1956).

[35] A. Carracedo, L. C. Cantley, and P. P. Pandolfi. Cancer metabolism: fatty acid oxidation in the limelight. *Nature reviews Cancer* **13**(4) 227–232 (2013).

[36] K. C. Patra and N. Hay. The pentose phosphate pathway and cancer. *Trends in biochemical sciences* **39**(8) 347–354 (2014).

[37] B. A. Webb, M. Chimenti, M. P. Jacobson, *et al.*. Dysregulated ph: a perfect storm for cancer progression. *Nature Reviews Cancer* **11**(9) 671–677 (2011).

[38] R. J. Gillies, N. Raghunand, G. S. Karczmar, *et al.*. Mri of the tumor microenvironment. *Journal of Magnetic Resonance Imaging* **16**(4) 430–450 (2002).

[39] F. A. Gallagher, M. I. Kettunen, S. E. Day, *et al.*. Magnetic resonance imaging of ph in vivo using hyperpolarized 13c-labelled bicarbonate. *Nature* **453**(7197) 940–943 (2008).

[40] V. Estrella, T. Chen, M. Lloyd, *et al.*. Acidity generated by the tumor microenvironment drives local invasion. *Cancer research* **73**(5) 1524–1535 (2013).

[41] D. Lagadic-Gossmann, L. Huc, and V. Lecureur. Alterations of intracellular ph homeostasis in apoptosis: origins and roles. *Cell Death & Differentiation* **11**(9) 953–961 (2004).

[42] S. Matsuyama, J. Llopis, Q. L. Deveraux, *et al.*. Changes in intramitochondrial and cytosolic ph: early events that modulate caspase activation during apoptosis. *Nature cell biology* **2**(6) 318–325 (2000).

[43] F. Hirschhaeuser, U. G. Sattler, and W. Mueller-Klieser. Lactate: a metabolic key player in cancer. *Cancer research* **71**(22) 6921–6925 (2011).

[44] E. K. Rofstad, B. Mathiesen, K. Kindem, *et al.*. Acidic extracellular ph promotes experimental metastasis of human melanoma cells in athymic nude mice. *Cancer research* **66**(13) 6699–6707 (2006).

[45] R. J. Gillies and R. A. Gatenby. Hypoxia and adaptive landscapes in the evolution of carcinogenesis. *Cancer and Metastasis Reviews* **26**(2) 311–317 (2007).

[46] M. F. McCarty and J. Whitaker. Manipulating tumor acidification as a cancer treatment strategy. *Altern Med Rev* **15**(3) 264–72 (2010).

[47] G. Helmlinger, A. Sckell, M. Dellian, *et al.*. Acid production in glycolysis-impaired tumors provides new insights into tumor metabolism. *Clinical Cancer Research* **8**(4) 1284–1291 (2002).

[48] A. S. Silva, J. A. Yunes, R. J. Gillies, *et al.*. The potential role of systemic buffers in reducing intratumoral extracellular ph and acid-mediated invasion. *Cancer research* **69**(6) 2677–2684 (2009).

[49] I. F. Robey, B. K. Baggett, N. D. Kirkpatrick, *et al.*. Bicarbonate increases tumor ph and inhibits spontaneous metastases. *Cancer research* **69**(6) 2260–2268 (2009).

[50] I. F. Robey and N. K. Martin. Bicarbonate and dichloroacetate: evaluating ph altering therapies in a mouse model for metastatic breast cancer. *BMC cancer* **11**(1) 235 (2011).

[51] Buffer therapy. http://imaging.moffitt.org/research-4.aspx.

[52] L. Q. Chen, C. M. Howison, J. J. Jeffery, *et al.*. Evaluations of extracellular ph within in vivo tumors using acidocest mri. *Magnetic Resonance in Medicine* **72**(5) 1408–1417 (2014).

[53] T. Rink, R. Tsien, and T. Pozzan. Cytoplasmic ph and free mg2+ in lympho-cytes. *The Journal of Cell Biology* **95**(1) 189–196 (1982).

[54] Y. Shen, M. Rosendale, R. E. Campbell, *et al.*. phuji, a ph-sensitive red fluorescent protein for imaging of exo-and endocytosis. *The Journal of cell biology* **207**(3) 419–432 (2014).

[55] J. Han and K. Burgess. Fluorescent indicators for intracellular ph. *Chemical reviews* **110**(5) 2709–2728 (2009).

[56] I. Johnson and M. Spence. The molecular probes handbook - a guide to fluorescent probes and labeling technologies (2010).

[57] Y. Lin. *Development and analysis of optical pH imaging techniques*. Ph.D. thesis, The University of Arizona. (2010).

[58] Y. Lin, T.-Y. Wu, and A. F. Gmitro. Error analysis of ratiometric imaging of extracellular ph in a window chamber model. *Journal of biomedical optics* **17**(4) 0460041–0460046 (2012).

[59] S. Srinivasan, B. W. Pogue, S. Jiang, *et al.*. Interpreting hemoglobin and water concentration, oxygen saturation, and scattering measured in vivo by near-infrared breast tomography. *Proceedings of the National Academy of Sciences* **100**(21) 12349–12354 (2003).

[60] Y. Lin and A. F. Gmitro. Errors in confocal fluorescence ratiometric imaging microscopy due to chromatic aberration. *Applied optics* **50**(1) 95–102 (2011).

[61] G. Grynkiewicz, M. Poenie, and R. Y. Tsien. A new generation of ca2+ indicators with greatly improved fluorescence properties. *Journal of Biological Chemistry* **260**(6) 3440–3450 (1985).

[62] K. Buckler and R. Vaughan-Jones. Application of a new ph-sensitive fluoroprobe (carboxy-snarf-1) for intracellular ph measurement in small, isolated cells. *Pflügers Archiv* **417**(2) 234–239 (1990).

[63] S. Bassnett, L. Reinisch, and D. C. Beebe. Intracellular ph measurement using single excitation-dual emission fluorescence ratios. *American Journal of Physiology-Cell Physiology* **258**(1) C171–C178 (1990).

[64] N. Raghunand and R. J. Gillies. ph and drug resistance in tumors. *Drug Resistance Updates* **3**(1) 39–47 (2000).

[65] R. M. Hoffman. The multiple uses of fluorescent proteins to visualize cancer in vivo. *Nature Reviews Cancer* **5**(10) 796–806 (2005).

[66] M. Yang, J. Reynoso, M. Bouvet, *et al.*. A transgenic red fluorescent protein-expressing nude mouse for color-coded imaging of the tumor microenvironment. *Journal of cellular biochemistry* **106**(2) 279–284 (2009).

[67] M. Yang, L. Li, P. Jiang, *et al.*. Dual-color fluorescence imaging distinguishes tumor cells from induced host angiogenic vessels and stromal cells. *Proceedings of the National Academy of Sciences* **100**(24) 14259–14262 (2003).

[68] P. Jiang, K. Yamauchi, M. Yang, *et al.*. Tumor cells genetically labeled with gfp in the nucleus and rfp in the cytoplasm for imaging cellular dynamics. *Cell Cycle* **5**(11) 1198–1201 (2006).

[69] R. M. Hoffman. Transgenic nude mice ubiquitously expressing fluorescent proteins for color-coded imaging of the tumor microenvironment. In S. R. Singh and V. Coppola (editors), *Mouse Genetics*, volume 1194 of *Methods in Molecular Biology*, 353–365. Springer New York (2014). ISBN 978-1-4939-1214-8.

[70] T.-Y. Wu, A. R. Rouse, S. K. Chambers, *et al.*. Confocal microlaparoscope for imaging the fallopian tube. *Journal of biomedical optics* **19**(11) 116010–116010 (2014).

[71] R. Schafer, H. M. Leung, and A. F. Gmitro. Multi-modality imaging of a murine mammary window chamber for breast cancer research. *BioTechniques* **57**(1) 45 (2014).

[72] C. Zou, Y. Wang, and Z. Shen. 2-nbdg as a fluorescent indicator for direct glucose uptake measurement. *Journal of biochemical and biophysical methods* **64**(3) 207–215 (2005).

[73] S. R. Millon, J. H. Ostrander, J. Q. Brown, *et al.*. Uptake of 2-nbdg as a method to monitor therapy response in breast cancer cell lines. *Breast cancer research and treatment* **126**(1) 55–62 (2011).

[74] R. A. Gatenby, E. T. Gawlinski, A. F. Gmitro, *et al.*. Acid-mediated tumor invasion: a multidisciplinary study. *Cancer research* **66**(10) 5216–5223 (2006).

[75] J. E. Bugaj, S. Achilefu, R. B. Dorshow, *et al.*. Novel fluorescent contrast agents for optical imaging of in vivo tumors based on a receptor-targeted dye-peptide conjugate platform. *Journal of biomedical optics* **6**(2) 122–133 (2001).

[76] X. Wu, H. Liu, J. Liu, *et al.*. Immunofluorescent labeling of cancer marker her2 and other cellular targets with semiconductor quantum dots. *Nature biotechnology* **21**(1) 41–46 (2003).

[77] X. Gao, Y. Cui, R. M. Levenson, *et al.*. In vivo cancer targeting and imaging with semiconductor quantum dots. *Nature biotechnology* **22**(8) 969–976 (2004).

[78] J. Chen, S. Zhuo, R. Chen, *et al.*. Depth-resolved spectral imaging of rabbit oesophageal tissue based on two-photon excited fluorescence and second-harmonic generation. *New Journal of Physics* **9**(7) 212 (2007).

[79] H. Choi, D. Wadduwage, P. T. Matsudaira, *et al.*. Depth resolved hyperspectral imaging spectrometer based on structured light illumination and fourier transform interferometry. *Biomed. Opt. Express* **5**(10) 3494–3507 (2014).

[80] N. Hagen and M. W. Kudenov. Review of snapshot spectral imaging technologies. *Optical Engineering* **52**(9) 090901–090901 (2013).

[81] A. Harvey and D. Fletcher-Holmes. Birefringent fourier-transform imaging spectrometer. *Opt. Express* **12**(22) 5368–5374 (2004).

[82] M. W. Kudenov and E. L. Dereniak. Compact real-time birefringent imaging spectrometer. *Opt. Express* **20**(16) 17973–17986 (2012).

[83] H. M. Leung and A. F. Gmitro. Fluorescence and reflectance spectral imaging system for a murine mammary window chamber model. *Biomedical optics express* **6**(8) 2887–2894 (2015).

[84] H. Makhlouf, A. F. Gmitro, A. A. Tanbakuchi, *et al.*. Multispectral confocal microendoscope for in vivo and in situ imaging. *Journal of biomedical optics* **13**(4) 044016–044016 (2008).

[85] N. Keshava and J. F. Mustard. Spectral unmixing. *Signal Processing Magazine, IEEE* **19**(1) 44–57 (2002).

[86] M. J. Doughty. pH dependent spectral properties of sodium fluorescein ophthalmic solutions revisited. *Ophthalmic and Physiological Optics* **30**(2) 167–174 (2010).

[87] W. G. Zijlstra, A. Buursma, and O. W. van Assendelft. *Visible and near infrared absorption spectra of human and animal haemoglobin: determination and application*. VSP (2000).

[88] R. L. van Veen, H. Sterenborg, A. Pifferi, *et al.*. Determination of vis-nir absorption coefficients of mammalian fat, with time-and spatially resolved diffuse reflectance and transmission spectroscopy. In *Biomedical Topical Meeting*, SF4. Optical Society of America (2004).

[89] S. Stolik, J. Delgado, A. Perez, *et al.*. Measurement of the penetration depths of red and near infrared light in human ex vivo tissues. *Journal of Photochemistry and Photobiology B: Biology* **57**(2) 90–93 (2000).

[90] C. Abrial, X. Durando, M.-A. Mouret-Reynier, *et al.*. Role of neo-adjuvant hormonal therapy in the treatment of breast cancer: a review of clinical trials. *International journal of general medicine* **2** 129–40 (2009).

[91] J. A. van der Hage, C. J. van de Velde, J.-P. Julien, *et al.*. Preoperative chemotherapy in primary operable breast cancer: results from the european organization for research and treatment of cancer trial 10902. *Journal of Clinical Oncology* **19**(22) 4224–4237 (2001).

[92] V. Marchand, A. Angelergues, V. Gobaux, *et al.*. Prospective and comparative evaluation of the toxicity of adjuvant concurrent chemoradiotherapy after neoadjuvant chemotherapy for breast cancer. *American journal of clinical oncology* **36**(5) 425–429 (2013).

[93] H. A. Wieder, A. J. Beer, F. Lordick, *et al.*. Comparison of changes in tumor metabolic activity and tumor size during chemotherapy of adenocarcinomas of the esophagogastric junction. *Journal of Nuclear Medicine* **46**(12) 2029–2034 (2005).

[94] J.-W. Wang, W. Zheng, J.-B. Liu, *et al.*. Assessment of early tumor response to cytotoxic chemotherapy with dynamic contrast-enhanced ultrasound in human breast cancer xenografts (2013).

[95] D. Roblyer, S. Ueda, A. Cerussi, *et al.*. Optical imaging of breast cancer oxyhemoglobin flare correlates with neoadjuvant chemotherapy response one day after starting treatment. *Proceedings of the National Academy of Sciences* **108**(35) 14626–14631 (2011).

[96] L. Martin. *All you really need to know to interpret arterial blood gases*. Lippincott Williams & Wilkins (1999).

[97] S. De Boo, J. Kopecka, D. Brusa, *et al.*. inos activity is necessary for the cytotoxic and immunogenic effects of doxorubicin in human colon cancer cells. *Mol Cancer* **8**(19) 108–111 (2009).

[98] M. B. Taylor, K. G. Christian, N. Patel, *et al.*. Methemoglobinemia: Toxicity of inhaled nitric oxide therapy. *Pediatric Critical Care Medicine* **2**(1) 99–101 (2001).

[99] D. L. Holliday and V. Speirs. Choosing the right cell line for breast cancer research. *Breast Cancer Res* **13**(4) 215 (2011).

[100] B. M. Burt, J. L. Humm, D. A. Kooby, *et al.*. Using positron emission tomography with [18 f] fdg to predict tumor behavior in experimental colorectal cancer. *Neoplasia* **3**(3) 189–195 (2001).

[101] D. W. Rickey, R. Gordon, and W. Huda. On lifting the inherent limitations of positron emission tomography by using magnetic fields (magpet). *Automedica* **14**(904) 355–369 (1992).

[102] Z. Cho, J. Chan, L. Ericksson, *et al.*. Positron ranges obtained from biomedically important positron-emitting radionuclides. *Journal of nuclear medicine: official publication, Society of Nuclear Medicine* **16**(12) 1174–1176 (1975).

[103] C. Champion and C. Le Loirec. Positron follow-up in liquid water: I. a new monte carlo track-structure code. *Physics in medicine and biology* **51**(7) 1707 (2006).

[104] P. E. V. Dale L Bailey, David W Townsend and M. N. Maisey. *Positron Emission Tomography: Basic Sciences*. Springer (2004).

[105] S. K. Moore. *ModPET: Novel Applications of Scintillation Cameras to Preclinical PET*. Ph.D. thesis, The University of Arizona. (2011).

[106] L. Chen, L. S. Gobar, N. G. Knowles, *et al.*. Direct imaging of radionuclide-produced electrons and positrons with an ultrathin phosphor. *Journal of Nuclear Medicine* **49**(7) 1141–1145 (2008).

[107] E. Coetsee, J. Terblans, and H. Swart. Degradation of Y_2SiO_5:Ce phosphor powders. *Journal of luminescence* **126**(1) 37–42 (2007).

[108] Q. Zhang, K. Pita, S. Buddhudu, *et al.*. Luminescent properties of rare-earth ion doped yttrium silicate thin film phosphors for a full-colour display. *Journal of Physics D: Applied Physics* **35**(23) 3085 (2002).

[109] Introduction to image intensifiers for scientific imaging, URL = www.princetoninstruments.com.

[110] C. S. Levin and E. J. Hoffman. Calculation of positron range and its effect on the fundamental limit of positron emission tomography system spatial resolution. *Physics in medicine and biology* **44**(3) 781 (1999).

[111] S. E. Derenzo. Precision measurement of annihilation point spread distributions for medically important positron emitters. *Lawrence Berkeley National Laboratory* (2010).

[112] J. D. Power, K. A. Barnes, A. Z. Snyder, *et al.*. Spurious but systematic correlations in functional connectivity mri networks arise from subject motion. *Neuroimage* **59**(3) 2142–2154 (2012).

[113] I. J. Zamora, O. O. Olutoye, D. L. Cass, *et al.*. Prenatal mri fetal lung volumes and percent liver herniation predict pulmonary morbidity in congenital diaphragmatic hernia (cdh). *Journal of pediatric surgery* **49**(5) 688–693 (2014).

[114] Magnetic resonance imaging (mri) exams (indicator). *OECD* (2015).

[115] A. R. Padhani, G. Liu, D. Mu-Koh, *et al.*. Diffusion-weighted magnetic resonance imaging as a cancer biomarker: consensus and recommendations. *Neoplasia* **11**(2) 102–125 (2009).

[116] S. Buchbender, S. Obenauer, S. Mohrmann, *et al.*. Arterial spin labelling perfusion mri of breast cancer using fair truefisp: initial results. *Clinical radiology* **68**(3) e123–e127 (2013).

[117] K. W. Chan, G. Liu, X. Song, *et al.*. Mri-detectable ph nanosensors incorporated into hydrogels for in vivo sensing of transplanted-cell viability. *Nature materials* **12**(3) 268–275 (2013).

[118] S. D. Rane and J. C. Gore. Measurement of t1 of human arterial and venous blood at 7t. *Magnetic resonance imaging* **31**(3) 477–479 (2013).

[119] P. A. Bottomley, T. H. Foster, R. E. Argersinger, *et al.*. A review of normal tissue hydrogen nmr relaxation times and relaxation mechanisms from 1–100 mhz: dependence on tissue type, nmr frequency, temperature, species, excision, and age. *Medical physics* **11**(4) 425–448 (1984).

[120] A.-L. Lin, Q. Qin, X. Zhao, *et al.*. Blood longitudinal (t 1) and transverse (t 2) relaxation time constants at 11.7 tesla. *Magnetic Resonance Materials in Physics, Biology and Medicine* **25**(3) 245–249 (2012).

[121] M. C. Dobre, K. Uğurbil, and M. Marjanska. Determination of blood longitudinal relaxation time (t 1) at high magnetic field strengths. *Magnetic resonance imaging* **25**(5) 733–735 (2007).

[122] J. Hennig, A. Nauerth, and H. Friedburg. Rare imaging: a fast imaging method for clinical mr. *Magnetic Resonance in Medicine* **3**(6) 823–833 (1986).

[123] R. Woodhams, K. Matsunaga, K. Iwabuchi, *et al.*. Diffusion-weighted imaging of malignant breast tumors: the usefulness of apparent diffusion coefficient (adc) value and adc map for the detection of malignant breast tumors and evaluation of cancer extension. *Journal of computer assisted tomography* **29**(5) 644–649 (2005).

[124] D.-M. Koh and D. J. Collins. Diffusion-weighted mri in the body: applications and challenges in oncology. *American Journal of Roentgenology* **188**(6) 1622–1635 (2007).

[125] D. M. Patterson, A. R. Padhani, and D. J. Collins. Technology insight: water diffusion mria potential new biomarker of response to cancer therapy. *Nature Clinical Practice Oncology* **5**(4) 220–233 (2008).

[126] Y. Hayashida, T. Yakushiji, K. Awai, *et al.*. Monitoring therapeutic responses of primary bone tumors by diffusion-weighted image: initial results. *European radiology* **16**(12) 2637–2643 (2006).

[127] E. Stejskal and J. Tanner. Spin diffusion measurements: Spin echoes in the presence of a time dependent field gradient. *Journal of Chemical Physics* **42**(1) 288–292 (1965).

[128] D. Le Bihan (editor). *Diffusion and Perfusion Magnetic Resonance Imaging: Applications to Functional MRI.*. Raven Press, New York (1995).

[129] D. Le Bihan, E. Breton, D. Lallemand, *et al.*. Mr imaging of intravoxel incoherent motions: application to diffusion and perfusion in neurologic disorders. *Radiology* **161**(2) 401–407 (1986).

[130] B. University of Colorado. Mcdb 1150-003: Biofundamentals. topic 6. 497–505 (2007-2015).

[131] M. Essig, M. S. Shiroishi, T. B. Nguyen, *et al.*. Perfusion mri: the five most frequently asked technical questions. *American journal of roentgenology* **200**(1) 24–34 (2013).

[132] D. Le Bihan, E. Breton, D. Lallemand, *et al.*. Separation of diffusion and perfusion in intravoxel incoherent motion mr imaging. *Radiology* **168**(2) 497–505 (1988).

[133] J.-H. Zhou, L.-H. Cao, W. Zheng, *et al.*. Contrast-enhanced gray-scale ultrasound for quantitative evaluation of tumor response to chemotherapy: preliminary results with a mouse hepatoma model. *American Journal of Roentgenology* **196**(1) W13–W17 (2011).

[134] R. García-Figueiras, V. J. Goh, A. R. Padhani, *et al.*. Ct perfusion in oncologic imaging: a useful tool? *American Journal of Roentgenology* **200**(1) 8–19 (2013).

[135] S. Warach, J. F. Dashe, and R. R. Edelman. Clinical outcome in ischemic stroke predicted by early diffusion-weighted and perfusion magnetic resonance imaging: a preliminary analysis. *Journal of Cerebral Blood Flow & Metabolism* **16**(1) 53–59 (1996).

[136] Y. Ohno, H. Hatabu, K. Murase, *et al.*. Primary pulmonary hypertension: 3d dynamic perfusion mri for quantitative analysis of regional pulmonary perfusion. *American Journal of Roentgenology* **188**(1) 48–56 (2007).

[137] K. D. Song, D. Choi, J. H. Lee, *et al.*. Evaluation of tumor microvascular response to brivanib by dynamic contrast-enhanced 7-t mri in an orthotopic xenograft model of hepatocellular carcinoma. *American Journal of Roentgenology* **202**(6) W559–W566 (2014).

[138] F. Calamante. Arterial input function in perfusion mri: a comprehensive review. *Progress in nuclear magnetic resonance spectroscopy* **74** 1–32 (2013).

[139] S. Verma, B. Turkbey, N. Muradyan, *et al.*. Overview of dynamic contrast-enhanced mri in prostate cancer diagnosis and management. *American Journal of Roentgenology* **198**(6) 1277–1288 (2012).

[140] S. L. Barnes, J. G. Whisenant, M. E. Loveless, *et al.*. Practical dynamic contrast enhanced mri in small animal models of cancer: data acquisition, data analysis, and interpretation. *Pharmaceutics* **4**(3) 442–478 (2012).

[141] C. Leithner, K. Gertz, H. Schröck, *et al.*. A flow sensitive alternating inversion recovery (fair)-mri protocol to measure hemispheric cerebral blood flow in a mouse stroke model. *Experimental neurology* **210**(1) 118–127 (2008).

[142] C. De Bazelaire, N. M. Rofsky, G. Duhamel, *et al.*. Arterial spin labeling blood flow magnetic resonance imaging for the characterization of metastatic renal cell carcinoma. *Academic radiology* **12**(3) 347–357 (2005).

[143] J. A. Detre, W. Zhang, D. A. Roberts, *et al.*. Tissue specific perfusion imaging using arterial spin labeling. *NMR in Biomedicine* **7**(1-2) 75–82 (1994).

[144] T. E. Yankeelov, D. R. Pickens, and R. R. Price. *Quantitative MRI in Cancer*. Taylor & Francis (2011).

[145] S.-G. Kim. Quantification of relative cerebral blood flow change by flow-sensitive alternating inversion recovery (fair) technique: Application to functional mapping. *Magnetic Resonance in Medicine* **34**(3) 293–301 (1995).

[146] S.-G. Kim and N. V. Tsekos. Perfusion imaging by a flow-sensitive alternating inversion recovery (fair) technique: application to functional brain imaging. *Magnetic Resonance in Medicine* **37**(3) 425–435 (1997).

[147] H. M. Leung, R. Schafer, and A. F. Gmitro. Imaging patient derived breast cancer xenografts in an orthotopic mammary window chamber model. In *CLEO: Applications and Technology*, ATh3J–5. Optical Society of America (2015).

[148] K. Chung, J. Wallace, S.-Y. Kim, *et al.*. Structural and molecular interrogation of intact biological systems. *Nature* **497**(7449) 332–337 (2013).